Mathematical Modelling of Calcium Ions during Ischaemic Stroke

George Qian

Brasenose College

University of Oxford

A thesis submitted for the degree of

Doctor of Philosophy

Michaelmas 2017

Abstract

Stroke is a condition affecting over 100,000 people every year in the UK alone. There are two types of stroke: ischaemic, which is the more common and occurs when blood supply to the brain is blocked and haemorrhagic, where blood vessels in the brain burst, causing bleeding. After the occurrence of an ischaemic stroke, one typically observes three regions being formed, namely the ischaemic core, penumbra and the unaffected region. While cells in the ischaemic core die immediately due to lack of blood supply, there remains a chance to salvage those in the penumbra, as these cells are still supplied temporarily by peripheral vessels. Clinicians, however, still have difficulty identifying the penumbra, despite advances in medical technology.

To this end, our goal is to create a mathematical model that uses cell calcium ion concentration as a biomarker to predict in these three regions of the brain, given some decrease in blood flow, which is a clinically measureable input. This would allow our model to be used as a diagnostic tool for clinicians to determine which areas to apply reperfusion.

We find that our model is able to portray certain spatial inhomogeneities known as Turing patterns, which arise from one set of equations, with calcium concentration as its sole biomarker. This is a feature that, to our knowledge, has not been investigated in other models. The presence of Turing patterns allows us potentially to model the ischaemic core, penumbra and unaffected regions; however, the spatial inhomogeneities observed in our model simulations do not yet correspond to these regions due to the presence of higher-order modes. We, therefore, suggest ways to improve the model to make it a viable clinical tool.

Acknowledgements

I have been very privileged to have met and known some truly wonderful people while studying here; people who have helped me in so many ways. All I will do here is to leave a note here thanking you for making me feel that much better.

First, thank you to my supervisor, Stephen. No other supervisor can be as patient, calm and understanding as you have been. Your door is always open and you're always available for any advice. I've truly enjoyed being your student, learning so much just from how you think and act. I will remember your advice and philosophy. In fact, I notice that my desk is a little tidier nowadays.

Thank you also to Elspeth. You've been such a great Tutor for Graduate Studies, always checking to make sure that I'm on track and spending time to talk, with a warm smile, if required. To think that you do this for each Brasenose graduate student is astonishingly sweet.

I'd like to thank Philip Maini, as well, for always taking the time to answer all my questions on Turing instabilities and being so warm and friendly whenever I would visit.

To the PUMMA group, especially Wahbi (a charismatic, confident and loyal ENFP), Jamil (the crazy cat with whom I've shared great times), Flora (always the voice of reason and a real inspiration) and Simao (our personal movie database who has an extremely caring personality): thanks for being great labmates and putting up with my snoring. I've learnt so much about movies, politics, food and board games after spending so much time together.

Also, thank you to Adam Mahdi, for all the great discussions we've had on both dynamical systems and life in general. I'm sure you know that I value your knowledge and advice greatly. You've always made time for me, despite your hectic schedule and for that I'll always be grateful.

To my CDT group: it was a pleasure being in the same class for almost a year. I must thank, in particular: Thomas (you are the older brother I always wished I could have), Steve (conversation with you is always so engaging) and Andre, for taking care of me and always offering an ear.

To Adam Szmul, thank you for being such a great friend and fantastic person. I have learnt so much from you about things ranging from Polish culture to being a little more practical. Even more importantly, I always feel better after talking to you and that, to me, is priceless.

To Tasos, thank you, my fellow INFP and *caniformia*, for everything. Knowing I can share anything with you and be met without judgement is extremely comforting and yet we still have the greatest laughs ever.

Thanks also to the Cosin Close Club (Steve, Emily, Dongli, Julian, Lili and Joha) for all the great times, Paka, Mengyuan, James and Wilfride for our amazing adventures together, Jo, for being so kind and still keeping the CDT running. Karen, Faye and Steven: you have such big hearts and spirits that I'm astounded you could fit into my messy room every week. Tingting and Arvind: thank you – even though, as labmates, I never gave you enough room to manoeuvre, we're still great friends now!

I must also mention some special people from Imperial College. Dominik, my warden, mentor and friend: thank you for helping me see the big picture. Where would I be without you? Aisha: my big sister, to whom I go to vent or just have some fun and laughter. Alex: you taught me leadership... one day I may even put that into practice. Laurie: I learnt how to be friendly and caring, yet firm if needed. Valerio: you display the very best qualities of an INFP. It fills me with joy seeing how far you've come. Tessa: thanks for being so sweet and caring. Kamara: seeing you always brightens my day! Frances: you're the best hall manager ever. Elena and Nic: thank you for all you've done through all these years.

To my friends from NZ: David, Jonathan and Nick. Thank you for being there from the very beginning. Knowing I have friendships as solid as ours makes me stronger whenever the chips are down and I always miss you when I'm here.

Finally, thank you to my dear family. Sarah, even if you weren't the best sister (which you are!), you'd be my close INFJ friend and the only squirrel I could ever laugh and cry with. Dearest Baba, you are and always have been my hero. Thank you for devoting all your time, energy and life to looking after us. I love you heaps and always will. And Mama, though you may be worlds apart, I know you're still here, always watching and forever smiling. May the Force be with you, always. *Dum habito, semper te amo.*

Nomenclature

A — Proportion of cells that are Alive

ADP – Adenosine Diphosphate

ATP – Adenosine Triphosphate

Ca^{2+} - Calcium Ions

CBF – Cerebral Blood Flow

CICR – Calcium-Induced Calcium Release

D – Damage Magnitude

ER- Endoplasmic Reticulum

I – Injury Magnitude

IP_3 – Inositol Triphosphate

K^+ — Potassium Ions

N — Proportion of cells that are Necrotised

Na^+ - Sodium Ions

ODE – Ordinary Differential Equation

PDE – Partial Differential Equation

S – Stress Magnitude

SERCA - Sarco/Endoplasmic Reticulum Ca^{2+}-ATPase

SR – Sarcoplasmic Reticulum

V — Proportion of cells that are Vulnernable

1. Introduction

"Heard melodies are sweet, but those unheard

Are sweeter; therefore, ye soft pipes, play on;

'Ode on a Grecian Urn', John Keats.

In a world where we, as human beings, have made such great technological advances that we can travel to the poles, construct buildings so tall that they peak through the clouds and harness energy from the elements, it is ironic that we cannot always safeguard the very bodies that enable us to achieve such feats. We are constantly fighting off illnesses and often eventually succumb to one. There are many diseases and conditions which are familiar to most people: for instance, heart disease and cancer. This thesis investigates the condition that is stroke and, in particular, ischaemic stroke, which occurs when the blood flowing to the brain is blocked. In the UK alone, there are around 100,000 occurrences of stroke every year [1]. In 2015, around 40,000 UK individuals died of stroke [2], while it is estimated that around two-thirds of stroke survivors suffer a subsequent disability [3]. The NHS spends almost £2 billion per year to treat individuals both during and after stroke and yet it is well known that 'prevention is the best cure'. The biggest risk factor for stroke is high blood pressure (hypertension); a 10mmHg reduction in systolic blood pressure reduces the chances of a stroke by 40% and heart attack by 20% [4]. Living a healthier lifestyle and, especially, limiting salt intake does help to avoid strokes. If an individual does suffer a stroke, however, it is important to understand the physiology behind the condition to allow clinicians to administer appropriate treatment.

There are two types of strokes: ischaemic (caused by blockage of blood flow) and haemorrhagic (caused by bleeding). Ischaemic strokes are by far the more common, making up around 85% of all incidences [5] and we will focus on these throughout the thesis.

In order to understand why ischaemic strokes cause cell death, we must first realise that the

healthy human body is like a well-engineered machine that monitors the processes which occur within itself, preventing any variable straying too far from the norm. This process is known as *homeostasis*, a series of negative feedback mechanisms that stabilise internal conditions, such as body temperature, blood pH and ionic concentrations. The breakdown of biological controls that form a key part of the homeostatic mechanism, however, often has severe consequences. The example of particular interest during stroke is the body's failure to regulate intracellular calcium concentrations. Typically, the calcium concentration inside our cells (~100nM) is several orders of magnitude lower than the extracellular (~1mM) [6]. Such large differences in concentration can only be preserved by the action of ion pumps, which use the cell's energy to push calcium ions against the concentration gradient into the extracellular space. Such is the case for a healthy individual: if, however, oxygen is unable to reach parts of the brain, as happens during an ischaemic event, then the energy reserves become depleted. This causes failure of typical homeostatic measures designed to regulate intracellular calcium concentration which, in turn, triggers a series of chemical reactions that cause the cell to die.

In this thesis, we present a mathematical model that captures the role of calcium ions during an ischaemic event. In the model, the calcium concentration both inside the cells as well as in the surrounding extracellular fluid serve as a gauge of the damage inflicted upon the cells. The prediction of the damage that a stroke inflicts upon the cell leads to a further model prediction of cell fate: whether it survives, dies or becomes, in our words, vulnerable. The last case is the most interesting: vulnerable cells are those which the local blood vessels can no longer supply after being blocked off by the ischaemia, but remain viable due to oxygen supply from the surrounding arteries. If medical intervention arrives in time (usually before around 4½ hours after the inception of the ischaemic event), these cells may be able to regain functionality. Vulnerable cells are usually contained in the *penumbra*, a region of the brain neighbouring the *ischaemic core,* an area where the cells die immediately due to all supply being cut off. For decades, the identification of the penumbra region has been the topic of much research. Yet, despite advances in imaging techniques,

the delineation of the penumbra has been fraught with controversy. Our mathematical model helps to provide a theoretical approach to penumbra identification, helping to assist clinicians to decide whether or not to proceed with intervention. The model input is the cerebral blood flow, which is clinically measureable, and this leads to predictions of the calcium concentrations within the cell, damage and, finally, the eventual fate of the cell: whether they remain alive, die or form part of the penumbral region. This will be discussed in more detail in the thesis.

Each chapter covers a different aspect of our mathematical model. Chapter 2 covers the background literature motivating our model. This chapter, itself, comprises three sections: the relevant biology behind the causes and effects of an ischaemic stroke; previous attempts at mathematical modelling of ionic transport during ischaemic stroke, since we have incorporated elements of several models in the literature into our own and, finally; an investigation into a phenomenon known as *Turing instabilities*, which are patterns caused by spatial inhomogeneities appearing in certain reaction-diffusion equations. The importance of this final section lies in the fact that a mathematical model which forms Turing patterns can potentially show the ischaemic core, penumbra and unaffected regions.

Chapter 3 introduces the first portion of our model; calcium ion transport. Here, we propose a simple linear model that takes, as input, the cerebral blood flow reduction after ischaemia and predicts the subsequent calcium concentrations in the neurons, astrocytes (the two types of brain cells) and also the extracellular space surrounding them. Known to be a biomarker for ischaemic stroke, calcium ions have only been modelled in conjunction with other ions in stroke models (to our knowledge). Hence, our model simplifies these more complex models, with calcium ions playing the role, here, of being the sole biomarker.

Having predicted calcium ion dynamics in the brain after a restriction in blood flow, Chapter 4 discusses how changes in calcium concentration may damage cells. Here, our work is based on two models: first, the DeGracia model [7], which focuses not on modelling all the different forms of injury separately before coupling them together but combines them all into one equation instead.

This negates the need to model each form of damage, which may involve several processes of little other relevance to ischaemic stroke. Similarly, the DeGracia model also predicts the magnitude of stress factors generated; these are all the mechanisms the body undertakes to counteract the damage. If the magnitude of damage does prevail over that of the stress factors, we then proceed to the final part of the model: cell fate. Here, we draw inspiration from a model by O'Neill *et al.* [8] which hypothesises that a cell can be in one of three states: alive (undamaged and with adequate blood supply), vulnerable (functioning cells with limited supply, typically found in the penumbra) and dead. Alive cells become vulnerable after restriction of blood flow but this process is reversible: there is an opportunity for the vulnerable cells to be salvaged. If, however, supply continues to be unavailable, then vulnerable cells die: this is a unidirectional process. Hence, the model presented in this chapter takes, as input, the magnitude of injury inflicted upon a cell and predicts whether a cell will survive, die, or requires intervention. This potentially offers clinicians a tool to decide whether to attempt the salvaging of vulnerable cells.

Chapter 5 focuses on how to couple the two models presented in Chapters 3 and 4 such that the resulting model shows the ischaemic core, penumbra and unaffected regions. Since the diffusion terms in our equations are typically assumed to homogenise any spatial variations, the model must be modified in order for inhomogeneities to appear. Specifically, we determine how Turing patterns can form by modifying the two partial differential equations present in the model and show that further feedback terms are required. Subsequent coupling of the two models investigated in Chapters 3 and 4 ensures spatial patterns in the absence of feedback. However, in its presence, patterns appear only in the components before the O'Neill model, due to the 'all or nothing' nature of DeGracia's model and the smaller oscillations of the patterns formed.

Chapter 6 involves the discussion and conclusions gained from the previous chapters. Here, we emphasise the clinical relevance of our work and discuss potential future work. We conclude that the model displays Turing instabilities, though not in the presence of feedback, and so suggest further modifications allowing spatial patterns to form. This would subsequently allow our model to

be used as a guide for clinicians, allowing them to decide whether or not to salvage vulnerable cells after ischaemic stroke.

Before continuing, we point out one more aspect of our work: throughout the thesis, very little quantitative modelling (fitting) is done. Instead, our philosophy is to show the (very rich) qualitative features that our model can display and to relate these back to physiological mechanisms. The reason behind this is that we understand that modelling processes in biology is not a trivial task, especially in humans; because of the way we have evolved, many processes are involved in any given variable and, moreover, nature tends to add noise to accompany all of her subjects. Hence, our approach to modelling these processes is to start from the most basic model possible (reducing the number of parameters involved) and adding equations/terms only when the variable is of particular interest. In the words of Albert Einstein, mathematical models should be, “As simple as possible, but no simpler.” Our wish is to reflect this philosophy in our work.

Chapter 2: Literature Review

Then felt I like some watcher of the skies
When a new planet swims into his ken;
Or like stout Cortez when with eagle eyes
He star'd at the Pacific — and all his men
Look'd at each other with a wild surmise
'On First Looking into Chapman's Homer', John Keats

2.1 Introduction

Mathematical modelling is the art of representing a system using mathematics. The resulting model may elucidate how and within which limits the system works. A model describing some biological process is especially interesting. Biological systems are usually affected by random variations (e.g. genetically identical cells can grow to different sizes) and involve many feedback systems and redundancies to negate the possibility that parts of the system stop working. Moreover, it is still unclear how many pathways work, despite extensive experimental research. For this reason, mathematical modelling in biology remains an important tool to help our understanding of such systems. In addition, there are many types of models in our toolkit: those based on ordinary differential equations (ODE) and partial differential equations (PDE), stochastic systems and agent-based models, to name but a few that are used in the field. ODE/PDE models are deterministic; they represent a system in the absence of random effects and are extremely common in biomathematics, where they have been used to examine, for instance infectious diseases, glaucoma, blood flow, disease spreading and ecological issues [9][10][11][12]). Stochastic systems, on the other hand, include some source of random 'noise'. The addition of this noise is an attempt to mimic the stochasticity inherent in an actual biological system, resulting in a more complex model. Stochastic models have been developed to investigate phenomena such as ion transport [13]. Agent-based models are also popular in mathematical biology, being applied in areas such as immunology, ecology and oncology [14]–[16]. These models are so named because each 'agent' (or variable) in the model interacts with the others in a manner strictly determined by a set of rules, which are

representative of the interactions of these agents observed in biology. In this thesis, the biological event that we are primarily interested in is ischaemic stroke. Specifically, we construct a mathematical model to enhance our understanding of the role of calcium ions during a stroke. To this end, we must, first, understand how blood flow to the brain is maintained (Section 2.2), second, examine some of the existing mathematical models in the literature and say how they may be improved (Section 2.3), before finally examining Turing Instabilities (Section 2.4), a phenomenon whereby a system displays patterns in the presence of diffusion and which may be relevant in the modelling of ischaemic stroke.

2.2 Brain Physiology

The brain is the controlling hub of the body, though its mass consists of only around 2% of the entire body. Its many functions include processing external signals, making decisions and directing cells in the body to react to these signals, memorisation and emotional and behavioural reactions [6] .

This section focuses mainly on the organisation of the brain at the cellular and vascular levels. We will also briefly examine the major brain anatomy here. All of the brain can be divided into three parts: the cerebrum, cerebellum and brainstem. The cerebrum is the largest of these and controls higher-order functions, such as speech, emotions, learning and fine motor control. The cerebrum, itself, is divided further into the left and right hemispheres. Each hemisphere controls the opposite side of the body and, hence, if a stroke affects the left hemisphere, it is the right side of the body that is subsequently impaired. In addition, each side of the cerebrum is responsible for different tasks; the left appears to control aspects such as speech, memory and linear, logical thinking, whereas the right helps with creativity, intuition, emotions/empathy and ‘big-picture’ thinking. Each of these hemispheres can be further subdivided into four lobes: frontal, parietal, occipital and temporal. Each of these lobes performs its own set of tasks. The frontal lobe, for instance, controls one’s emotions, helps with problem solving, speaking and writing.

The cerebellum lies just underneath the cerebrum and controls muscle movement and balance. The brainstem connects the other two regions to the spine and regulates functions such as breathing and heart rates, body temperature and circadian cycles.

We now examine the cellular level structure of the brain. In humans, the brain contains trillions of cells, all of which can be divided into two groups: neurons and glia cells [6]. There are approximately 100 billion neurons in the brain and each one of these cells is connected to several other neurons. There are also approximately 10 trillion glia cells, mechanically holding those cells in place. Although these glial cells were presumably thought to be mere 'bystanders' to the neurons, recent research suggests that they, in fact, play many critical roles, such as providing oxygen and other molecules to the neurons, as well as eliminating pathogens infecting the brain [6].

Such an important organ has many components and requires considerable maintenance: its cells must be continuously nourished by the surrounding blood vasculature with nutrients and its intracellular ion concentrations, especially the calcium ions, maintained in homeostasis [6]. This is because a lack of oxygen transport is linked to calcium imbalance which, as we shall see in Section 2.2.4, may result in imbalances in other ions and the subsequent occurrence of an ischaemic event. In this subsection, we focus on describing the main components of the brain relating to stroke, how it uses the energy supplied to it and what happens to its cells when it cannot maintain a stable calcium concentration.

2.2.1 Constituents

The brain can be thought of in terms of its basic components: the blood vessels (arteries, capillaries and veins), brain cells (neurons and astrocytes) and the extracellular space. Here follows a discussion of the role of each of these components in maintaining brain function.

2.2.1.1 Cerebral Vasculature

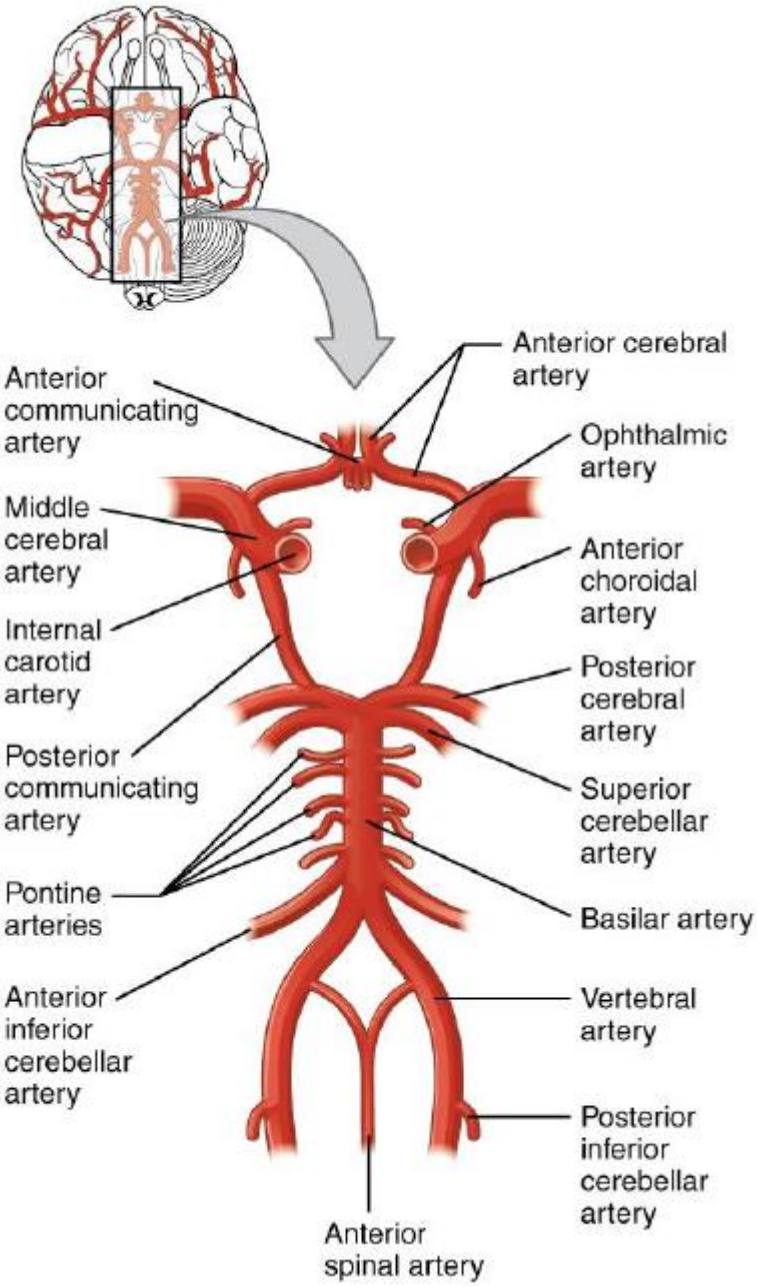

Figure 2.1: A schematic of the larger arteries in the brain, including the Circle of Willis. Reproduced without changes from OpenStax College under license http://creativecommons.org/licenses/by/3.0/.

Every cell in the body needs a constant supply of oxygenated blood to survive and this is especially so for those in the brain. In humans, the red blood cells (also known as *erythrocytes*), are the primary deliverers of this oxygen and these cells bring oxygenated blood from the heart, travel through arteries to the brain (and other cell types), before 'squeezing' one by one through the tiny

capillaries that branch out from these arteries. In this way, oxygenated blood reaches every cell in a healthy brain.

Four large arterial vessels bring oxygenated blood from the heart up to the brain: the left and right internal carotid arteries and left and right vertebral arteries (see Figure 2.1). Here, however, is where the blood supply to brain tissue differs from supply to the tissue of most other organs. Instead of branching off into smaller capillaries directly, the four vessels mentioned above are indirectly linked to each other by a structure known as the *Circle of Willis,* a ring-like structure comprised of 9 arteries that sits at the base of the pituitary gland. The Circle of Willis is the brain's ingenious solution for the need to maintain a constant blood supply to its cells: the arrangement of the arteries in the Circle of Willis allows for redundancy in case of vessel blockage. Even if one vessel experiences a restriction in perfusion, blood can still travel to the brain along the path of the unblocked vessels. This is known as *collateral circulation*.

In a manner so peculiar to biology, however, one finds that many people lack several of these structures. Indeed, studies by Papantchev *et al.* and Alpers *et al.* using advanced imaging techniques found that only approximately 50% of patients with neural dysfunction had a circle of Willis with all 9 vessels present [17][18]. People lacking a particular vessel remain unaffected unless a blockage occurs at the no-longer redundant vessel 'opposite' to the missing structure. Papantchev *et al.* showed that 35% of their 500 patients did not have a left posterior communicating artery, leaving them at risk of hypoperfusion of the middle cerebral artery [17].

In a healthy individual, blood leaving the Circle of Willis subsequently reaches the brain tissue first through one of six major arteries, before these branch out into smaller arteries and, finally, the capillaries. Capillaries take up around 0.5% of the brain's volume and are the vessels through which oxygen-carrying blood is able to deliver the oxygen to the cells in the brain, before carrying carbon dioxide back to the heart. Being so small in diameter (5-10 μm thick) and having only a membrane (endothelium) one cell thick, the capillaries are optimised for allowing small molecules, such as

oxygen, to diffuse in and out. In addition, all capillaries supplying the brain have a blood-brain barrier, which is a partially permeable membrane allowing diffusion of water and gases such as oxygen, as well as the transport of certain molecules, such as glucose, that the brain requires. The barrier also prevents toxic molecules from entering the brain, ensuring the brain remains unharmed by such chemicals.

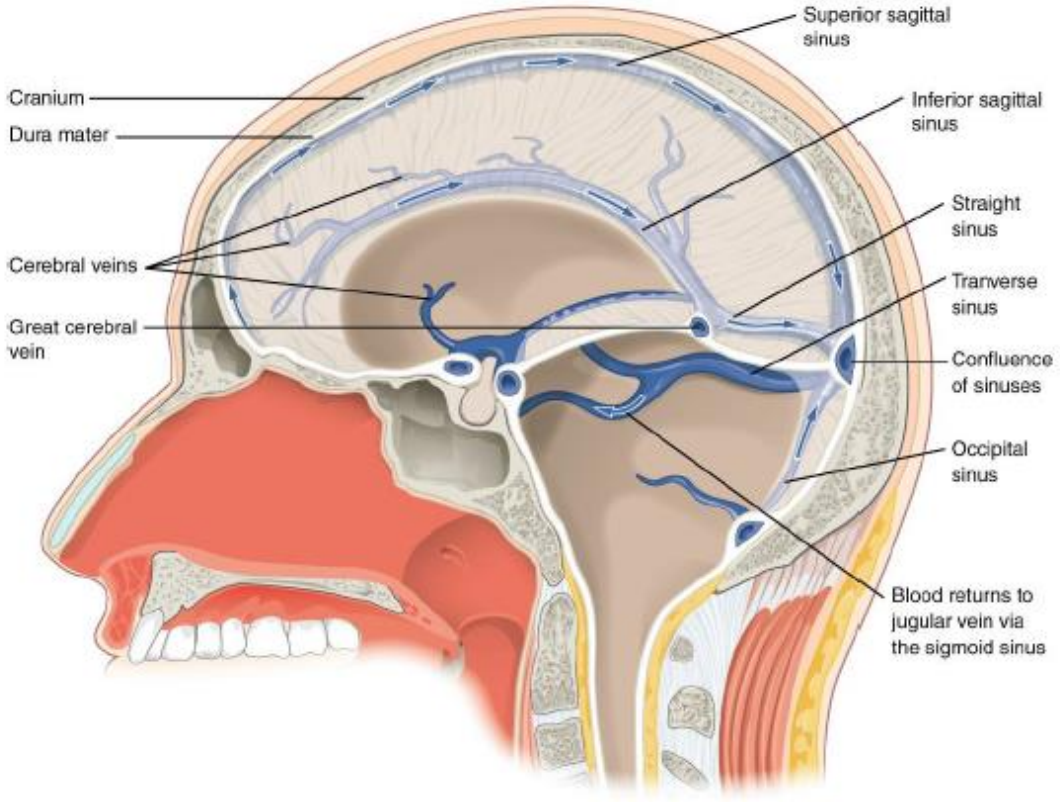

Figure 2.1: A schematic of the large veins in the brain. Reproduced without changes from OpenStax College under license http://creativecommons.org/licenses/by/3.0/.

After the delivery of oxygen to each cell, blood returns to the heart through the veins. Figure 2.2 shows the major veins of the brain. Subsequently, the deoxygenated blood moves across the smaller veins towards the confluence of sinuses at the back of the head and then to the jugular. From there, it enters the superior vena cava, eventually reaching the heart, where it is pumped to the lungs to receive a fresh supply of oxygen.

2.2.1.2 Neurons

Neurons are brain cells, approximately 100 billion in number in a typical adult brain. They respond to chemical or electrical signals by outputting an action potential. First, a neuron is activated by a stimulus: for instance, a neuron connected to the finger is activated when the finger touches an object. This electrical stimulus then triggers an action potential, which subsequently propagates down a series of neurons. This propagation is due to the movement of ions (usually sodium and potassium) into the cell through ion channels. Neurons take up approximately 45% of the total brain volume.

The concentration of calcium in the neurons is approximately 100nM under resting conditions [20] but a small increase in intracellular calcium concentration (from 100 to 300nM) may lead to apoptosis [21], whereas a large increase (from 100nM to 1000nM) may cause necrosis [22]. The process by which a transient calcium increase causes apoptosis is described in more detail in Section 2.2.4.2.

2.2.1.3 Astrocytes

Astrocytes are a type of glial cell and are the most common type of brain cell, taking up approximately 25% of the total brain volume. Amongst their many functions, we focus upon the following. First, glycogen can be stored only in astrocytes and not neurons. The maximum concentration of glycogen observed is 4.2mM [23]. This is the desired concentration level when the cell is at rest; however, during hypoglycaemia, when glucose levels are abnormally low, these glycogen stores can start to be converted to glucose and fed back to the cell.

Second, astrocytes are able to uptake calcium ions from the extracellular space (see Section 2.2.4.2). Third, glutamate can be released by the astrocytes, which then can cause 'glutamatergic currents' in neurons of around -400pA. The release of glutamate depends on the level of astrocytic calcium [24]. Like other brain cells, the concentration of calcium in the astrocytes is around 100nM [20]. However, it has been shown that an increase from 85nM to 140nM in intracellular calcium causes currents of about -400pA in adjacent neurons [24].

2.2.1.4 Linking Cerebral Vasculature and Cellular Processes

When cerebral vasculature is in healthy condition, neurons and glial cells can function properly. In the event of an ischaemic stroke, however, a thrombus narrows the arteries supplying the brain tissue, leading to a lack of oxygen received by this tissue, which can then lead to its death. This process is explored further in Sections 2.2.4 and 2.2.5. One typically observes a particular spatial distribution after ischaemia. Three regions make up this distribution: the *core*, *penumbra* and *unaffected space* (see Figure 2.3).

This Figure has been redacted due to copyright issues

Figure 2.3: Schematic showing the ischaemic core and penumbra regions of the brain after ischaemia. Originally taken from Fisher and Saver [25]**.**

The ischaemic core is the region where perfusion falls below a threshold, typically taken to be 20 ml/100 grams/minute. Cells in the core thus have an insufficient amount of oxygen supplying them and die shortly after ischaemia from necrosis (see Section 2.2.4.3). The unaffected region is where perfusion remains unaffected after the stroke and, hence, cells here continue to function normally. In between the core and unaffected region, one finds the zone known as the penumbra. While blood flow to the tissue here is also restricted, there is enough supply from collateral arteries to keep the tissue alive for several hours after ischaemia. This presents clinicians with a window of opportunity in which they can potentially salvage cells in this region by reperfusion; the drug known as recombinant tissue-plasminogen activator (rt-PA) promotes the breakdown of blood clots but may also lead to haemorrhage. Hence, clinicians must weigh up the potential risks and benefits when deciding whether or not to intervene. Finally, we note that, even though the penumbra is potentially

such an important region clinically, its demarcation is still fraught with difficulty, despite the availability of advanced imaging techniques.

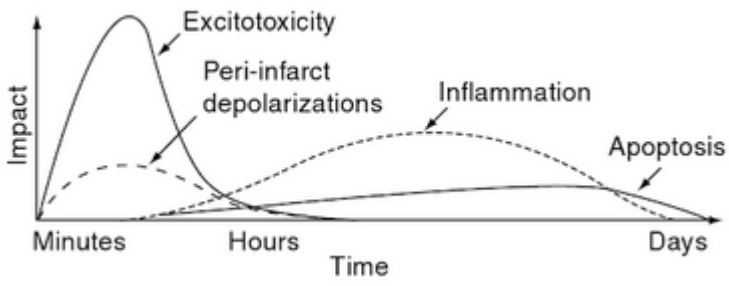

Figure 2.4: The typical timescales of an occurrence of ischaemic stroke is shown. Reproduced from Gonzalez [19].

It is worthwhile examining the timescales of a stroke, which Figure 2.4 elegantly illustrates. Within minutes of a stroke occurring, cells in the brain are killed through a process known as *excitotoxicity*. This involves the influx of calcium ions (see Section 2.2.3) into the cell; these ions subsequently cause cell death by two mechanisms: necrosis and apoptosis. The former acts much more quickly (a matter of minutes) while the latter is more orderly and takes hours or days to complete (see Section 2.24). Inflammation of brain tissue can also occur, starting a few hours after the onset of ischaemia.

2.2.1.5 Extracellular Space

The extracellular space is defined as all the volume of the brain outside the cells and capillaries, taking up about 20% of the volume of the brain. It is commonly assumed that molecules such as oxygen and carbon dioxide are able to diffuse from the capillaries to neurons/astrocytes, and vice versa, directly; the extracellular volume is bypassed during their diffusion.

The concentration of calcium in the extracellular space is around 1mM, which is about four orders of magnitude larger than the intracellular concentration [20]. This causes a concentration gradient to be formed, one of two forces that tend to push calcium into the cells. This increases the intracellular levels enough to drive the cell to apoptosis or necrosis. Hence, there are two pumps that force the calcium back into the extracellular space to maintain constant concentrations inside and outside the cell. This is discussed in more detail in Section 2.2.4.2.

2.2.2 Energy Usage in the Brain

Although only 2% of the body's mass comes from the brain, it uses 20% of the body's oxygen and 25% of its glucose [26]. The brain is a unique organ in that it has few energy stores compared with other organs, such as the liver and skeletal muscles and, thus, relies on a continuous stream of incoming molecules to provide it with energy. If, however, cells in the brain are starved of oxygen for only one minute, cell function begins to be lost. Hence, it is important to examine how the brain uses the energy molecules that are essential for its survival. This section explores how Adenosine Triphosphate, the cell's primary energy 'currency', is converted from Adenosine Diphosphate during the breakdown of glucose. We also briefly explore the theory of the 'lactate shuttle', which theorises that astrocytes, which contain the only energy reserves in the brain, can break down these reserves to give lactate during hypoglycaemia (when blood glucose is low), and that this lactate is then 'shuttled' over to the neurons as a source of energy, keeping them alive for a further 20 minutes, approximately [23] [27]. The lactate shuttle remains a controversial theory, as traditionally the brain has been thought to have no energy reserves; indeed, an increasing body of evidence appears to argue against it [28] [29] [30].

2.2.2.1 Adenosine Triphosphate (ATP)

Adenosine Triphosphate (ATP) is the most important energy-providing molecule in the body. The three phosphate groups (hence the triphosphate in the name) are adjacent to one another. This means that the negatively-charged oxide ions that make up these phosphate groups greatly repel one another. Hence, one of the three phosphate groups tends to separate from the molecule; when this occurs, adenosine diphosphate (ADP) is formed, with the release of approximately 30kJ energy per mole [6].

2.2.2.2 The Three Fates of Glucose

Glucose is a major source of energy for cells in the human brain. There are three pathways that glucose can traverse: the first two involve glucose breakdown, resulting in the formation of ATP,

from ADP, while the last involves its storage in the astrocytes. Figure 2.5 shows these three pathways in more detail, each of which is also discussed further below.

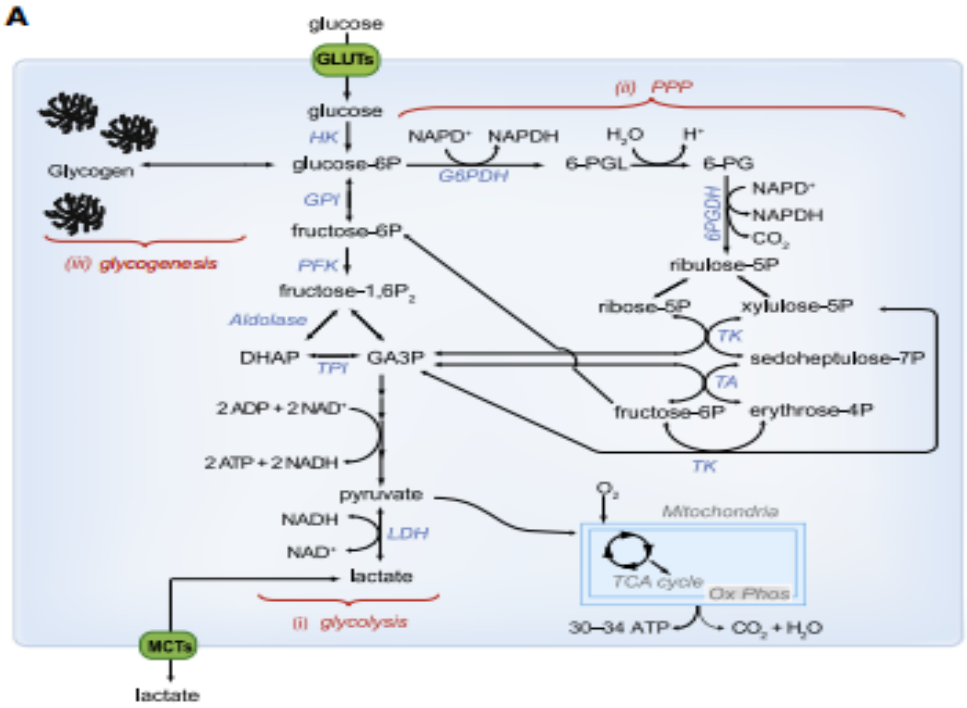

Figure 2.2: The three paths involved in the breakdown of glucose in the brain, showing: (i) the glycolysis pathway, (ii) the pentose phosphate pathway (PPP) and (iii) storage in the astrocytes (glycogenesis). Reproduced from Belanger *et al.*[26].

2.2.2.3 Glycolysis

The first of the three metabolic pathways by which glucose can be processed is glycolysis, shown in Figure 2.1. Here, one molecule of glucose is converted into two molecules of pyruvate, along with two molecules of ATP and two molecules of Nicotinamide Adenine Dinucleotide Phosphate (NADH). At this point, the pyruvate is available for processing in two more pathways: aerobically or as lactate. The former occurs in the presence of sufficient oxygen and is considered more energy-efficient, giving 30-34 molecules of ATP per glucose molecule, whereas the lactate pathway produces no further ATP or NADH other than those produced by glycolysis. However, the lactate pathway may be of significant importance in brain metabolism [26], [31], [32] - if, indeed, the theory is valid, having met much opposition in the scientific community [28] [29] [30].

Figure 2.1 shows, in more detail, these two pathways: aerobically, pyruvate enters the mitochondria

and goes through the Krebs' cycle and the oxidative phosphorylation processes. A large number of interactions occur here but, for our purposes, we summarise these interactions by saying that the result is that pyruvate is broken down to acetyl CoA, which allows both Nicotinamide Adenine Dinucleotide (NAD) to be converted to NADH, through the addition of energy-containing electrons, and also the formation of carbon dioxide, which diffuses to the capillary vessels. The NADH molecules then transfer their energy in the process of oxidative phosphorylation to convert ADP to ATP. This process is sometimes referred to as aerobic glycolysis.

In the absence of sufficient concentration of oxygen, however, oxidative phosphorylation cannot occur and, hence, pyruvate does not enter the mitochondria. Instead, it is converted to lactate, which exits the cell through monocarboxylate transporters. This process is referred to here as glycolytic metabolism. We also note that lactate can be converted into pyruvate as well; this 'reverse' process will be important in the lactate shuttle, described in Section 2.2.2.7.

Though it seems that it would be far more efficient for the energy-needy brain to use aerobic respiration to process glucose, it has been shown that the lactate pathway is important too; in Section 2.2.2.6, we shall thus examine the role of lactate in more detail.

2.2.2.4 The Pentose Phosphate Pathway

A second pathway for glucose to take is that, after being converted to glucose-6-phosphate, it enters the pentose phosphate pathway (PPP). After a series of reactions, depicted in Figure 2.1, the result is that fructose-6-phosphate is formed, together with NAPDH.

2.2.2.5 The Storage of Glucose as Glycogen

The third pathway that is available for glucose to take is to be stored as glycogen, as shown in Figure 2.1(iii). Glycogen is a molecule that is stored in the body as an energy reservoir. The glycogen stores are used up during periods of high energy demand and also replenished when demand is lower. In the brain, only astrocytes, and not neurons, are able to store glycogen and these stores are relatively few compared with those found in other organs, such as the skeletal muscles. Glucose from the

extracellular space reaches these astrocytes and is transformed to glucose-6-phosphate (G6P). From this molecule, two paths can be taken: the first is glycolysis, which leads to ATP production (see Section 2.2.2.1), while the second is glycogenolysis, where the G6P is converted to glycogen.

In most instances, the glucose will be used up to produce ATP. If, however, the glucose reaching the astrocytes is surplus to energy requirements, which is usually the case if the cells are in a resting state, the glucose will undergo glycogenolysis, so long as the glycogen concentration does not exceed the 4.2 mMol limit observed by Brown and Ransom [33]. When the energy stored in glycogen is required, glycogen is reconverted to G6P, ready for glycolysis.

2.2.2.6 Lactate Transport

Lactate is a molecule that is produced after glycolytic metabolism of glucose. As discussed in Section 2.2.2.1, this is not the most efficient method of metabolism. However, experimental evidence suggests that glycolytic metabolism is ongoing throughout the brain, even during the resting state, and that it rises sharply in proportion to oxidative phosphorylation during ischaemia [34]. Indeed, it has been suggested that lactate is a major source of energy for brain cells. The lactate shuttle is one theory which attempts to explain this paradox.

2.2.2.7 Lactate Shuttle

The lactate shuttle is a controversial mechanism proposed by Pellerin and Magistretti [32] and depicted in Figure 2.2. After neuronal stimulation, labelled V_m in the figure, glutamate is released from the presynaptic cleft, and some of this molecule acts as an excitatory neurotransmitter and excites the next neuron. However, there is also a proportion of glutamate that goes, instead, to the astrocytes. In order to enter the astrocytes, however, the glutamate must pass through a sodium co-transporter; hence, sodium ions enter simultaneously. These ions then leave the astrocytes via sodium-potassium ATP pumps, which exchange three sodium ions out of the cell in exchange for two potassium ions into the cell. The cost of driving these ions against their concentration gradients is that ATP must be converted into ADP, a process requiring energy.

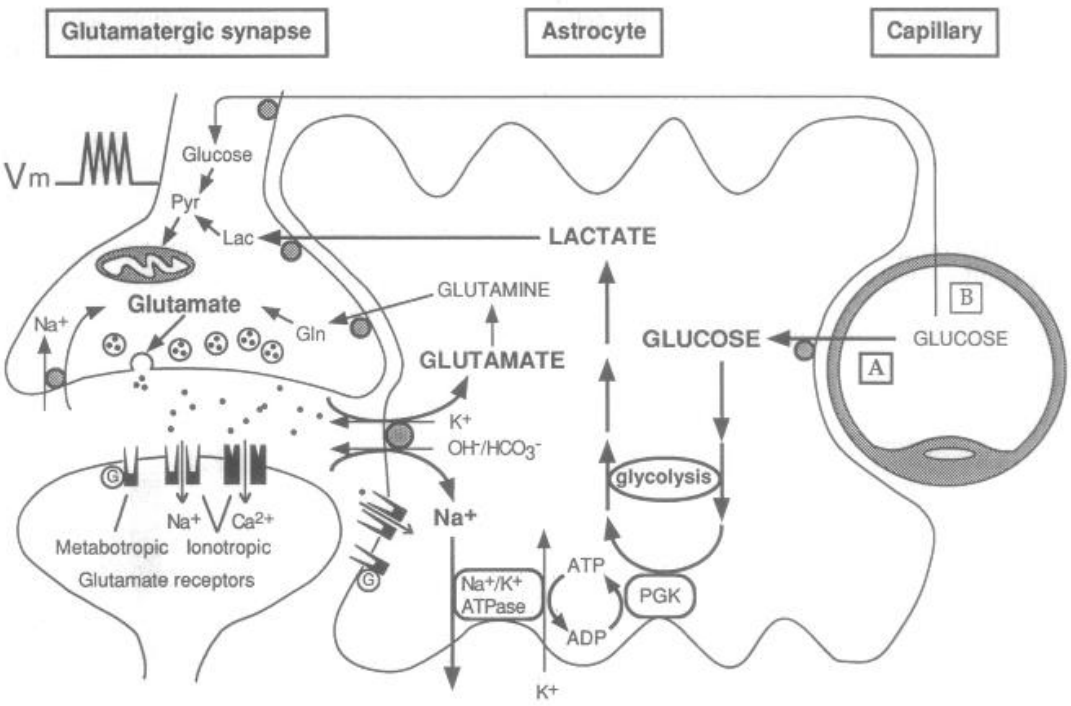

Figure 2.6: Schematic of the astrocyte-neuron lactate shuttle. Reproduced from Pellerin and Magistretti [32].

This process, in turn, activates glycolysis in the astrocyte. Lactate is subsequently produced. This lactate is able to leave the astrocytes, going into the neurons, where it can be converted to pyruvate. Pyruvate then undergoes aerobic respiration in the mitochondria, producing ATP. Thus, the neurons are able to use lactate formed in the *astrocytes* as a major source of energy; the 'classical' theory states, on the other hand, that, since the brain requires such a high proportion of energy in comparison with its size, it must require glucose to undergo oxidative metabolism instead of glycolytic metabolism [32].

2.2.3 Calcium Ions: Distribution, Maintenance and Functions

Calcium ions are necessary for many cellular processes. These include, but are certainly not restricted to [35]: a calcium ion influx from the Sarcoplasmic Reticulum (SR) to enable contraction in cardiac muscle, synaptic plasticity and, importantly for this work, they function as a second messenger, triggering, upon their release from the SR, the activation of proteins which, in turn, trigger other proteins in a cascade leading to apoptosis (this is discussed in Section 2.2.4.1).

These processes all require that the intracellular calcium ion concentration be regulated tightly: typically the intracellular calcium concentration is approximately 100nM, while the extracellular concentration is several orders of magnitude greater, at approximately 1mM. In addition, the intracellular component is also around 60mV lower in potential than the extracellular. Driven by these two gradients – the electrical and chemical – calcium ions tend to diffuse into the cell via calcium channels. The diffusion coefficient of calcium ions in the cell is around 5×10^{-6} cm/second, although this depends on the obstacles it encounters. Movement through the channel costs no amount of energy, since the process is diffusion. Calcium pumps move the ions back out of the cell. The process of opening the gates of the pump and the subsequent expulsion of calcium takes milliseconds to occur. As their name suggests, the ATP-powered pumps require energy to function; this energy is provided by hydrolysis of ATP molecules. Channels and functioning pumps are crucial for maintaining the concentration of calcium ions at around 100nM. Cell functions cease to be effective at higher levels and the cell may even undergo apoptosis. In the following subsection, we examine some of the key components and processes involved in calcium ion homeostasis.

2.2.3.1 The Sarcoplasmic Reticulum

The Sarcoplasmic Reticulum (SR) is a series of tubules found in muscle cells, neurons and astrocytes, within which calcium ions are stored. The concentration of calcium ions here is approximately 1mM, compared with 100nM in the cytoplasm. Under normal conditions, the SR can maintain homeostasis of intracellular concentration by releasing its vast store of calcium [36]. The store is replenished by active transport of calcium through Ca^{2+}-ATPase pumps, which we describe in Section 2.3.3.

2.2.3.2 Calcium-Induced Calcium Release (CICR)

Calcium-Induced Calcium Release occurs after calcium ions enter the cell from the extracellular space, causing the release of more calcium ions from the SR into the cell. CICR plays an important part in the contractions and relaxations of cardiac tissue. In addition, CICR is thought to have a role

in other types of cells/tissues – both glial and neuronal cells have been hypothesised to undergo CICR.

2.2.3.3 Sarco/Endoplasmic Reticulum Ca^{2+} ATPase (SERCA) Effects

After the effects of CICR, calcium ions must be pumped back into the SR to maintain the former concentration gradient. Within the sarcoendoplasmic reticulum resides an ATPase known as the Sarco/Endoplasmic Reticulum Ca^{2+} ATPase (SERCA). The enzyme transports calcium ions from the cytoplasm back into the SR, replenishing its supply. This is achieved at the cost of the hydrolysis of ATP. Calcium release from these stores is of the order of milliseconds [37].

2.2.3.4 Cell Membrane plasma membrane Ca^{2+}-ATPase pump

Another calcium pump resides in the cell membrane: the plasma membrane Ca^{2+}-ATPase. Like the SERCA pump, the energy gained from ATP hydrolysis allows active transport of calcium ions from within the cell to, in this case, the extracellular space. This is another process of calcium influx, taking on the order of milliseconds.

2.2.3.5 Summary

As can be seen, both intracellular and extracellular calcium ion concentrations are tightly regulated. Ischaemic stroke causes these pumps to lose functionality due to a lack of ATP formation, causing calcium ions to move into the cell, down their concentration gradient. When some threshold is exceeded, these calcium ions trigger processes that cause cell death; this is discussed in the following subsection.

2.2.4 Cell Death and the role of Calcium Ions

There are twelve known ways in which a cell may die [38]. In this thesis, we are chiefly concerned with apoptosis and necrosis, as they are the two fates mostly suffered by anoxic cells [39].

Apoptosis is a mechanism whereby internal signals drive the cell to an orderly, programmed, death. Necrosis, on the other hand, is a chaotic process where the cell is influenced by external factors to die.

More recent research has suggested that the overlap between apoptosis and necrosis may not be a null set. Indeed, a term 'necroptosis' has been coined to describe the necrosis of cells in an orderly manner [38]. Table 2.1 summarises the main differences between these two pathways.

	Apoptosis	**Necrosis**
Description	Programmed cell death driven by internal cell signalling	Cell death caused by external factors
Region primarily affected during ischaemic stroke	Penumbra	Ischaemic core
Time after stroke required to occur	Minutes (but post-apoptotic necrosis may also occur)	Hours/days
How calcium ions are involved	Triggers caspase cascade (section 2.2.4.1), leading to apoptosis	May be involved in post-apoptotic necrosis

Table 2.1: Summary of the main differences between apoptosis and necrosis.

Calcium ions are known to play a part in starting off both these cell death pathways, making them the centrepiece of this thesis. An imbalance in their cellular concentration triggers the activation of *caspases.* Caspases are enzymes that trigger processes such as apoptosis. They start off as procaspases and must be activated by signals, either external (or from already activated caspases, before going on to activate other procaspases (thus forming a caspase cascade). *Initiator caspases*, such as Caspase 8, once activated, start off the cascade, which ends in the activation of an *executioner caspase,* such as

Caspase 3. These caspases then trigger cell apoptosis. The following subsections describe the mechanisms leading to cell death in more detail.

2.2.4.1 *The Apoptotic Pathway*

It has been noted that apoptosis can be triggered by one of two pathways: the extrinsic or intrinsic pathway [34]. The extrinsic pathway, shown in Figure 2.3, causes apoptosis to occur by external 'death' signals. One example of this is the binding of Fas Ligand (Fas-L) to a receptor molecule. This forms the DISC (death-inducing signalling complex), which converts Procaspase-8 to Caspase 8 [34].

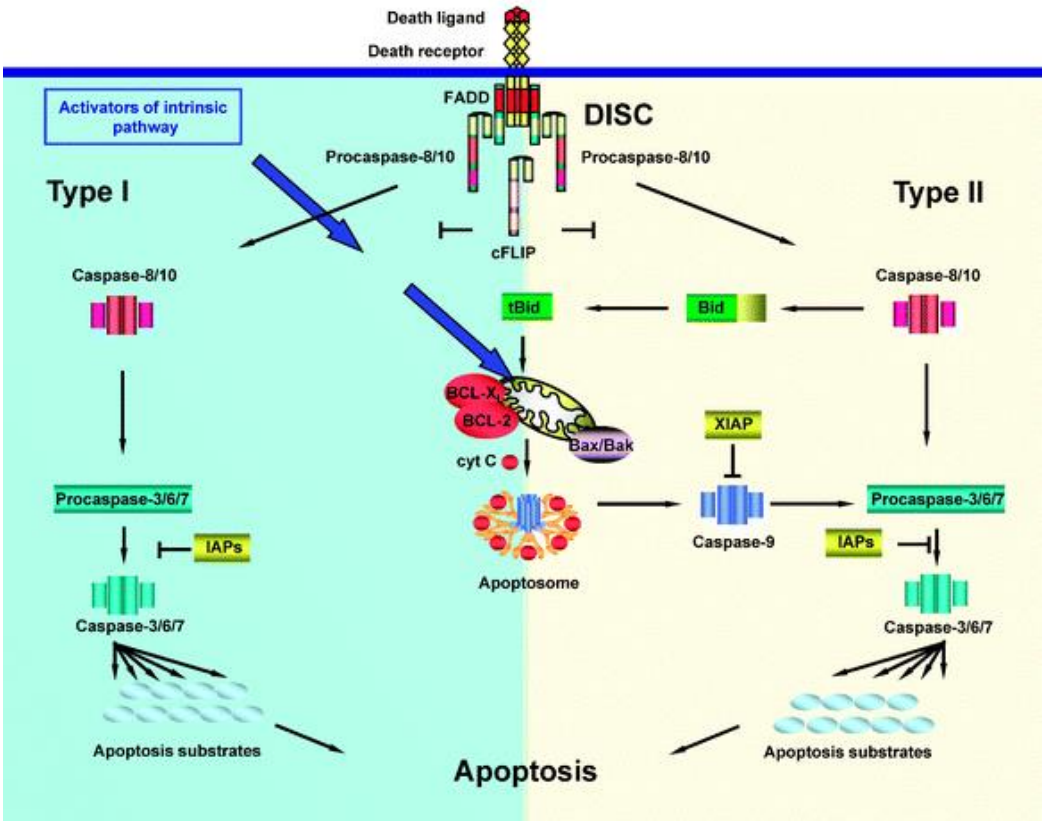

Figure 2.3: Schematic showing the intrinsic and extrinsic pathways of apoptosis. Reproduced from Lavrik *et al.* [40].

Subsequently, one of two paths is possible. The first occurs in Type I cells, which are defined as cells that do not require mitochondria-related processes to undergo apoptosis [34]. In these cells, caspase 8 is present in sufficient quantities to be able to lead to the conversion of other procaspases to their active caspase form, without the help of mitochondrial processes. A caspase cascade is thus triggered, with the final caspase activated being caspase 3. The second possibility occurs in Type II cells, defined

as cells requiring mitochondrial processes to be able to undergo apoptosis. Apoptosis occurs here when FasL binds to receptors on the cell, but the quantities of caspase 8 are insufficient; the effects of caspase 8 must then be amplified in the mitochondria before triggering the caspase cascade. The intrinsic pathway, also shown in Figure 2.3 occurs when apoptotic stimuli act directly on the mitochondria, releasing molecules such as cytochrome C, which form the apoptosome. This then triggers caspase 9 to activate caspase 3, leading to apoptosis. There is a large overlap between Type II cells undergoing apoptosis via the extrinsic pathway and cells undergoing intrinsically-mediated apoptosis, as shown in Figure 2.3. Ischaemic stroke is believed to cause apoptosis of brain cells through both extrinsic and intrinsic pathways [41].

2.2.4.2 The role of Calcium in Apoptosis

Calcium ions were suspected to be of pivotal importance when their influx corresponded to cell damage, as Nicholson *et al.* [42] found. The intracellular influx of calcium ions occurring in response to anoxia, an extreme shortage of oxygen being supplied to these cells, plays an important role in ischaemic stroke [21], [24], [34], [43].

Kristian and Siesjo assert that calcium ions are one of the triggers for cell death, no matter what the mechanism [43]. Since many studies report that this trigger is caused by calcium ions moving into cells from the extracellular space [21], [24], [34], [43], the control, or homeostasis, of calcium ion concentrations is of particular interest here.

In a normal, resting state, in addition to the calcium imbalance, the electric potential outside of the cell is also about 75mV higher than inside. Thus, both the concentration and electric gradients try to push the calcium ions into the cell. To counteract this push, there are two pumps located along the membrane that force the calcium ions back into the extracellular space: the Na^{+}-Ca^{2+} and ATP-consuming Ca^{2+}-H^{+} exchangers [43]. These two competing phenomena help to maintain intracellular calcium concentrations at around 100-200nM [43]. However, when the cell is triggered by an action potential, this homeostasis is no longer preserved and the intracellular concentrations spike dramatically, a process taking place over a few milliseconds.

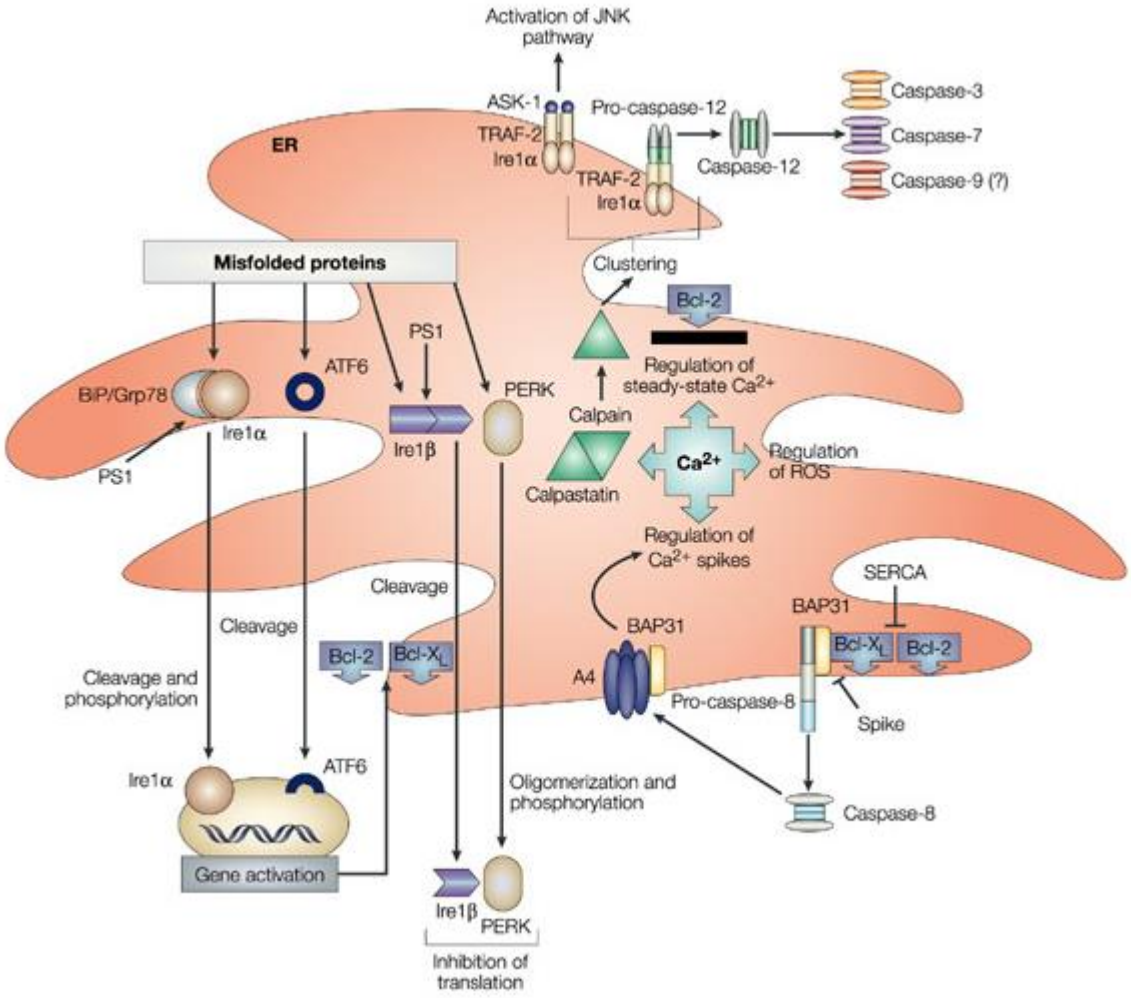

Figure 2.4: Changes in calcium concentration drive both intrinsic and extrinsic apoptosis pathways. Reproduced from Orrenius, 2003 [34].

This spike is caused by receptors, such as glutamate, opening calcium channels. Calcium ions then rush inside the cell. There, it is either stored in the endoplasmic reticulum or binds to proteins with calcium receptors, such as calmodulin. Such proteins then bind to procaspase-12, activating caspase-12, which itself triggers the caspase cascade. At the end of the cascade, Caspase 3 is activated and this final caspase then causes cell apoptosis. Furthermore, Caspase 3 is believed to be able to interfere with both the Ca^{2+}/ATPase and the Na^{+}/Ca^{+} exchangers [34], [43]. Hence, the cell loses more control of its calcium homeostasis. This loss of homeostasis will continue unless reperfusion occurs, for then the oxygen and, therefore, ATP supply to the cell enables the calcium pumps to function again.

What is interesting is that, under low levels of pH (under 7.0), calcium conductances through their

membrane channels fall dramatically [43], a drop arising from excitatory stimuli. pH levels have been shown to correspond, in part, to ischaemic damage [44]. Magnetic resonance imaging (MRI) techniques based on pH are currently available, producing pH-weighted MRI images, although these produce images only at single time-points during the condition [45]. Studies have also shown that there is a link between the initial magnitude of injury and the rise in calcium [34], [46].

2.2.4.3 The Necrotic Pathway

Necrosis was previously thought to be a chaotic stream of events leading up to a cell's ungainly death. Two hypotheses proposed in 1987, however, refined this definition; first, that the injury (here, the influx of calcium ions) needed to trigger apoptosis should be less than that required for necrosis and, second, that it is easier to necrotise a cell that has already been 'primed' for apoptosis [38].

Hence, as we have touched on previously, apoptosis and necrosis perhaps should not be seen as two completely distinct processes. Rather, they can occur to cells suffering from the same *type* of injury; which path an anoxic cell wanders down (in the case of ischaemia) depends on the *magnitude* of intracellular calcium influx. This may be why necrosis generally occurs to cells in the ischaemic core – these cells dying within minutes – while those in the penumbra, where intracellular calcium concentration is lower, largely undergo apoptosis.

As a final example of this, and again portraying how few phenomena in biology are truly black and white, research has shown that 'post-apoptotic necrosis' can occur in cells that have been flooded with caspases, in response to apoptosis; these caspases inactivate calcium channels in the membrane prevent calcium extrusion, building up the levels of calcium ions to such high levels that necrosis occurs [38].

2.2.4.4 Consequences of Stroke on Chemical Pathways

After ischaemic stroke, the cell experiences a lack of oxygen and, hence a reduction in ATP being produced. As mentioned previously, this may subsequently result in the loss of functionality in active

processes (those requiring, for instance, ATP–powered pumps). As the concentrations of ions in the cell are tightly regulated, loss of these processes can quickly lead to imbalance of chemicals, including calcium ions, about which we are primarily concerned.

In particular, there are two pumps that bring calcium ions back into the cell, to maintain the concentration gradient. These are the plasma membrane Ca^{2+}-ATPase and SERCA pumps; the loss of functionality in these pumps eventually leads to calcium ion depletion in the SR and, more crucially, an imbalanced intracellular calcium concentration. This affects the cell signalling pathways, triggering cell death.

2.2.5 Overview

As Figure 2.5 shows, a thrombus, which is caused by blood clotting over plaque-damaged arteries, results in reduced blood flow to areas of the brain further upstream. One common blood vessel where thrombus formation occurs is the carotid artery – this is often apparent in carotid artery disease. The thrombus leads to reduced blood flow and this, in turn, to less oxygen delivered to the cells. Since aerobic respiration no longer occurs, the amount of ATP produced decreases and, if this decrease is severe, then the ATP-powered pumps that maintain the concentration gradient of ions, such as sodium, potassium and calcium, cease to function.

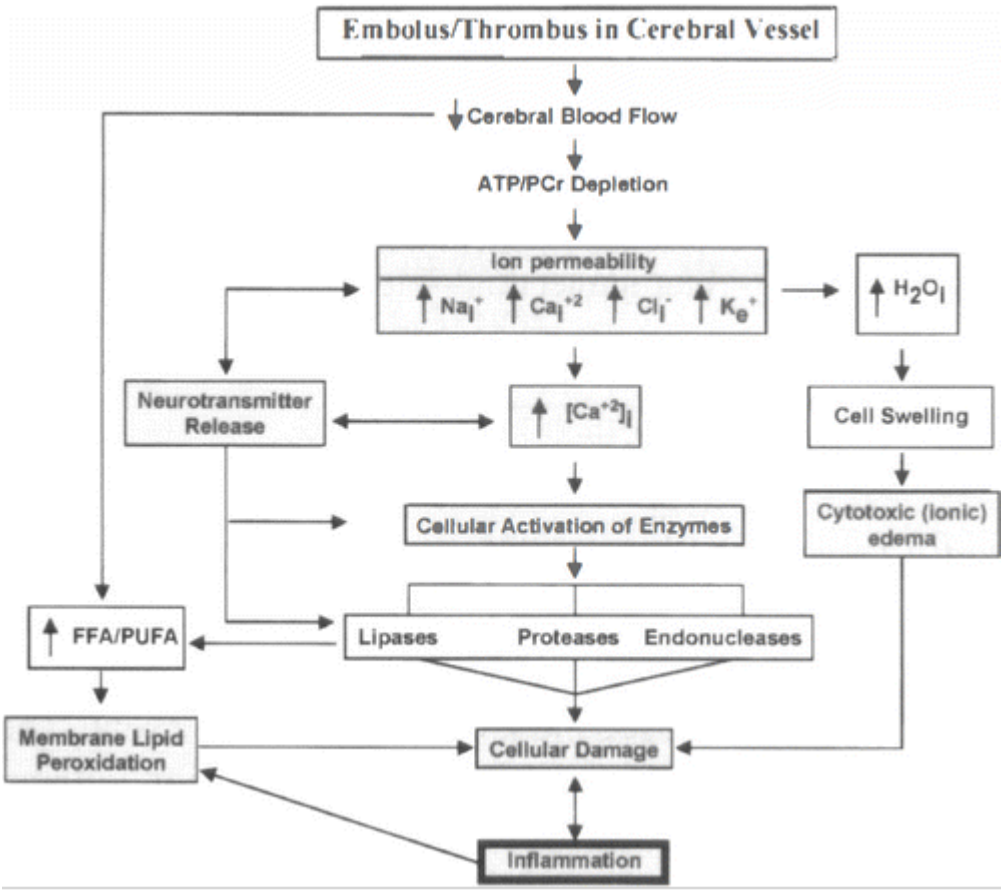

Figure 2.5: Summary of calcium-related events after stroke. Reproduced from Barone and Feuerstein [47]. Timescales of events: thrombosis – hours, ATP depletion – 1-3 minutes (Grotta *et al.*), ion permeability – minutes to hours, intracellular calcium concentration and neurotransmitter increase – milliseconds, water influx into cell, swelling and oedema – hours to days [49], cellular activation of enzymes – hours, cellular damage and inflammation – hours to days.

Figure 2.10 shows the typical timescales required for the above processes – these range from minutes/hours to days/weeks. As a result, the homeostasis of calcium ions that keeps the intracellular concentration several orders of magnitude lower than the extracellular can no longer be maintained. Suddenly, calcium ions can move down the concentration gradient into the cell; such an influx marks the beginning of the end of the cell, as it triggers cell death through apoptosis, necrosis or necroptosis. Cells residing in the penumbra, the region where perfusion from vessels immediately adjacent is restricted but cells continue to live as vessels from neighbouring regions continue to perfuse them, still stand a chance for survival, provided that oxygen returns to the penumbra within the window of opportunity, which is around 4½ hours after inception of the ischaemia.

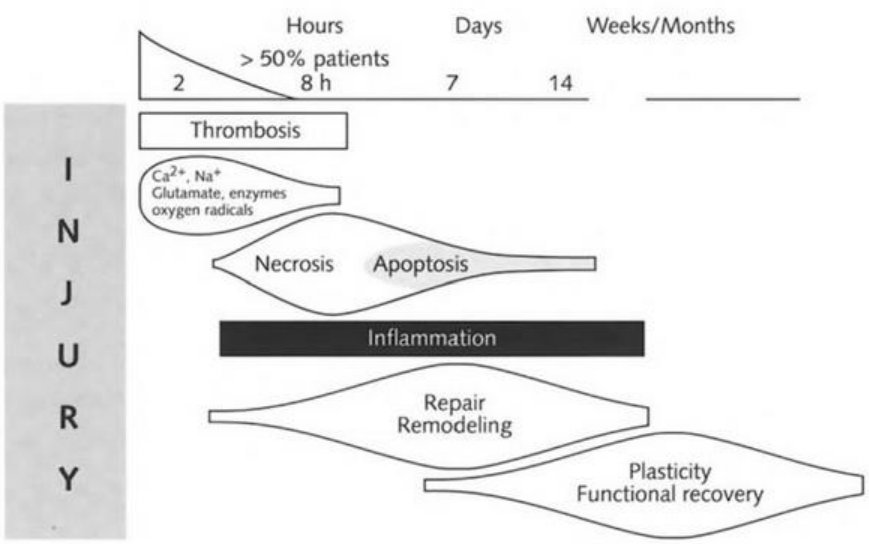

Figure 2.6: Schematic of timescales of events taking place after ischaemia. Thrombosis and ion imbalance take place over a few hours, as does necrosis but inflammation and apoptosis take longer (days), with repair and functional recovery taking weeks. Reproduced from Barone and Feuerstein [47].

2.3 Mathematical Models from Existing Literature

Having examined some of the biological details of the brain, we now examine some of the key mathematical models in the literature investigating ischaemic stroke [7], [50]–[56].

Seidenstein *et al.*[57] divide the current world of ischaemia modelling into two groups: those that investigate the cellular level and the others at the tissue/systems level. In brief, cellular level models (operating in the 100μm scale) describe the dynamics of chemical species in a cell after the onset of ischemia: what cellular processes spring into action or are disabled and how they ultimately affect the fate of the cell. Tissue level models, on the other hand, ($\geq$1mm scale) aim primarily to delineate the ischaemic core and penumbra.

Here, we shall focus mostly on cellular level models since we are interested in the role of calcium ions during stroke; their effects are usually described by cellular level mechanics. The cellular level models, themselves, can be further subdivided into which pathways they investigate: namely, the ionic/chemical transport, caspase networks, and cell damage/death models. This subsection examines existing models in each of these three categories in turn.

2.3.1 Models of Chemical/Ionic Transport

Most models of ischaemic stroke include equations describing the movement of chemicals around the brain. This section provides a description of some of the important features of these models and Table 2.2 summarises their similarities and differences. Duval *et al.* developed one of the first models of ischemic stroke [50]. Since this model did not include ion dynamics, Dronne *et al.*, [53], who were interested in identifying the penumbra region, further developed the Duval model by adding subsystems such as that for cytotoxic oedema, a phenomenon leading to cell necrosis (See Figure 2.6). In doing so, they required additional equations for other ion dynamics, namely K^+ and Ca^{2+}. Dronne *et al.* [55] then further developed the model to show the long-term ionic concentrations and their effect on the cytotoxic oedema process by adding the dynamics of Cl^- ions and modelling the actions of volume-activated channels, which expel Cl^- ions during oedema, pumps and exchangers, such as those mentioned in Section 2.2.

The model of Chapuisat *et al*. [52], developed in 2008, focuses on supporting or discrediting the theory of spreading depressions, a phenomenon where there is a temporary pause in neuronal activity, which eventually spreads to other parts of the brain. Prior research by Rutecki [58] strongly suggests that, if spreading depressions are to exist, then only K^+ and Ca^{2+} ion concentrations change before such an event. Hence, even though the model developers are from the same group as Dronne *et al.*, fewer ionic concentrations are included in the Chapuisat model and the way in which these two ions are modelled differs. Both calcium and potassium ions, for instance, are described in the later model by diffusion-reaction equations. Moreover, the actions of the pumps, exchangers and channels, such a centrepiece of Dronne's 2006 model [55], are encapsulated in the reaction terms of these diffusion-reaction equations; gone are the multitude of equations found in Dronne *et al.* required to capture the actions of, say, the voltage-driven gates.

Another family of models was started by Aubert and Costalat [59], who were interested in the astrocyte-neuron lactate shuttle described in Section 2.1.2.7. To this end, their model includes the dynamics of lactate, glutamate and also sodium ions, as they are co-transported along with

glutamate into the astrocytes. This, in part, inspired the model by Cloutier *et al.,* [54], which tries to predict whether or not it is feasible that the lactate shuttle proposed by Pellerin and Magistretti [32] and described in Section 2.2.2.7, is a key feature in brain energy metabolism.

Although it is a large model - there are 34 independent variables across four compartments, with 63 parameters - the outputs that the authors concentrate on are the glucose, glycogen and lactate dynamics in the different compartments in order to test the feasibility of the lactate shuttle.

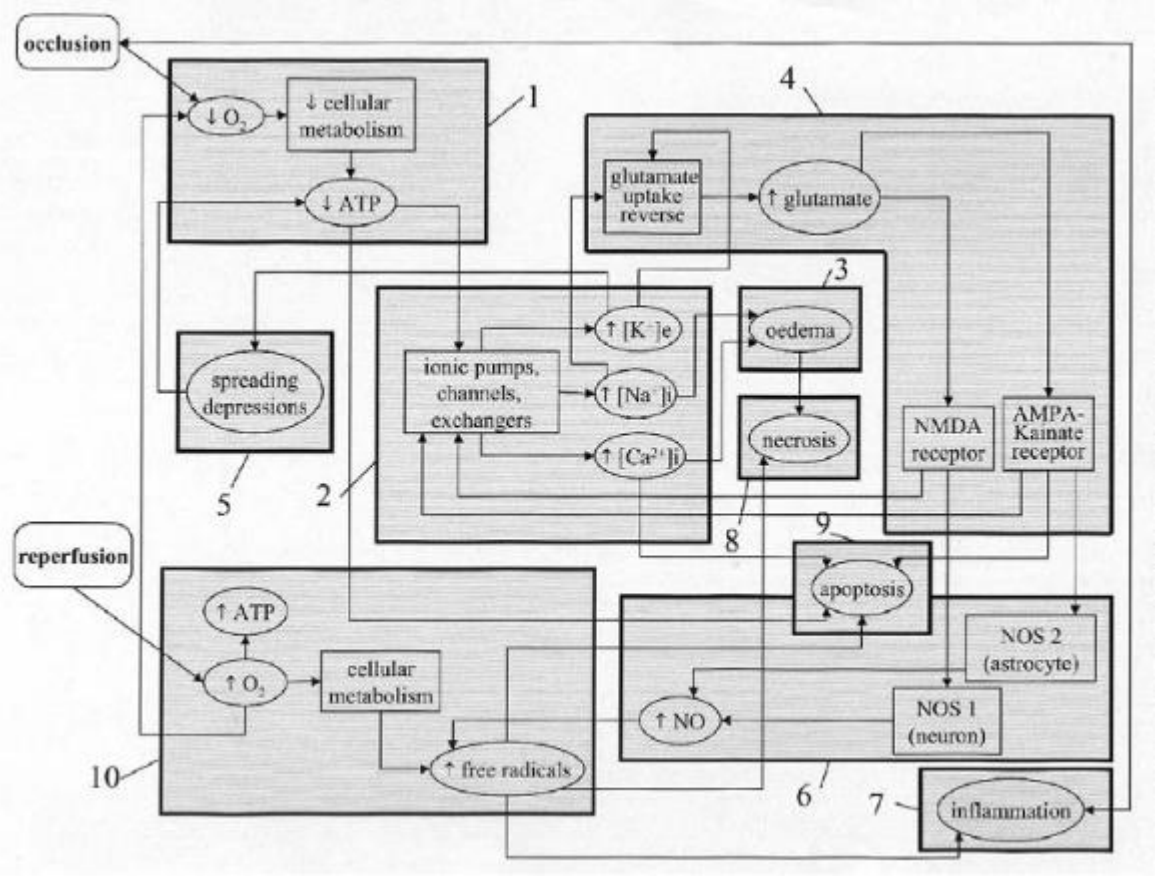

Figure 2.7: The ten different components of the Dronne model. Reproduced from Dronne *et al.,*[53].

The model proposed by Orlowski *et al.* [56] builds upon the Cloutier model in order to observe the effects of overproduction of H^+ ions and, hence, pH (the output) changes in brain cells during ischaemic stroke. In order to capture the pH dynamics, the model differs slightly from that of Cloutier, mainly in the following elements. First, the theorised glutamate loop from neurons to astrocytes, which Cloutier *et al.* sought to test, is absent. This is since pH (the focus of the Orlowski

model) and glutamate dynamics are deemed to be unrelated. Second, the model adds in seven ion channels and pumps that regulate pH dynamics. These pumps are situated between the extracellular

	Duval *et al.* [50]	**Dronne *et al.*** [53]	**Dronne *et al.*** [55]	**Chapuisat *et al.*** [52]	**Aubert and Costalat** [59]	**Cloutier et al.** [54]	**Orlowski et al.** [56]
Clinically Relevant Input	Yes	Yes	No	Yes	Yes	Yes	Yes
Includes Calcium Dynamics	No	Yes	Yes	Yes	No	No	Yes
Includes Dynamics of Other Ions	No	Yes (Na^+, K^+)	Yes (Na^+, K^+, Cl^-)	Yes (K^+)	No	No	Yes (Na^+, K^+, Cl^-)
Decision for Cell Fate	Yes	Yes	No	Yes	No	No	No
PDEs or Compartmental	Uses 'units', compartmental (matrix)	Uses 'units', compartmental	Uses 'units', compartmental	Uses 'units', compartmental	Compartmental ODEs	Compartmental ODEs	Compartmental ODEs

Table 2.2: Summary of selected models of ischaemic stroke

space and neuron/astrocyte membranes. The equations for modelling these channels and pumps come from Endresen *et al.* [60]. Third, a pH buffer is added to both the neuronal and astrocytic compartments.

Calcium ion dynamics are included in this model. One reason for their inclusion is because the level

of pH directly affects the calcium ion concentration [43], with apoptosis occurring at pH values under approximately 6.5. Another is that both calcium channels and the sodium-calcium pump help to regulate pH and, hence, are included in the pH buffer. The authors conclude that the pH decreases after blood flow is reduced, with the magnitude of the pH drops being controlled by two ATP-powered pumps and the rate at which glucose is used.

Since we take a particular interest in ion transport, it is worthwhile to consider the equations at the heart of some of the mathematical models examined here. These were proposed by Endresen *et al.*, [60], and were used for the ion dynamics of, for instance, the Orlowski model. Endresen's proposed equations for the calcium ion current, as it moves through the calcium channels on the cell membrane, are as follows:

$$i_{Ca} = k_{Ca} f d_{\infty} \sinh\left(\frac{e(v-v_{Ca})}{kT}\right) \quad (2.1)$$

$$d_{\infty} = \frac{1}{2}\left(1 + \tanh\left(\frac{2e(v-v_d)}{kT}\right)\right) \quad (2.2)$$

$$\frac{df}{dt} = \frac{1}{\tau_{Ca}} \cosh\left(\frac{2e(v-v_f)}{kT}\right)\left(\frac{1}{2}\left(1 - \tanh\left(\frac{2e(v-v_f)}{kT}\right)\right) - f\right) \quad (2.3)$$

where:

i_{Ca} is the variable representing the current due to calcium ions,

k_{Ca} is an observed constant representing the conductance of the calcium channels,

f is a variable signifying the proportion of open calcium channels. This is a function of both v and f itself.

d_{∞}, a variable, is the proportion of calcium channels open at steady-state,

v is a variable representing the intracellular voltage (with respect to the extracellular potential). It is, itself, dependent on the currents caused by ions such as potassium, sodium and calcium.

v_{ca} is an observed constant that represents the equilibrium potential for calcium (the potential at which net calcium movement into the cell is zero)

k is the Boltzmann's constant

T is an observed constant for intracellular temperature (a constant)

τ_{Ca} represents the relaxation time for calcium channels (a constant)

v_d and v_f are constants representing the half-activation and half-inactivation potentials of the calcium channels.

If we look back at all these mathematical models, we find that which ions are included in these models, therefore, depends on what processes or phenomena the authors attempt to capture and which previous models they used as a backbone for their own.

2.3.2 Apoptosis Models involving Caspases

The first subdivision of cellular models involves those that describe the caspase cascade (Section 2.1.4.1). Many of these may not necessarily focus on ischaemic stroke but, as we have seen from the literature, they are applicable in this field, as the mechanisms are similar.

A feature common to most of these models is that, rather than the output variable being the cell state, it is most often the concentration of caspase 3, since this is the final caspase activated during the cascade (Section 2.1.4.1). The steady-state caspase 3 concentration predicted by bistable models, which show three sets of equilibria separated by a pair of saddle-node bifurcations, can realistically belong to one of two sets of equilibria: the higher or the lower (the middle set is always unstable). Higher concentrations are indicative of cell death, whereas survival results for lower concentrations. For those earlier models that lack the possibility of bistable states, a simple threshold level of some variable, for instance the concentration of cytochrome c in the Fussenegger model, constitutes the simpler boundary between life and death of the cell [61].

Models capable of exhibiting bistability did eventually become popular; this was in response to work by, for instance, Nair *et al.* [62], who proposed that, under certain conditions, it was possible to observe two states: one favouring cell death and the other survival. Starting with Eissing's [51], these models investigate the causes of bistability, which may reveal how one may start or stop the apoptosis process.

Such mathematical models allowed researchers to support existing theories on how bistability might occur. Eissing *et al.,* for instance, lean towards the idea that apoptosis-inhibiting factors, such

as IAPs (*Inhibitor of apoptosis proteins*), compete with the effects of the caspases [51]. Bagci *et al.* [63] favour the explanation that cooperativity in forming the apoptosome complex, where the order of reaction in forming the apoptosome is larger than 1; that is, more than 1 molecule of cytochrome c is involved in activating 1 molecule of caspase 3.

2.3.3 Cell Damage/Death Models

The mathematical models discussed in Section 2.3.2 present detailed simulations of events occurring during apoptosis. There are many other ways for a cell to die, however, and these are linked to how and to what extent the cell is damaged (see Section 2.1.4). However, just as the apoptosis models did not present any link between Caspase 3 (or other molecules) and cell death, (aside from either, rather crudely, setting a threshold or requiring the concentration of the executioner caspases to lie on the set of larger-valued stable nodes), so too is there a lack of connection among models in the literature between cell damage and death.

One counterexample, however, is the mathematical model developed by Chapuisat *et al.*[52], whose major point of difference from previous models is that theirs differentiates between apoptosis and necrosis, depending on the damage incurred by the cell by calcium influx (see Section 2.1.4, which elaborates on the importance of calcium ions and their role in cell death). In particular, apoptosis is assumed to be a two-stage process, with the first stage being a reversible stage and the second being an irreversible one. The reversible stage is triggered when the variable representing cell fate, θ, decreases below a threshold value, θ_{apop}.

Chapuisat's modelling approach can be compared with DeGracia's [7], who also models cell damage after ischaemia. Whereas in the DeGracia model, the rate at which these cells deteriorate towards or away from apoptosis is determined solely by the difference between the Repair and Damage functions (which is similar to θ), here it is determined by a 'race' between two functions: the apoptosis function, A, and θ. The apoptosis function is a Hill function dependent on the energy of the cell (DeGracia's model, on the other hand, does not account for the cell's energy). If there is sufficient energy for A to reach an apoptosis threshold, A_{apop}, before θ falls below θ_{nec}, where

$\theta_{nec} < \theta_{apop}$, then the cell dies by apoptosis. However, if θ reaches θ_{nec} first, which occurs if there is insufficient energy for apoptosis, then the cell dies by necrosis. In the reversible state, θ can still rise above θ_{apop} if the Damage to the cell is sufficiently small.

The output variable, θ, is defined as a function of Repair, R, and Damage, D, linking cell damage to their demise:

$$\frac{\partial \theta}{\partial t} = R(1-\theta) - D \quad (2.4)$$

Just as in the DeGracia model, there are two competing functions in equation 2.4: R, which determines the rate at which the cell repairs itself (i.e. the 'Stress' function in DeGracia's model), named the Repair function, and the other, D, determining the rate at which the cell succumbs to damage by calcium ions (i.e. the 'Damage' function in DeGracia's model), which is also named the Damage function. The Damage functions of both models are very similar; they are both Hill functions whose independent variables are the injury magnitude (DeGracia's Damage function) and calcium concentration (Chapuisat's Damage function). The major difference comes from the biology; whereas DeGracia's model does not state what factors cause the injury, Chapuisat's assumes that injury stems only from calcium concentration.

However, Chapuisat's Repair function differs from DeGracia's corresponding Stress function; instead of a Hill function depending on the injury magnitude, as in DeGracia's model, Chapuisat's Repair function is dependent only on the energy available to the cell. The rationale is that, with more energy, the cell is able to protect itself from the incoming calcium flux. The rate of cell death is determined by subtracting the rate at which the Repair function can 'fix' the cell from the Damage (Equation 2.4). The Chapuisat model, therefore, is unique in that it firmly draws a line between apoptosis and necrosis and links damage and repair of the cell by calcium ions to cell death.

The problem with models that specialise in one form of cell death – and even a model that firmly differentiates between apoptosis and necrosis, like Chapuisat's - is that they do not focus on the bigger picture. Not all dead cells necessarily suffer the same fate and current hypotheses blur the

line between apoptosis and necrosis in many cases of cell death. Hence, by modelling one process when, in fact, the other process (or, indeed, necroptosis or even one of the other forms of cell death) occurs, we can introduce assumptions that have no concrete foundations into the model.

Since such complexity in biology is either beyond elucidation or would result in over-complicated mathematical models, DeGracia *et al.* attempt to absorb the many modes of cell death into the elegance of a simple model. This is one which we study in-depth here, as it proves useful for our model later (Chapter 4). The model consists of just two variables - Damage (D) and Stress (S) - represented by two coupled ordinary differential equations (ODEs).

Figure 2.7 shows the model schematic: it takes, as input, an injury magnitude of the stroke (I) which ranges from 0 to 10, depending on how severe the ischaemia is. The output is the time-course for both D and S, which we explain below.

After ischaemic stroke, all biological phenomena that contribute towards damaging the cell, such as depletion of ATP and damage by oxidative agents, are lumped into the Damage variable (D), while all phenomena that attempt to bring the cell back to its healthy state are lumped into the Stress variable (S). This is shown in Figure 2.8.

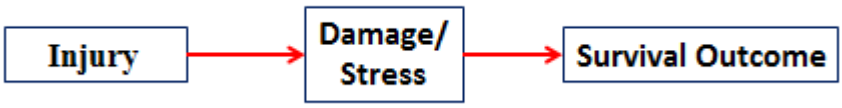

Figure 2.8: Schematic showing the input, output and variables of the DeGracia Model.

S and D are locked in competition with each other; if S is larger than D, then the cell's Stress factors overcome the Damage done to it; the cell survives ischaemia. If, however, D is larger, then the Damage factors prevail and the cell dies. Hence, without being too concerned about the specific biological details that go into each variable, the model predicts whether the cell will heal itself or succumb to death, given an initial injury value.

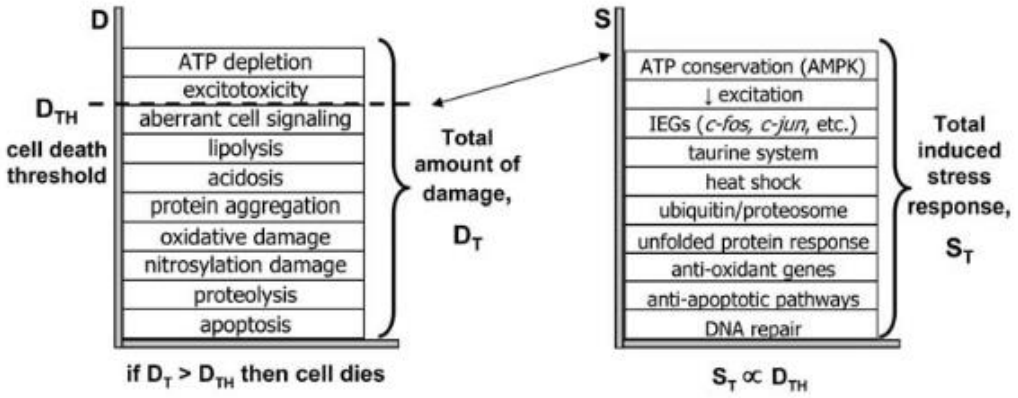

Figure 2.9: Schematic showing the various processes that are involved in the Damage (D) and Stress (S) variables in DeGracia's model. Reproduced from DeGracia *et al.*[7].

This input is an addition to the model by Huang *et al.* [64], where the authors model two competing molecular proteins (GATA1 and PU.1) in place of the two competing variables, D and S, in the DeGracia model. No input was required in Huang's model; only the initial conditions representing the concentrations of the two proteins had to be stated. However, D and S are both affected by input I, as we now discuss.

DeGracia's model has the form:

$$\frac{dD}{dt} = \frac{[f(I)]^4}{[f(I)]^4+S^4} - D \quad (2.5)$$

$$\frac{dS}{dt} = \frac{[g(I)]^4}{[g(I)]^4+D^4} - S \quad (2.6)$$

where $f(I)$ and $g(I)$ are functions depending on the Injury magnitude, I. $f(I)$ is equivalent to the amount of Stress (S) required to halve the accumulation of D from its maximum value, while $g(I)$ is equivalent to the Damage (D) required to halve S from its maximum.

If we focus on equations 2.5 and 2.6, then we see that each ODE consists of two terms: a positive accumulation and a negative decay term. The accumulation term is in the form of a Hill function. We can see why DeGracia *et al.* describe D and S as being *mutually antagonistic*: there is an inversely but exponentially proportional relationship between the rate of accumulation of D and the amount of S (and vice versa). This makes sense biologically, as having more Stress factors would inhibit the

production of Damage factors and vice versa.

The functions $f(I)$ and $g(I)$ are both exponential functions. When I increases, D is assumed to become exponentially larger, while S will increase for small increases of I, but decreases as the injury becomes too large, as the stress factors become overwhelmed. Hence, DeGracia *et al.* proposed that the functions should be as follows:

$$f(I) = c_D I e^{\lambda_D I} \quad (2.7)$$

$$g(I) = c_S I e^{-\lambda_S I} \quad (2.8)$$

where c_D, c_S, λ_D and λ_S are constants.

The second term of Equation 2.5 and 2.6 represent, respectively, the natural decay of D and S. The decay terms of D and S are uncoupled from each other (while D and S may inhibit each other's *formation,* one does not eliminate the other). The rate of decay is also unrelated to the injury magnitude; hence, there is no dependence on I.

The authors observe that there are four different 'injury courses', dependent on the parameter values. An injury course is a diagram showing how the Damage variable changes as the input injury value is varied. Of these four injury courses, three display bistability, a hysteretic feature whereby increasing or decreasing the injury value continuously leads to a discontinuous drop or rise in the Damage variable and vice versa. This bistability is often seen in biological systems [65], and so is an indicator that the parameter values of the model may be in the right range.

It should be noted that the injury magnitude, I, is not a function of time in the DeGracia model: in practice, the magnitude of injury in any cell will change due to changing stimuli, such as fluctuating calcium concentrations. It is also very difficult to quantify I in a clinical setting and, hence, the model should be coupled with another which takes a more quantifiable input.

2.3.4 Modelling calcium oscillations in the astrocytes

When it was discovered that astrocytes are not mere 'place-holders' but cells that can influence activities in the neurons through their intracellular calcium ion concentration, the mathematical modelling community became interested in replicating the spontaneous oscillatory behaviour of these ions that was observed in experiments. To this end, several have proposed their own models, which we divide into two groups: those investigating single cells and others that combine many cells. The former are spatially homogenous ODE models, while the latter require PDEs.

2.3.4.1 Single Cell Models

Single cell models, [66], [67] , focus on the transport of calcium into and out of the cell. The key variables in these models are the intracellular calcium concentration, of course, as well as its concentration in the Endoplasmic Reticulum (ER), where calcium ions are stored and inositol triphosphate (IP_3). The external calcium concentration, being several orders of magnitude larger at rest, is usually assumed constant.

Calcium diffuses into the cell down its concentration gradient and can also be transported inside through the CICR mechanism (Section 2.1.3.2), aided by IP_3, and out into the extracellular space or back into the ER/SR via pumps and through SERCA (Section 2.1.3.3).

Many terms in the equations of these models are highly nonlinear, reflecting the interdependencies of these processes. For instance, the CICR mechanism may be represented as a process proportional to the difference in concentration between intracellular and extracellular concentrations [66]. Lavrentovich and Hemkin also assume that the term is IP_3 dependent:

$$v_{CICR} = 4v_{M3}\left(\frac{k_{CaA}^{n}X^{n}}{(X^{n}+k_{CaA}^{n})(X^{n}+k_{CaI}^{n})}\right)\left(\frac{Z^{m}}{Z^{m}+k_{ip3}^{m}}\right)(Y-X) \quad (2.9)$$

Here, v_{CICR} represents the release of calcium ions from the ER/SR into the cell during CICR, X and Y are the intracellular and extracellular calcium concentrations, respectively and Z is the intracellular concentration of IP_3. The other symbols are all parameters with fixed values.

Hill functions, such as those used here, are found in other mechanisms and portray how chemicals (in this case, IP_3) act as a tuning mechanism, amplifying the effects of the mechanism (here CICR) when found in high concentration but masking them at lower quantities.

Although these models principally investigate the causes and effects of calcium oscillations, the equations proposed for mechanisms such as CICR and SERCA are of importance later when we propose our own model (see Section 3.2).

2.3.4.2 Spatially Varying Models

Whereas single cell models focus on one cell, or else assume the environment to be well-mixed, spatially varying models of calcium oscillations in astrocytes have at least one diffusion-reaction equation: the model thus consists of coupled PDEs and ODEs. Examples of spatially varying models include those developed by Li *et al*. [68] and Yang [69].

Coupled diffusion-reaction equations, under certain conditions (see Section 2.3), can display *Turing instabilities*. These occur when the system of equations is stable in the absence of diffusion (that is, the reaction terms alone are linearly stable) but adding the diffusion terms causes instabilities to appear, given appropriate parameter values. These instabilities manifest themselves as patterns: the spots of a leopard and stripes of a zebra, for instance, can be modelled by reaction-diffusion equations [70]. Calcium ions are also known to show patterns during their oscillations [69], [71] and so one requirement of model development and parameter estimation should be that the resulting dynamics must be stable in the absence of diffusion but unstable in its presence. Such patterns can be seen in Figure 2.9, taken from the work of Yang [69]. We discuss Turing patterns in greater detail in Section 2.4, as these are an important aspect of our work.

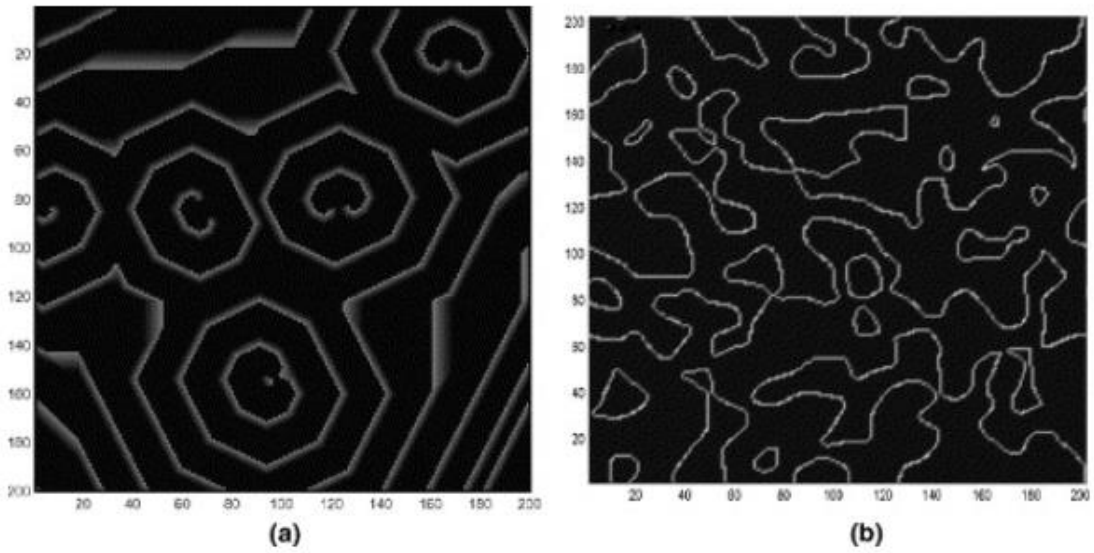

Figure 2.10: Reproduced from Yang [69]. Two cases that satisfy the conditions for Turing instability produce patterns – spirals on the left and rings on the right.

2.4 Reaction Diffusion Equations in Literature

In 1952, Alan Turing published his seminal paper on instabilities arising from certain reaction-diffusion systems [72]. In particular, Turing found that his patterns could only arise when the system's reaction terms were linearly stable in the absence of diffusion but became unstable in its presence. This is counterintuitive; diffusion is a 'stabilising' process in that, alone, it removes spatial variations and yet, when coupled to an already stable system, instabilities occur. To illustrate the relevance of his work, Turing gave an example from biology: each variable in the set of reaction-diffusion equations represented a *morphogen,* a chemical driving the development of an embryo. In cells arranged in a ring structure, if one morphogen is a growth factor [72], [73], instabilities corresponding to, for instance, the limbs of animals, may form.

Maini claims that Turing's discovery made him one of the first systems biologists [73]. Although experimentalists have yet to replicate his predictions in a biological context (in the sphere of chemistry, however, morphogens have been discovered, as have diffusion-driven instabilities [73]) biologists can no longer simply "identify the individual components" of a system [73]. Even if it turns out that no set of chemical species impacts morphogenesis, Turing's mathematical analysis gives insight into not necessarily *what* but, rather, *how* to look for factors influencing morphogenesis (or

other symmetry-breaking phenomena).

Turing's work is of substantial importance to us because our model consists of coupled diffusion-reaction equations which must also show spatial inhomogeneities, as a stroke results in three different regions (the core, penumbra and unaffected region). Hence, rather than using different parameters to represent each region, if our model can display Turing patterns, then we may be able to predict how each variable should interact with each other as well as find appropriate parameter ranges. The following sections discuss some of the mathematical detail behind these instabilities: the conditions required for pattern formation are given in Section 2.4.1 and we also review some models in the literature that are known to show these patterns in 2.4.2.

2.4.1 Conditions Required for Occurrence of Turing Instabilities

In this subsection, we derive the conditions required to observe Turing instabilities. Particular focus is placed on the case where the system has two dependent variables, since this will be useful for our work in Chapter 5.

By definition, Turing instabilities occur in reaction-diffusion systems where the reaction terms alone are linearly stable to small perturbations around the equilibrium, but where introducing diffusion terms renders the system unstable. First, consider the generalised reaction-diffusion system:

$$\frac{\partial Y_j}{\partial t} = D_j \nabla^2 Y_j + F_j(\boldsymbol{Y}) \quad (2.10)$$

where Y_j is the *j*th element in the vector $\boldsymbol{Y} = (Y_1, Y_2, \dots, Y_n)^T$, which consists of *n* dependent variables, D_j the *j*th diffusion coefficient, and F_j the *j*th reaction equation. We take the domain of the problem to be a 1-dimensional line in Cartesian coordinates, from $x = 0$ to $x = L$.

We are interested in the behaviour of the linearised system, since we wish to investigate stability close to the equilibrium. The linearised model is (neglecting higher order terms):

$$\frac{\partial Y_j}{\partial t} = D_j \nabla^2 Y_j + \frac{\partial F_j}{\partial Y_1}\Big|_{eq} Y_1 + \cdots + \frac{\partial F_j}{\partial Y_n}\Big|_{eq} Y_n \quad (2.11)$$

where eq stands for the equilibrium point, which we take to be at $(0,0, \dots, 0)^T$.

First, we introduce a trial solution: $Y = (Y_1, Y_2, \dots, Y_n)^T$, where:

$$\begin{pmatrix} Y_1 \\ Y_2 \\ \vdots \\ Y_n \end{pmatrix} = \begin{pmatrix} y_1 \\ y_2 \\ \vdots \\ y_n \end{pmatrix} \exp(\lambda t + ikx) \quad (2.12)$$

By substitution of the trial solution (2.12) into the linearised system (2.11), we obtain an equation of the form:

$$\begin{pmatrix} \lambda + D_1 k^2 - \frac{\partial F_1}{\partial Y_1} & \cdots & -\frac{\partial F_1}{\partial Y_n} \\ \vdots & \ddots & \vdots \\ -\frac{\partial F_n}{\partial Y_1} & \cdots & \lambda + D_n k^2 - \frac{\partial F_n}{\partial Y_n} \end{pmatrix} \begin{pmatrix} y_1 \\ y_2 \\ \vdots \\ y_n \end{pmatrix} = \begin{pmatrix} 0 \\ 0 \\ \vdots \\ 0 \end{pmatrix} \quad (2.13)$$

In order for non-trivial solutions to exist, the determinant of the matrix on the LHS of equation (2.13) must equal zero. We can then find the eigenvalues, λ, as a function of the wavenumber, k.

$$\lambda = \lambda(k) \quad (2.14)$$

Instabilities occur when the following conditions are satisfied:

1. **First Condition (General Model):**

   When $k = 0$, all eigenvalues λ of the determinant:

   $$det = \begin{vmatrix} \lambda - \frac{\partial F_1}{\partial Y_1} & \cdots & -\frac{\partial F_1}{\partial Y_n} \\ \vdots & \ddots & \vdots \\ -\frac{\partial F_n}{\partial Y_1} & \cdots & \lambda - \frac{\partial F_n}{\partial Y_n} \end{vmatrix} \quad (2.15)$$

   have negative real part.

2. **Second Condition (General Model):**

   When $k \neq 0$, at least one eigenvalue λ of the equation

   $$\begin{vmatrix} \lambda + D_1 k^2 - \frac{\partial F_1}{\partial Y_1} & \cdots & -\frac{\partial F_1}{\partial Y_n} \\ \vdots & \ddots & \vdots \\ -\frac{\partial F_n}{\partial Y_1} & \cdots & \lambda + D_n k^2 - \frac{\partial F_n}{\partial Y_n} \end{vmatrix} = 0 \quad (2.16)$$

   has positive real part.

The first condition corresponds to system stability in the absence of diffusion, the second to instability in the presence of diffusion. Reaction-diffusion systems with boundary conditions must meet one more criterion for pattern formation: by bounding the domain, the number of patterns that can fit inside is restricted to whole number values. The wavelengths corresponding to each allowed pattern must also satisfy the conditions above. We will illustrate this by taking the particular case of a reaction-diffusion model with two species.

2.4.2 Pattern Formation in Two-Species Reaction-Diffusion Models

The generalised coupled reaction-diffusion PDE model with two dependent variables can be written as:

$$\frac{\partial u}{\partial t} = D_1 \frac{\partial^2 u}{\partial x^2} + f(u, v) \quad (2.17)$$

$$\frac{\partial v}{\partial t} = D_2 \frac{\partial^2 v}{\partial x^2} + g(u, v) \quad (2.18)$$

with no-flux boundary conditions (this leads to sinusoidal solutions):

$$\frac{\partial u}{\partial x}(x = 0) = \frac{\partial u}{\partial x}(x = L) = 0 \quad (2.19)$$

We are interested in the behaviour of the linearised system, since we wish to investigate stability close to the equilibrium. The linearised model is (neglecting higher order terms):

$$\frac{\partial u}{\partial t} = D_1 \frac{\partial^2 u}{\partial x^2} + f_u|_{eq} u + f_v|_{eq}\, v \quad (2.20)$$

$$\frac{\partial v}{\partial t} = D_2 \frac{\partial^2 v}{\partial x^2} + g_u|_{eq} u + g_v|_{eq} v \quad (2.21)$$

where f_u is the shorthand notation for the partial derivative, $\frac{\partial f}{\partial u}$, and eq stands for the equilibrium point (we henceforth drop this notation and assume it to be understood).

We introduce the trial solution:

$$\binom{u}{v} = \binom{U}{V} \exp(\lambda t + ikx\,) \text{ (2.22)}$$

Substitution of equation 2.22 into equations 2.20 and 2.21 results in the following:

$$\begin{pmatrix} \lambda + D_1 k^2 - f_u & -f_v \\ -g_u & \lambda + D_2 v^2 - g_v \end{pmatrix} \binom{U}{V} = 0 \text{ (2.23)}$$

The determinant of the matrix must be zero for non-trivial solutions to exist:

$$\begin{vmatrix} \lambda + D_1 k^2 - f_u & -f_v \\ -g_u & \lambda + D_2 k^2 - g_v \end{vmatrix} = 0 \text{ (2.24)}$$

This gives an equation for λ in terms of k^2: $\lambda = \lambda(k^2)$. Such an equation is called the *dispersion relationship.*

Specifically, here the dispersion equation is:

$$(\lambda + D_1 k^2 - f_u)(\lambda + D_2 k^2 - g_v) - f_v g_u = 0 \text{ (2.25)}$$

This gives a quadratic equation in λ:

$$\lambda^2 + A\lambda + B = 0 \text{ (2.26)}$$

where $A = (D_1 + D_2)k^2 - g_v - f_u$ (2.27)

and $B = D_1 D_2 k^4 - (D_1 g_v + D_2 f_u)k^2 + f_u g_v - f_v g_u$ (2.28)

Remembering that we have to satisfy conditions (2.15) and (2.16) of the General Model, as described in Section 2.3.1, we find that (2.15) leads to the following two conditions for the two-species case:

1. $f_u + g_v < 0$ (2.29)

2. $f_u g_v - f_v g_u > 0$ (2.30)

Condition (2.16), meanwhile leads to these conditions for the two-species case:

3. $D_1 f_u + D_2 g_v > 0$ (2.31)
4. $(D_1 f_u - D_2 g_v)^2 + 4 D_1 D_2 f_v g_u > 0$ (2.32)

Note that this imposes conditions on both the ratio between the diffusion coefficients, D_1 and D_2, as well as the reaction terms.

Finally, we must address the conditions imposed upon us by the boundary conditions. In the case of no-flux boundary conditions, the solutions will be a sum of cosines, of the form: $u \sim \exp(\lambda t)\cos(kx) = \exp(\lambda t)\cos\left(\frac{n\pi}{L}x\right)$ (2.33)

Here, L is a typical lengthscale (for example, when modelling the human brain, we might choose L to be 20cm), while n is a natural number known as the *mode,* and quantifies the number of patterns seen within the domain. Therefore, the solution must be a summation of cosine functions in space to satisfy the boundary conditions and the modes be natural numbers so that the cosine waves can 'pack' themselves into the domain. In particular, the admissible wavenumbers are: $k = \frac{n\pi}{L}$, for natural numbers n.

The solution, moreover, typically consists of both spatially stable and unstable modes. The onset of spatial instabilities occurs when $\lambda = 0$. From the quadratic equation (2.26), we notice that when $\lambda = 0$, then $B = 0$. Hence, setting equation (2.28) to zero and solving for k^2 gives the wavenumbers at which instabilities arise, if any exist. In the ideal case, there should be two critical wavenumbers, k_+ and k_-. These correspond to, respectively, the larger and smaller real-numbered solutions to equation (2.28). Turing instabilities may exist if *any* admissible modes of the solution have corresponding wavenumbers such that:

$k_-^2 < k_{solution}^2 < k_+^2$ (2.34)

Figure 2.10 shows a typical dispersion plot of the maximum $Re(\lambda)$ against k^2, which one can obtain by solving equations (2.26-2.28) for the real part of λ with respect to k. This dispersion plot is the

work of Nesterenko *et al.* [74]. Graphically, we can see that there are two cases where Turing instabilities cannot form due to the inability to satisfy this criterion. One situation arises when there are no positive roots, λ, satisfying $B = 0$, (turquoise plot in Figure 2.10) while the other (red plot) occurs if λ is already positive at $k = 0$; in other words, the reaction terms alone are unstable. Note that the solid red curve represents the real part of the eigenvalues, while the dashed curve represents the imaginary part.

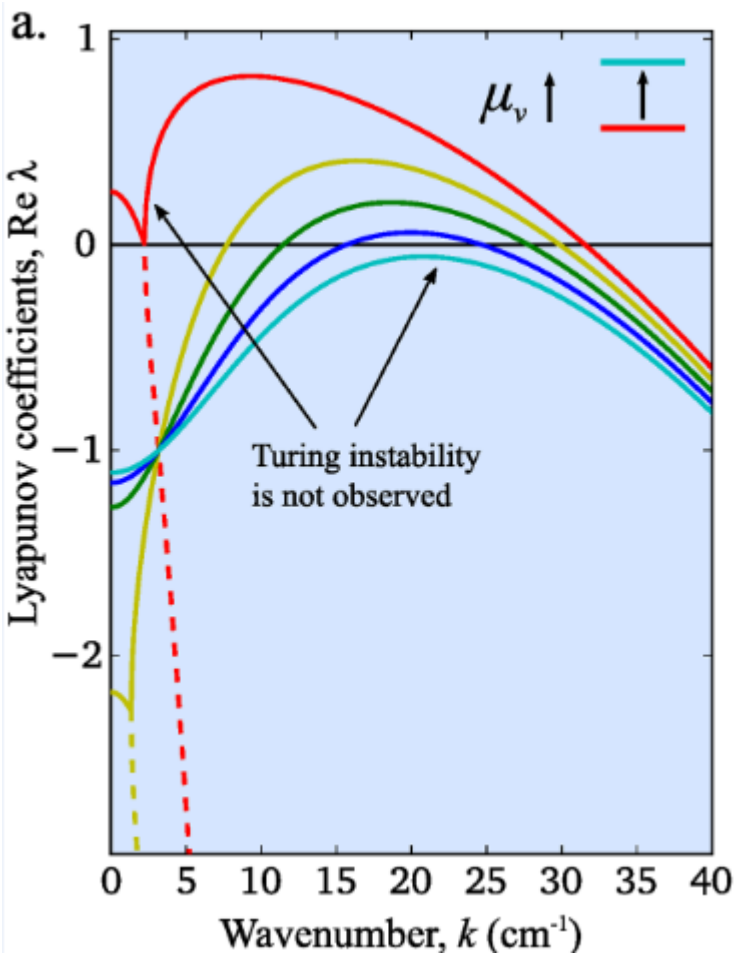

Figure 2.11: Plot showing typical dispersion relations (wavenumber compared with the real value of the system eigenvalues) of a reaction-diffusion system, where some parameter (μ_v) is varied. Whereas the yellow, green and dark blue plots show regions in which instabilities may occur, the red and turquoise plots show that no instabilities can be formed for these parameter values. Specifically, the red plot shows that the reaction terms alone have positive eigenvalues, whereas the turquoise shows that no wavenumber has positive solutions. Reproduced from Nesterenko *et al.* [74].

Due to the fact that larger modes form patterns with smaller amplitude variations and also since having multiple admissible modes causes them to combine nonlinearly (as the reaction terms are nonlinear), we would like to isolate a single mode that is 'small enough' to produce 'large enough'

amplitude variations by selecting parameters for A and B such that $k^2 = \frac{n^2\pi^2}{L^2}$ falls within k_+ and k_-. This process is known as 'mode isolation'.

Knowing the necessary mathematical conditions needed for Turing instabilities to occur, we can now proceed to the next subsection. There, we examine different reaction-diffusion models that researchers in the field commonly study and their corresponding Turing Space; the range of parameters for which patterns occur.

2.4.3 Common Diffusion-Reaction Models and their Turing Space

Turing's work on morphogenesis [72] inspired much work and in this section, we will look at three of these models: those of Thomas, Gierer-Meinhardt and Schnakenburg [75]–[77]. Many authors have studied the characteristics of these models or based their own on them [70], [74], [78]. In Chapter 5, we will base our own work on the properties common to models capable of showing Turing instabilities.

2.4.3.1 Thomas Model

The Thomas Model [75] is given by the following equations:

$$\frac{\partial u}{\partial t} = \nabla^2 u + a - u - \frac{\rho u v}{1+u+Ku^2} \quad (2.35)$$

$$\frac{\partial v}{\partial t} = D\nabla^2 v + \alpha(b - v) - u - \frac{\rho u v}{1+u+Ku^2} \quad (2.36)$$

The five parameters, a, α, b, K and ρ, together with a sufficiently large D, can render the system (2.35) and (2.36) unstable, a necessary condition for Turing instabilities. Figure 2.11, taken from Murray (56), shows the Turing space of the Thomas model for one specific set of parameters. We note that the bottom curve is the set of lower limits for values of a and b, while the curves labelled $D = 10, D = 100$ and $D \to \infty$ denote the upper limits of these parameters for each respective diffusion coefficient, D. The black dots signify that the values in between the lower and upper curves represent the model's Turing Space, for that value of D.

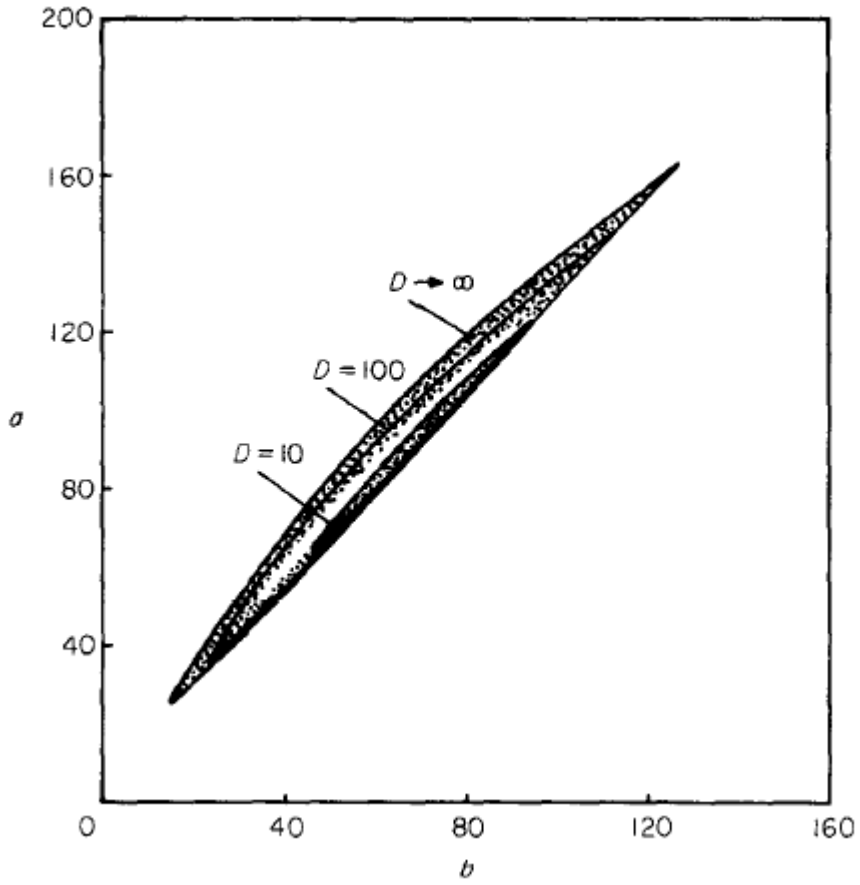

Figure 2.12: The Turing Space of the Thomas model for different values of D, with parameter values: $K = 0.125, \alpha = 1.5, \rho = 13$. Reproduced from Murray [78].

2.4.3.2 Gierer-Meinhardt Model

Another well-studied model known to exhibit Turing instabilities is the Gierer-Meinhardt [76], whose equations are written as:

$$\frac{\partial u}{\partial t} = \nabla^2 u + a - bu + \frac{u^2}{v(1+Ku^2)} \quad (2.37)$$

$$\frac{\partial v}{\partial t} = D\nabla^2 v + u^2 - v \quad (2.38)$$

The values of the parameters a, b and K as well as the ratio of diffusion coefficients, D, determine the stability of the system (2.37)-(2.38). Figure 2.12, taken from Murray [78], shows the Turing space, in terms of a, b and D for two values of K. We interpret this graph in a similar manner to that of the Thomas model above.

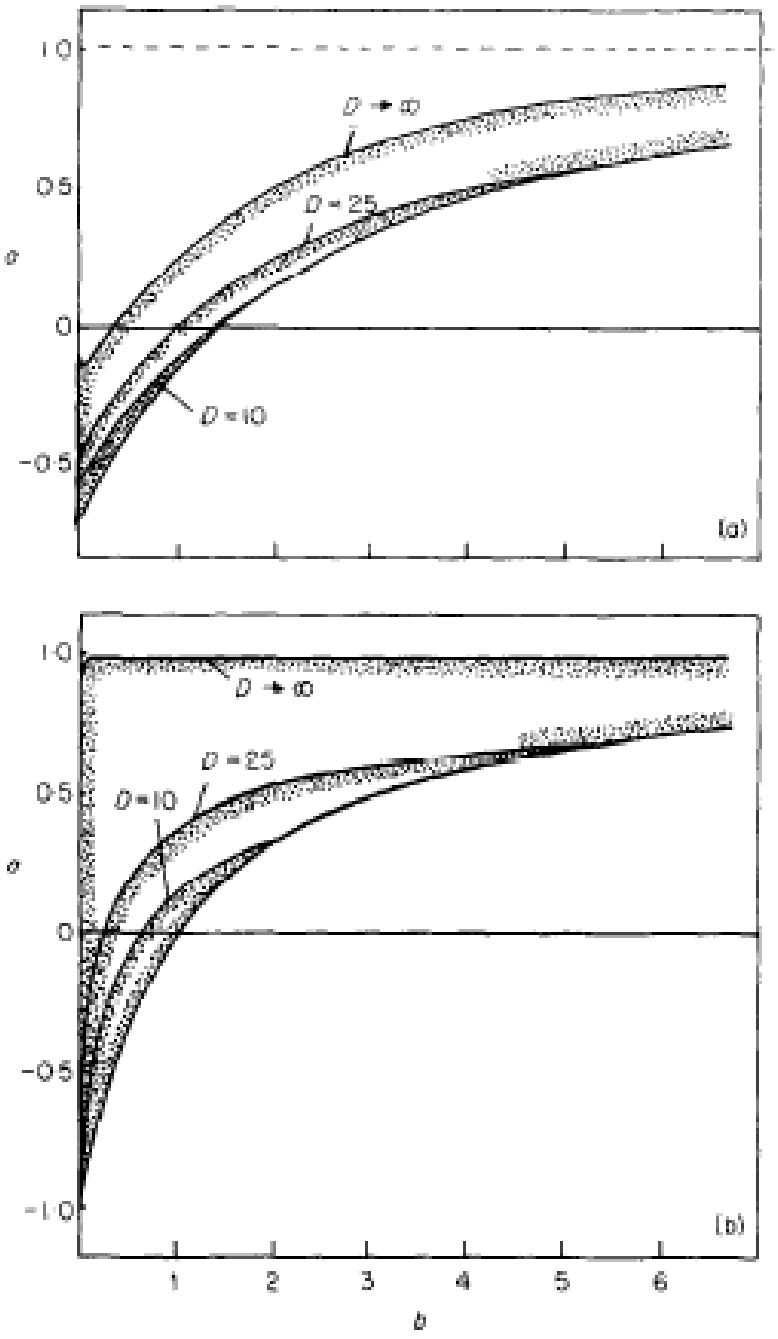

Figure 2.13: The Turing space of the Gierer-Meinhardt model as a function of diffusion ratios, D, for (above) $K = 0$ and (below) $K = 0.5$. Reproduced from Murray [78].

2.4.3.3 Schnakenburg Model

The Schnakenburg Model [77], in its simplest form, is written as the following:

$$\frac{\partial u}{\partial t} = \nabla^2 u + a - u + u^2 v \quad (2.39)$$

$$\frac{\partial v}{\partial t} = D\nabla^2 v + b - u^2 v \quad (2.40)$$

Since the only parameters are a, b and the diffusion coefficient D, Murray [78] simply plotted the Turing space, shown in Figure 2.13. We interpret this graph in a similar manner to that of the Thomas model above.

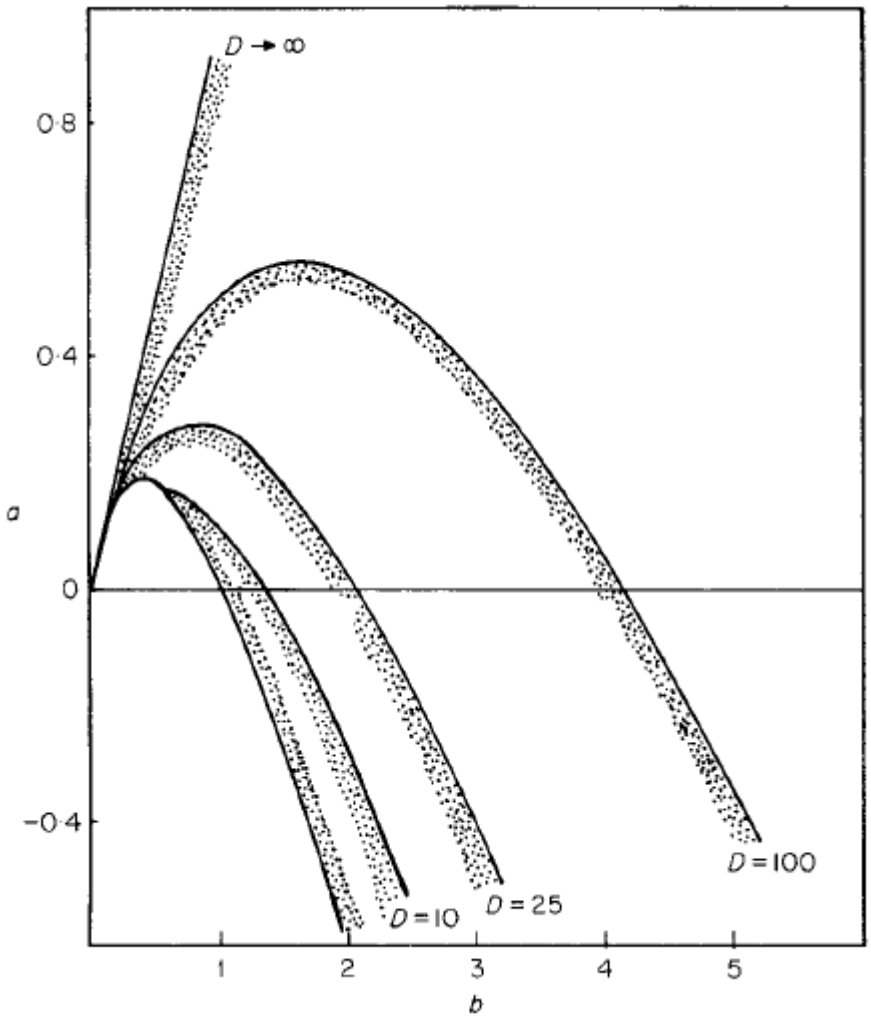

Figure 2.14: The Turing Space of the Schnakenburg Model for different diffusion coefficients, D. Reproduced from Murray [78].

2.4.3.4 Common Features of Models displaying Turing Patterns

The three models in section 2.4.3 have some features in common. Knowing these is important to understand what is required for Turing instabilities to occur both in a model and in a biological context.

Table 2.3 shows these common features. We can see that, first, at least 2 reaction-diffusion equations are required and that the reaction terms only become unstable because of the presence

of diffusion; this is the definition of Turing instabilities.

What is also noticeable is that a cooperative term must also be present in at least one of the equations. This is also a prerequisite for the fourth condition, which states that the signs of each element in the Jacobian of the reaction terms is either:

$$J = \begin{bmatrix} f_u & f_v \\ g_u & g_v \end{bmatrix}_{|eq} = \begin{bmatrix} + & - \\ + & - \end{bmatrix} \quad (2.41)$$

$$\text{or } J = \begin{bmatrix} + & + \\ - & - \end{bmatrix} \quad (2.42)$$

Finally, there must also be a sufficiently large diffusion coefficient, D, or ratio of diffusion coefficients if neither diffusion coefficient is unity. The larger the value of D, or, more strictly, the ratio between the two diffusion coefficients, the larger the Turing space.

Common Features of all Turing Models
At least two reaction-diffusion equations
Reaction terms alone are stable but become unstable in presence of diffusion
Cooperative term present
Signs of first derivative either $\begin{bmatrix} + & - \\ + & - \end{bmatrix}$ or $\begin{bmatrix} + & + \\ - & - \end{bmatrix}$ (2-species case)
Sufficiently large ratio of diffusion coefficient

Table 2.3: Features common to all models displaying Turing instabilities

In this subsection, we introduced the phenomenon of pattern formation, made famous by Alan Turing's predictions on morphogens in the 1950s. We saw that the presence of the 'stabilising' process of diffusion could, in fact, destabilise an otherwise stable system. Turing patterns resulted from these instabilities and we stated the conditions required for these to occur, both in general and

in the particular case of two-species models. We also discussed dispersion relations, which are important in the case where the system is constrained by boundary conditions and examined the relevant conditions this imposed on the two-species case. Finally, we looked into different diffusion-reaction models already studied and available in the literature and discussed their Turing Space. This analysis will be of importance in Chapter 5, where we investigate the formation of Turing patterns in our own model on ischaemic stroke.

2.5 Discussion and Conclusions

This chapter has examined a few of the many mathematical models in the literature. We have selected these particular models because they are the key models in the literature also since they form the backbone of our own model; by selecting the features from each model that we are interested in, we build up our own model.

Several models already exist in the literature and we discussed their strengths and drawbacks briefly in this chapter. For example, one of the first mathematical model of stroke, created by Duval *et al.* [50], includes both Cerebral Blood Flow (CBF) as input and cell survival outcome as output. However, it lacks both the calcium dynamics and subsequent damage inflicted; Dronne *et al.* [53], [55] build upon this model to include ion transport dynamics; however, modelling intra- and extracellular concentrations of four ion concentration dynamics (sodium, potassium, chloride as well as calcium), makes their model too complex in terms of the large number of parameters required.

In particular, we examined models of apoptosis. These models link inputs such as calcium ion concentrations to the concentrations of caspases triggered by the caspases cascade (see Section 2.2.4.1); the output is the concentration of Caspase 3, the final caspase in the cascade. High concentrations of this caspase indicate apoptosis of the cell. In many apoptosis models, such as the models of Bagci *et al.* and Eissing *et al.* [51], [63], bistability is an included feature: by varying the concentration of an input caspase, the Caspase 3 concentration can increase discontinuously from a

low, non-apoptotic concentration to a concentration high enough to induce apoptosis. This bistability is noted in experimental work [79], [80] and is required to prevent noisy signals from causing apoptosis.

However, since ischemic cells can die not only from apoptosis, but also from necrosis, (see Section 2.2.4) together with the fact that apoptosis can be triggered by both the intrinsic and extrinsic pathways (see Section 2.2.4.1), it may be too complicated a process to include both pathways of apoptosis and necrosis as well in a model. We have, therefore, neglected to mention these models in detail, preferring, instead, to lump all the processes causing death into a 'Damage counter'. These simplifications, as well as other assumptions of our new model, are detailed in the next chapter.

Chapter 3: Model of Calcium Transport

Yes, I will be thy priest, and build a fane

In some untrodden region of my mind,

Where branched thoughts, new grown with pleasant pain

Instead of pines shall murmur in the wind

'Ode to Psyche', John Keats

This chapter presents and analyses a mathematical model describing the mass transfer of calcium ions across the brain. In addition, calcium ions are normally kept at tightly regulated concentrations and this model includes the processes involved in calcium homeostasis. In Chapter 5, we couple this model of calcium transport to another describing cell injury and death (described in Chapter 4).

3.1 Model Equations

First, we examine a simple model where the brain is divided into three compartments: neurons, astrocytes and the extracellular space. An important assumption is that the blood plays no part in calcium transport, although it occupies a fixed fraction of the space. A schematic of the model is presented in Figure 3.1.

The model equations are as follows:

$$\varphi_a \frac{\partial C_a}{\partial t} = g_a - \gamma_{ae}(C_a - C_e) \quad (3.1)$$

$$\varphi_n \frac{\partial C_n}{\partial t} = g_n - \gamma_{ne}(C_n - C_e) \quad (3.2)$$

$$\varphi_e \left(\frac{\partial C_e}{\partial t} + U_e . \nabla(C_e)\right) = \nabla . \left(D . \nabla(\varphi_e C_e)\right) + \gamma_{ae}(C_a - C_e) + \gamma_{ne}(C_n - C_e) \quad (3.3)$$

where:

- C_a, C_n and C_e indicate the concentrations of calcium ions in the astrocytic, neuronal and extracellular compartments respectively.
- φ_a, φ_n and φ_e indicate the volume fraction of calcium in the respective compartments.
- γ_{ae} and γ_{ne} are the mass transfer coefficients of calcium ions to the extracellular space from the astrocytes and neurons, respectively.
- g_a and g_n are the generation terms for calcium in the respective compartments. There is assumed to be no calcium generation in the extracellular space.
- U_e represents the advection velocity of calcium transfer
- D represents the diffusion coefficient.

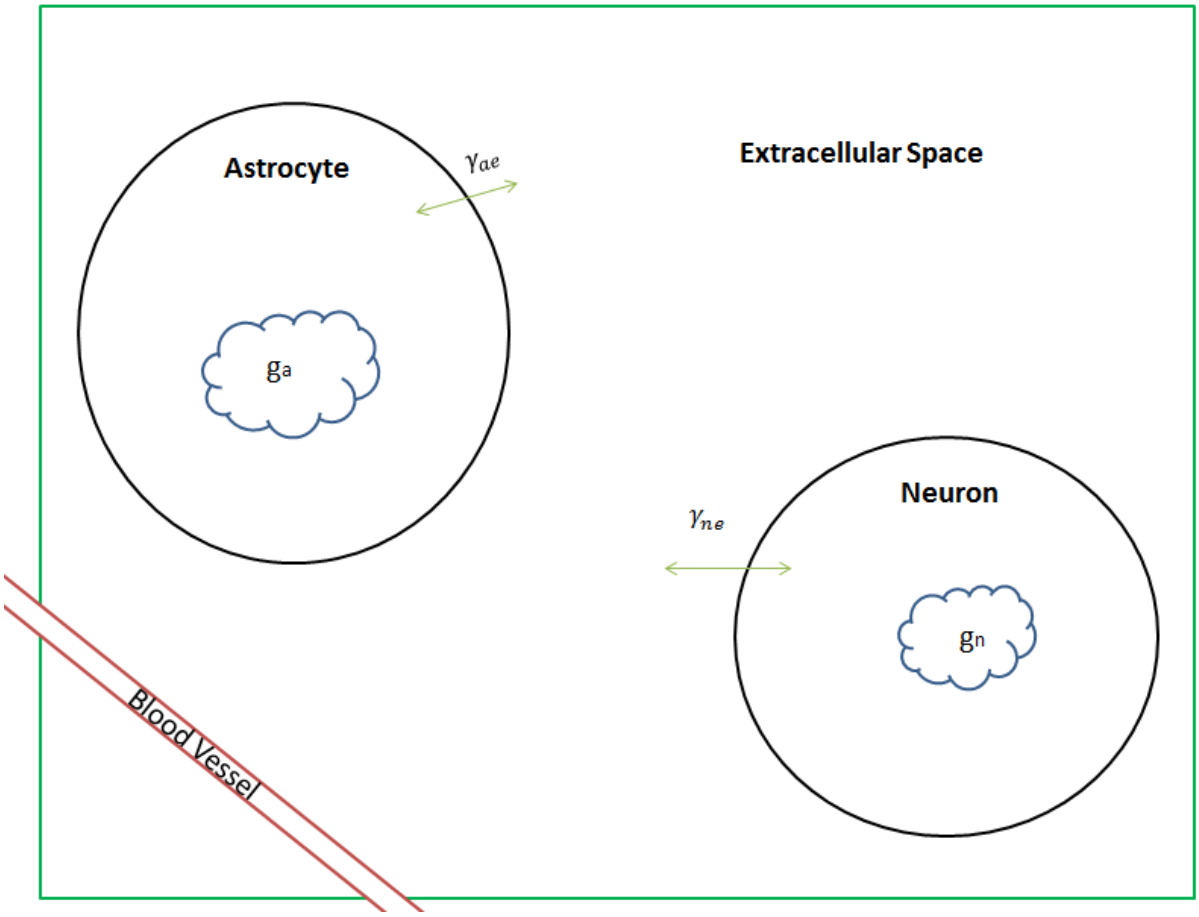

Figure 3.1: Schematic of the model, represented by equations (3.1)-(3.3).

Figure 3.1 is, of course, a simplified version of the physiology. The cell does not generate calcium ions, in reality, but has stores of calcium ions instead, as seen in Figure 3.2. We will discuss this

further in Section 3.4, where we present another, more complex, model. We also neglect to model other glial cells and assume that the extracellular space is homogeneous and so the diffusion coefficient is constant, whereas, in reality, the ions will encounter many obstacles in the extracellular space. The resultant diffusive route that they must then take is known as a tortuous path. This would make the diffusion coefficient a function of space. Finally, we focus our modelling only on calcium ions, knowing that it has a crucial role in cell death (see Section 2.2.4), neglecting all others for simplicity.

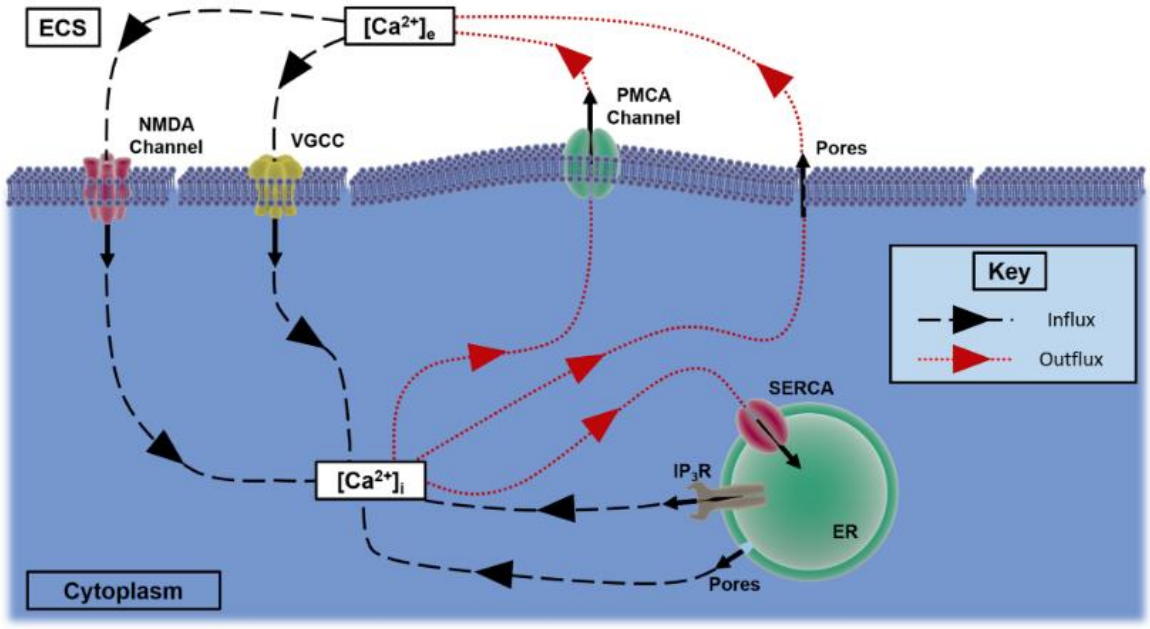

Figure 3.2: Schematic of calcium ion transport within the neuron – here, ECS is an abbreviation for the extracellular space. Similar transport occurs at the astrocytes. This figure was reproduced from Kant *et al.* [81].

These equations are the coupled mass transfer equations, where each equation represents the calcium dynamics in one of the three compartments. The final equation, describing transfer in the extracellular space, is an advection-diffusion-reaction equation, where the second term on the LHS represents the advection of calcium ions, while the first term on the RHS represents diffusion. Our goal is to find the values of the parameters in equations (3.1)-(3.3).

We first reduce the model to exclude all spatially-varying components, which we will then refer to

as our 0-dimensional model. The equation for the extracellular compartment, represented by equation (3.3), then becomes:

$$\varphi_e \frac{dC_e}{dt} = \gamma_{ae}(C_a - C_e) + \gamma_{ne}(C_n - C_e) \quad (3.4)$$

3.1 Calcium Ion Dynamics of the Orlowski Model

Since the calcium ion dynamics play such a key role in our work (see Chapter 2), we used CellML to run simulations of the Orlowski model [56], mentioned in Chapter 2.31, and observed the predicted calcium concentrations in the neurons, astrocytes and extracellular space when the CBF was reduced by: $70\%, 75\%, 80\%, 85\%, 90\%$ and 95% of its original value of 60 ml/100g/minute. The Orlowski model provides the link from CBF to calcium dynamics. The subsequent calcium dynamics in these three compartments are shown in Figures 3.2, 3.3 and 3.4 respectively. In all cases, CBF is reduced after 50 seconds.

Figure 3.2 shows that, for reductions in CBF greater than 70%, the neurons begin to uptake calcium ions a few minutes after the stroke. There is a sharp increase in calcium uptake that lasts a few minutes, before steady-state is reached. The steady-states range from 250-750 nM, depending on the CBF reduction (c.f. the physiologically observed values of 300nM-1000nM [21], [22]). As the percentage reduction increases, the steady-state calcium uptake increases and this uptake begins at earlier times. For reductions in CBF less than or equal to 70% however, no uptake is observed. One possible biological explanation for this is that the calcium influx at these smaller CBF reductions is low enough and the energy of the cell high enough that calcium pumps can still maintain pre-ischaemic concentrations (see Section 2.2.4.2). Figure 3.3 shows that for reductions in CBF greater than 70%, the astrocytes also begin to uptake calcium ions at the same time as the neurons. However, as CBF reduction increases, the maximal calcium uptake into the astrocytes *decreases.* As this does not appear to conform to physiological observations, we believe that this decrease is a 'quirk' of the model.

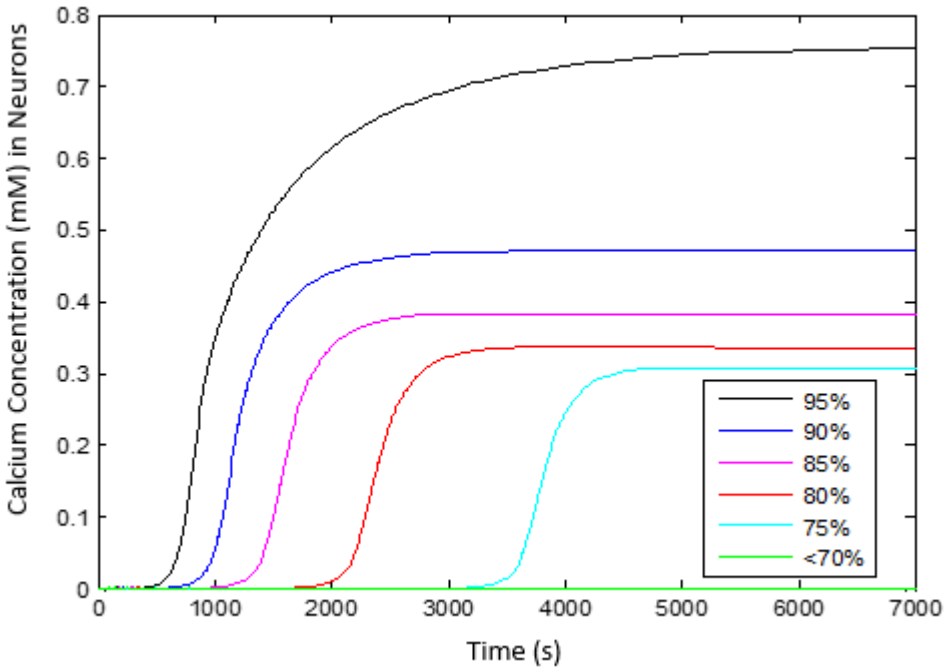

Figure 3.2: Time-course plot of calcium concentration in neurons after cerebral blood flow is reduced by five different values.

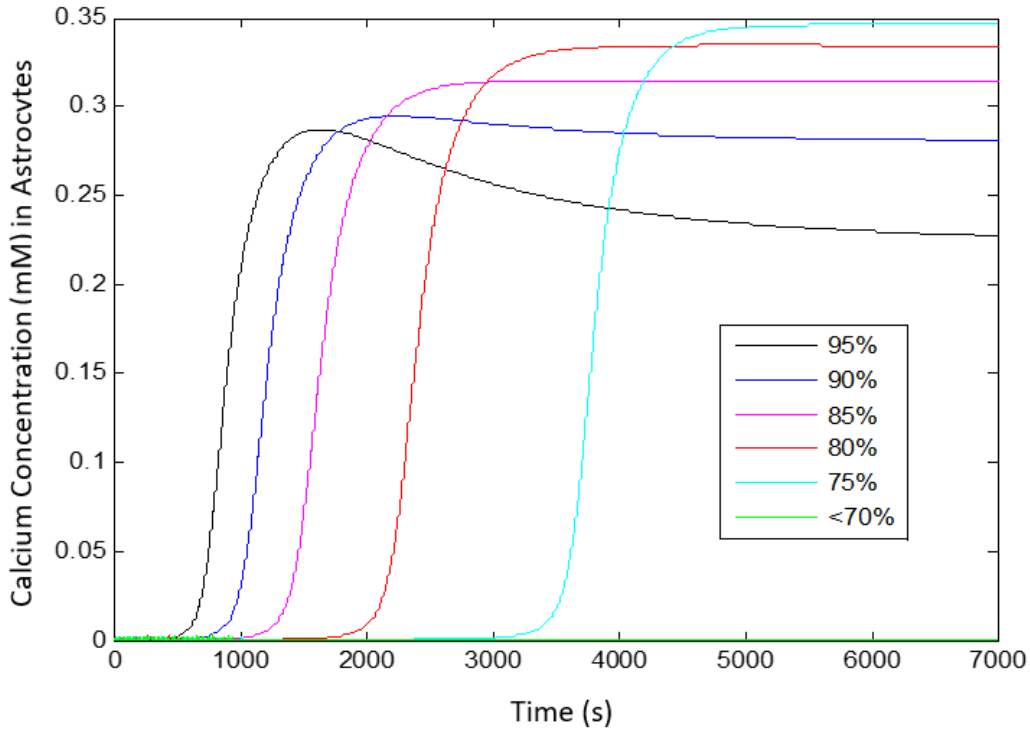

Figure 3.3: Time-course plot of calcium concentration in astrocytes after cerebral blood flow is reduced by five different values.

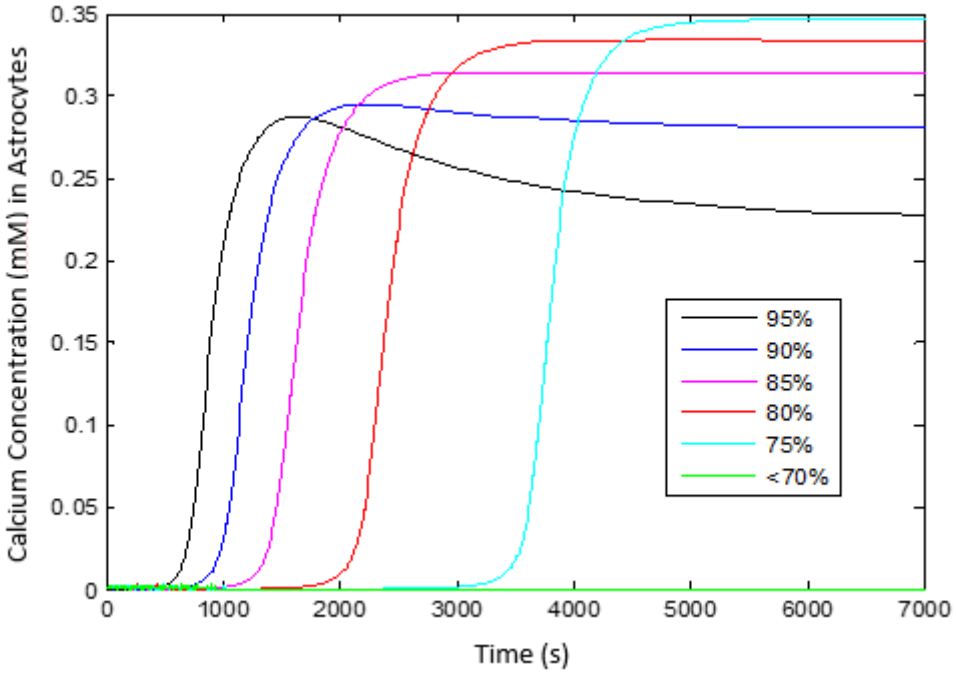

Figure 3.4: Time-course plot of calcium concentration in the extracellular space after cerebral blood flow is reduced by five different values.

Again, for CBF reduction less than 70%, no uptake is observed; this is again possibly due to the maintenance of homeostasis by calcium pumps. Figure 3.4 shows that extracellular calcium concentration decreases for CBF reductions of over 70%, as the calcium ions move into the astrocytes and neurons. For reductions of under 70%, the calcium concentration is almost constant as homeostasis can still be maintained by the calcium pumps.

3.2 Fitting to a Second Order Model

Noticing the presence of overshoot in Figure 3.3, we suggest that the simplest model suitable for fitting is a second order ODE. Parameter values for this ODE can be found by using the above equations to find C_a as a function of g_a and g_n alone, and repeating the elimination process to find C_e as a function of g_a and g_n alone. This yields two equations for g_a and g_n which can be matched

to equation 3.4, leaving these variables as functions of CBF alone. Using the above procedure, we find that the resultant ODE for the astrocytic compartment is:

$$\frac{\varphi_e\varphi_n\varphi_a}{\gamma_{ae}\gamma_{ne}}\frac{d^3C_a}{dt^3}+\left(\frac{\varphi_e\varphi_n}{\gamma_{ne}}+\frac{\varphi_e\varphi_a}{\gamma_{ae}}+\frac{\varphi_n\varphi_a}{\gamma_{ae}}+\frac{\varphi_a\varphi_n}{\gamma_{ne}}\right)\frac{d^2C_a}{dt^2}+(\varphi_a+\ \varphi_e+\varphi_n)\frac{dC_a}{dt}$$

$$=\frac{\varphi_e\varphi_n}{\gamma_{ae}\gamma_{ne}}\frac{d^2g_a}{dt^2}+\left(\frac{\varphi_n}{\gamma_{ae}}+\frac{\varphi_n}{\gamma_{ne}}+\frac{\varphi_e}{\gamma_{ae}}\right)\frac{dg_a}{dt}+\ g_a+g_n\ \text{(3.5)}$$

Integrating equation (3.5) gives the following second-order ODE:

$$\frac{\varphi_e\varphi_n\varphi_a}{\gamma_{ae}\gamma_{ne}}\frac{d^2C_a}{dt^2}+\left(\frac{\varphi_e\varphi_n}{\gamma_{ne}}+\frac{\varphi_e\varphi_a}{\gamma_{ae}}+\frac{\varphi_n\varphi_a}{\gamma_{ae}}+\frac{\varphi_a\varphi_n}{\gamma_{ne}}\right)\frac{dC_a}{dt}\ +(\varphi_a+\ \varphi_e+\varphi_n)C_a$$

$$=\frac{\varphi_e\varphi_n}{\gamma_{ae}\gamma_{ne}}\frac{d^2h_a}{dt^2}+\left(\frac{\varphi_n}{\gamma_{ae}}+\frac{\varphi_n}{\gamma_{ne}}+\frac{\varphi_e}{\gamma_{ae}}\right)\frac{dh_a}{dt}+\ h_a+\ h_n+m\ \text{(3.6)}$$

where:

$$g_a=\frac{dh_a}{dt}\ \text{(3.7)}$$

$$g_n=\frac{dh_n}{dt}\ \text{(3.8)}$$

and m is a time-independent constant.

Equation (3.6) can be rearranged to give a second-order differential equation of the form:

$$\ddot{y}(t)+2\zeta\omega_n\dot{y}(t)+\ \omega_n^2\,y(t)=f(t)\ \text{(3.9)}$$

where $y(t)$ represents the calcium response (corresponding to C in the equations above), $f(t)$ the forcing function (describing the change in CBF), corresponding to g_a and g_n, the generation terms of equations (3.7) and (3.8), while ζ is the damping factor and ω_n the natural frequency.

The LHS of equations (3.5) and (3.6) can now be matched to equation (3.4). The sum of the three volume fractions, φ_{sum}, is:

$$\varphi_{sum}=\varphi_a+\ \varphi_e+\varphi_n\ \text{(3.10)}$$

Therefore, the equations can be scaled by $\frac{\omega_n^2}{\varphi_{sum}}$, in order to match the lowest-order terms. This leaves the following equations:

$$\frac{\omega_n^2}{\varphi_{sum}} \frac{\varphi_e \varphi_n \varphi_a}{\gamma_{ae} \gamma_{ne}} = 1 \text{ (3.11)}$$

$$\frac{\omega_n}{\varphi_{sum}} \left(\frac{\varphi_e \varphi_n}{\gamma_{ne}} + \frac{\varphi_e \varphi_a}{\gamma_{ae}} + \frac{\varphi_n \varphi_a}{\gamma_{ae}} + \frac{\varphi_a \varphi_n}{\gamma_{ne}} \right) = 2\zeta \text{ (3.12)}$$

This means that an expression for γ_{ne} in terms of γ_{ae} is:

$$\gamma_{ne} = \frac{\omega_n^2}{\varphi_{sum}\, \gamma_{ae}} \varphi_e \varphi_n \varphi_a \text{ (3.13)}$$

Substituting this expression into the second equation and rearranging gives the following second-order algebraic equation for γ_{ae}:

$$(\varphi_e \varphi_n + \varphi_a \varphi_n)\, \gamma_{ae}^2 - 2\xi \omega_n \varphi_e \varphi_n \varphi_a \gamma_{ae} + \frac{(\varphi_n \varphi_a + \varphi_e \varphi_a)\omega_n^2}{\varphi_{sum}} \varphi_e \varphi_n \varphi_a = 0 \text{ (3.14)}$$

In order for this quadratic equation to contain real roots for γ_{ae}, its discriminant, Δ, must be less than zero.

$$\Delta = (2\xi \omega_n \varphi_e \varphi_n \varphi_a)^2 - 4(\varphi_e \varphi_n + \varphi_a \varphi_n) \frac{(\varphi_n \varphi_a + \varphi_e \varphi_a)\omega_n^2}{\varphi_a + \varphi_e + \varphi_n} \varphi_e \varphi_n \varphi_a < 0 \text{ (3.15)}$$

Hence, the inequality (3.15) is satisfied if:

$$\xi^2 > \frac{(\varphi_e + \varphi_a)(\varphi_e + \varphi_n)}{\varphi_{sum}\, \varphi_e} \text{ (3.16)}$$

From the parameter values used in the model by Cloutier *et al.,* [54], the volume fractions are:

$\varphi_n = 0.45,\ \varphi_a = 0.25, \varphi_e = 0.2$ for the

Thus:

$$\xi > 1.2748 \text{ (3.17).}$$

However, the model generates calcium dynamics that, at higher CBF drops, display overshoot (see Figure 3.3). For a system modelled by the second order differential equation, (3.9), overshoot can only occur if the condition:

$$0 < \xi < 1 \quad (3.18)$$

is satisfied. Therefore, a valid conclusion is that the form of the equations will need to change in order to display this overshoot.

3.3 Calcium-Dependent Generation Terms and Third Order Model

In response to the finding in the previous section that the second order fitting is not adequate, we attempt to address this inadequacy by changing the generation terms in equations (3.1) and (3.2) to be dependent upon the calcium concentration; as we shall see, this leads to a third order ODE.

$$g_a = g_{a0} + g_{a1}C_a \quad (3.19)$$

$$g_n = g_{n0} + g_{n1}C_n \quad (3.20)$$

Substituting these new generation terms back into equations (3.1) and (3.2) again, in order to find an equation only in terms of C_a, we obtain the following equation:

$$\frac{d^3C_a}{dt^3} + \left(\frac{\gamma_{ae}}{\varphi_a} + \frac{\gamma_{ae}}{\varphi_e} + \frac{\gamma_{ne}}{\varphi_e} + \frac{\gamma_{ne}}{\varphi_n} - \frac{g_{a1}}{\varphi_a} - \frac{g_{n1}}{\varphi_n}\right)\frac{d^2C_a}{dt^2} + \left(\frac{\gamma_{ae}\gamma_{ne}}{\varphi_a\varphi_e} + \frac{\gamma_{ae}\gamma_{ne}}{\varphi_a\varphi_n} + \frac{\gamma_{ae}\gamma_{ne}}{\varphi_e\varphi_n} - \frac{\gamma_{ae}g_{a1}}{\varphi_a\varphi_e} - \frac{\gamma_{ne}g_{a1}}{\varphi_a\varphi_e} - \frac{\gamma_{ne}g_{a1}}{\varphi_a\varphi_n} - \frac{\gamma_{ae}g_{n1}}{\varphi_e\varphi_n} - \frac{\gamma_{ne}g_{n1}}{\varphi_e\varphi_n} - \frac{\gamma_{ne}g_{a1}}{\varphi_a\varphi_n} + \frac{g_{a1}g_{n1}}{\varphi_a\varphi_n}\right)\frac{dC_a}{dt} + \left(-\frac{(g_{a1}+g_{n1})\gamma_{ae}\gamma_{ne}}{\varphi_a\varphi_e\varphi_n} + \frac{g_{a1}g_{n1}(\gamma_{ae}+\gamma_{ne})}{\varphi_a\varphi_e\varphi_n}\right)C_a = -\frac{g_{a0}g_{n1}(\gamma_{ae}+\gamma_{ne})}{\varphi_a\varphi_e\varphi_n} + (g_{a0} + g_{n0})\frac{\varphi_a\varphi_e\varphi_n}{\gamma_{ae}\gamma_{ne}} \quad (3.21)$$

The corresponding equation for C_n is:

$$\frac{d^3C_n}{dt^3}+\left(\frac{\gamma_{ae}}{\varphi_a}+\frac{\gamma_{ae}}{\varphi_e}+\frac{\gamma_{ne}}{\varphi_e}+\frac{\gamma_{ne}}{\varphi_n}-\frac{g_{a1}}{\varphi_a}-\frac{g_{n1}}{\varphi_n}\right)\frac{d^2C_n}{dt^2}$$

$$+\left(\frac{\gamma_{ae}\gamma_{ne}}{\varphi_e\varphi_n}+\frac{\gamma_{ae}\gamma_{ne}}{\varphi_a\varphi_n}+\frac{\gamma_{ae}\gamma_{ne}}{\varphi_e\varphi_n}-\frac{\gamma_{ae}g_{a1}}{\varphi_a\varphi_e}-\frac{\gamma_{ne}g_{a1}}{\varphi_a\varphi_e}-\frac{\gamma_{ne}g_{a1}}{\varphi_a\varphi_n}-\frac{\gamma_{ae}g_{n1}}{\varphi_e\varphi_n}-\frac{\gamma_{ne}g_{n1}}{\varphi_e\varphi_n}-\frac{\gamma_{ne}g_{a1}}{\varphi_a\varphi_n}\right.$$

$$\left.+\frac{g_{a1}g_{n1}}{\varphi_a\varphi_n}\right)\frac{dC_n}{dt}+\left(-\frac{(g_{a1}+g_{n1})\gamma_{ae}\gamma_{ne}}{\varphi_a\varphi_e\varphi_n}+\frac{g_{a1}g_{n1}(\gamma_{ae}+\gamma_{ne})}{\varphi_a\varphi_e\varphi_n}\right)C_n$$

$$=-\frac{g_{a1}g_{n0}(\gamma_{ae}+\gamma_{ne})}{\varphi_a\varphi_e\varphi_n}+(g_{a0}+g_{n0})\frac{\varphi_a\varphi_e\varphi_n}{\gamma_{ae}\gamma_{ne}} \quad (3.22)$$

The only difference between the coefficients of the two calcium compartments is the first term on the RHS of both equations.

Since the coefficient of the zeroth derivative of calcium concentration in both compartments is no longer zero, the equation cannot be integrated through; it represents a coupled third-order system. There are now six parameters to fit. However, before proceeding, there are a couple of characteristics of the third order model that we investigate.

3.3.1 Stability Analysis

A stability analysis for solutions to the third order model is conducted and presented.

3.3.1.1 Steady-State Relations

When the 0-dimensional system is at steady-state, the following relations hold:

$$\gamma_{ne}=-\frac{\overline{C_a}-\overline{C_e}}{\overline{C_n}-\overline{C_e}}\gamma_{ae} \quad (3.23)$$

where the overbar indicates the steady-state value.

Since the steady-state concentration of calcium is largest in the extracellular compartment, for all CBF drops, this implies that one of γ_{ae} or γ_{ne} must be negative and the other positive.

Also:

$$g_{a0}+g_{a1}\overline{C_a}+(g_{n0}+g_{n1}\overline{C_n})=0 \quad (3.24)$$

3.3.1.2 Stability Criteria

This subsection investigates the stability of the 0-dimensional mass transfer system. This involves examining the eigenvalues associated with the system. Should any of the eigenvalues have positive real part, the system will be unstable.

The system of equations, (3.1)-(3.3), can be rewritten in the form:

$$\frac{d}{dt}\boldsymbol{C} = \boldsymbol{J}\boldsymbol{C} \quad (3.25)$$

where:

$$\boldsymbol{J} = \begin{bmatrix} \frac{(g_{a1}-\gamma_{ae})}{\varphi_a} & 0 & \frac{\gamma_{ae}}{\varphi_a} \\ 0 & \frac{(g_{n1}-\gamma_{ne})}{\varphi_n} & \frac{\gamma_{ne}}{\varphi_n} \\ \frac{\gamma_{ae}}{\varphi_e} & \frac{\gamma_{ne}}{\varphi_e} & \frac{-(\gamma_{ae}+\gamma_{ne})}{\varphi_e} \end{bmatrix} \quad (3.26)$$

and

$$\boldsymbol{C} = [C_a, C_n, C_e]^T \quad (3.27)$$

The eigenvalues are found by calculating the determinant of the matrix $(\boldsymbol{J} - \lambda\boldsymbol{I})$ and setting the resultant polynomial in λ, known as the characteristic polynomial, $p(\lambda)$, to zero.

The characteristic polynomial is found to be:

$$p(\lambda) = \lambda^3 - \left(\frac{(g_{a1}-\gamma_{ae})}{\varphi_a} + \frac{(g_{n1}-\gamma_{ne})}{\varphi_n} - \frac{(\gamma_{ae}+\gamma_{ne})}{\varphi_e}\right)\lambda^2 + \left(\frac{(g_{a1}-\gamma_{ae})(g_{n1}-\gamma_{ne})}{\varphi_a\varphi_n} - \frac{g_{a1}(\gamma_{ae}+\gamma_{ne})-\gamma_{ae}\gamma_{ne}}{\varphi_a\varphi_e} + \frac{g_{n1}\gamma_{ae}+g_{n1}\gamma_{ne}-\gamma_{ae}\gamma_{ne}}{\varphi_n\varphi_e}\right)\lambda - \frac{(g_{a1}+g_{n1})\gamma_{ae}\gamma_{ne}-g_{a1}g_{n1}(\gamma_{ae}+\gamma_{ne})}{\varphi_a\varphi_n\varphi_e} \quad (3.28)$$

Setting this polynomial to zero yields the characteristic equation, the solutions of which represent the three (possibly complex) eigenvalues. However, to find the nature of these eigenvalues, it is simpler to use the Routh-Hurwitz criterion. This states that, in the case of a cubic polynomial with equation:

$$p_3(\lambda) = a\lambda^3 + b\lambda^2 + c\lambda + d = 0 \quad (3.29)$$

Then the three eigenvalues all have negative real parts if and only if all four of the following conditions are met:

1. $a > 0$ (3.30)
2. $b > 0$ (3.31)
3. $d > 0$ (3.32)
4. $bc - ad > 0$ (3.33)

Multiplying the characteristic polynomial above gives:

$$a = 1 \quad (3.34)$$

$$b = \frac{(\gamma_{ae} - g_{a1})}{\varphi_a} + \frac{(\gamma_{ne} - g_{n1})}{\varphi_n} + \frac{(\gamma_{ae} + \gamma_{ne})}{\varphi_e} \quad (3.35)$$

$$c = \frac{(g_{a1} - \gamma_{ae})(g_{n1} - \gamma_{ne})}{\varphi_a \varphi_n} + \frac{-g_{a1}(\gamma_{ae} + \gamma_{ne}) + \gamma_{ae}\gamma_{ne}}{\varphi_a \varphi_e} + \frac{g_{n1}\gamma_{ae} + g_{n1}\gamma_{ne} - \gamma_{ae}\gamma_{ne}}{\varphi_n \varphi_e} \quad (3.36)$$

$$d = \frac{-(g_{a1} + g_{n1})\gamma_{ae}\gamma_{ne} + g_{a1}g_{n1}(\gamma_{ae} + \gamma_{ne})}{\varphi_a \varphi_n \varphi_e} \quad (3.37)$$

Next, to simplify the subsequent equations and noting, from equation (3.22), that γ_{ne} is a negative multiple of γ_{ae}, we make the substitution:

$$\gamma_{ne} = -m\gamma_{ae} \quad (3.38)$$

where m is a positive real number, equal to:

$$m = \frac{\overline{C_a} - \overline{C_e}}{\overline{C_n} - \overline{C_e}} \quad (3.39)$$

Note that m is positive since the steady-state concentration of extracellular calcium is found to be greater than those in the other compartments.

Simplification of the analysis can be achieved by making the approximation:

$g_{a1} \approx 0$ (3.40)

This approximation is used here because simulations (not shown here) have shown that, after initial fitting of parameters to match the dynamics in just two compartments (the astrocytes and neurons), g_{a1} was shown to be very close to zero.

Hence, with condition 1 of the Routh-Hurwitz criterion already satisfied, the remaining conditions require the following to be satisfied:

Condition 3 implies that:

$$\frac{g_{a1}g_{n1}\gamma_{ae}+g_{a1}g_{n1}\gamma_{ne}-g_{a1}\gamma_{ae}\gamma_{ne}-g_{n1}\gamma_{ae}\gamma_{ne}}{\varphi_a\varphi_n\varphi_e} > 0 \quad (3.41)$$

Since:

$$\varphi_a\varphi_n\varphi_e > 0 \quad (3.42)$$

Making the approximation in (3.40) leads to the following inequality:

$$mg_{n1}\gamma_{ae}^2 > 0 \quad (3.43)$$

Therefore, this condition reduces elegantly to the following inequality:

$$g_{n1} > 0 \quad (3.44)$$

Condition 2 implies that:

$$\frac{(\gamma_{ae}-g_{a1})}{\varphi_a} + \frac{(\gamma_{ne}-g_{n1})}{\varphi_n} + \frac{(\gamma_{ae}+\gamma_{ne})}{\varphi_e} > 0 \quad (3.45)$$

After applying the substitution in equation (3.39) and also the approximation in (3.40), the following must hold:

$$\left(\left(\frac{\varphi_n}{\varphi_e}+\frac{\varphi_n}{\varphi_a}\right) - m\left(1+\frac{\varphi_n}{\varphi_e}\right)\right)\gamma_{ae} > g_{n1} \quad (3.46)$$

Equation (3.46) gives an inequality expressing a linear relationship between γ_{ae} and g_{n1}. This results in a straight line, above or below which the inequality and, hence, condition 2, is satisfied.

From condition 4, making the approximation from (3.40), the following holds:

$$\left(\frac{-\gamma_{ae}(g_{n1}+m\gamma_{ae})}{\varphi_a\varphi_n}-\frac{m\gamma_{ae}^2}{\varphi_a\varphi_e}+\frac{(-g_{n1}\gamma_{ae}+mg_{n1}\gamma_{ae}-m\gamma_{ae}^2)}{\varphi_n\varphi_e}\right)\left(\frac{\gamma_{ae}(1-m)}{\varphi_e}-\frac{(m\gamma_{ae}+g_{n1})}{\varphi_n}+\frac{\gamma_{ae}}{\varphi_a}\right)-\frac{mg_{n1}\gamma_{ae}^2}{\varphi_a\varphi_n\varphi_e}>0 \quad (3.47)$$

The graph of this inequality is most easily obtained numerically. All four conditions must be satisfied simultaneously and the proceeding section gives a simple method which can be used to determine whether or not there exists a region in the (γ_{ae}, g_{n1})-plane where the system is stable.

3.3.1.3 Method

All four conditions of the Routh-Hurwitz criterion must be satisfied for the eigenvalues to be negative and, hence, the system to be stable. Moreover, the criterion must be satisfied at each CBF value. The procedure used to test for stability, at each value of CBF, is as follows:

1. Calculate the associated m value for each CBF drop, from equation (3.39).
2. Determine:

$$sign\left(\left(\frac{\varphi_n}{\varphi_e}+\frac{\varphi_n}{\varphi_a}\right)-m\left(1+\frac{\varphi_n}{\varphi_e}\right)\right) \quad (3.48)$$

   This is the sign of the coefficient of γ_{ae} in inequality (3.45).

3. Determine the domain of interest. This will be all the positive values of g_{n1}, to satisfy condition 3, and the positive or negative values of γ_{ae}, depending on whether the sign determined in step 2 is positive or negative, respectively.
4. Calculate, in the above domain, values for the LHS of both equations (3.46) and (3.47), which represent conditions 2 and 4 respectively, and determine if there is a region in the domain where both are positive.

3.3.1.4 Results and Conclusions

The method above was implemented for different CBF values to determine stability. The results are summarised in Table 3.1.

The system is unstable for all CBF values. For CBF drops between 91% and 95%, the domain of interest is $\{(g_{n1}, \gamma_{ae}) |\ g_{n1} \in \mathbb{R}^+, \gamma_{ae} \in \mathbb{R}^-\}$. This is since the sign determined in expression (3.48) is negative and, hence, the sign of γ_{ae}must also be negative, to be able to satisfy condition 2. However, the LHS of equation (3.46) is never positive and, hence, condition 4 is never satisfied in the domain. This can be seen in Figure 3.5a, where the green region, representing the area where both conditions are fulfilled, is outside the domain of interest (as is the orange region, where only condition 4 holds).

On the other hand, for CBF drops between 75% to 90%, the system is unstable because, while conditions 2 and 4 are *individually* satisfied at certain points in the domain of interest, they are never *simultaneously* satisfied. Note that the domain of interest is now $\{(g_{n1}, \gamma_{ae}) |\ g_{n1} \in \mathbb{R}^+, \gamma_{ae} \in \mathbb{R}^+\}$, since the sign determined in expression (3.48) is positive and, hence, the sign of γ_{ae} must also be positive, to be able to satisfy condition 2. This is shown in Figure 3.5b, where blue and orange regions, representing the fulfilment of conditions 2 and 4 respectively, never coincide in the domain of interest.

Another way to understand this is to realise that equation (3.36), which gives the value for c in the characteristic equation (3.29), is always found to be negative in this domain of interest (when calculated numerically) and, hence, in order to be able to satisfy condition 4 of the Routh-Hurwitz criterion, shown in inequality (3.33), b must be negative (since the domain of interest ensures that condition 3, shown in equality (3.32), holds); this, however, then contradicts condition 2, shown in inequality (3.31). Hence, only one of condition 2 or condition 4 must hold at any point and, hence, from the Routh-Hurwitz criterion, the system is unstable.

CBF Drop	m	$sign\left(\left(\frac{\varphi_n}{\varphi_e}+\frac{\varphi_n}{\varphi_a}\right)-m\left(1+\frac{\varphi_n}{\varphi_e}\right)\right)$	$sign(\gamma_{ae})$ (to *be able* to satisfy condition 2)	Stability of System
95%	2.79	−	−	Unstable (1)
94%	1.91	−	−	Unstable (1)
93%	1.58	−	−	Unstable (1)
92%	1.41	−	−	Unstable (1)
91%	1.31	−	−	Unstable (1)
90%	1.2376	+	+	Unstable (2)
85%	1.0725	+	+	Unstable (2)
80%	1.0006	+	+	Unstable (2)
75%	0.9634	+	+	Unstable (2)

Table 3.1: A summary of the results of each step in the method. The system is unstable for all CBF drops since, for (1), condition 4 is not satisfied, while for (2), both conditions are never simultaneously satisfied.

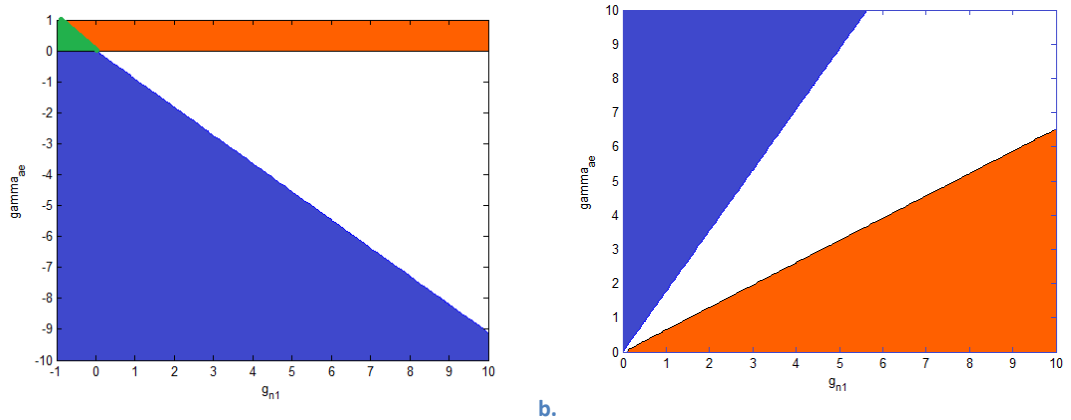

a. b.

Figure 3.5: Graphs showing the regions where conditions 2 and 4 are satisfied, for (a): 93% and (b): 85% CBF drops. In blue is the region satisfying condition 2, while the orange region satisfies condition 4. The green region, which indicates fulfilment of both conditions, nevertheless does not exist inside the region of interest: $\{(g_{n1}, \gamma_{ae}) | \ g_{n1} \in \mathbb{R}^+, \gamma_{ae} \in \mathbb{R}^-\}$.

3.3.2 Proof of Lack of Overshoot

As seen in the previous chapter, the synthetic data produce calcium responses to simulated ischaemic stroke that may display an overshoot, before settling down at the steady-state value. The following analysis examines whether or not the 3rd order model can display overshoot.

γ_{ne} is expressed in terms of γ_{ae}, from equation (1.41), and we also make the approximation in equation (1.43), stating that g_{a1} is close to zero.

Hence, for simplicity we write:

$g_{n1} = g$ (3.49)

$\gamma_{ae} = -\gamma_{ne} = \gamma$ (3.50)

These two steps reduce the number of parameters involved in the transfer function from four to two. Then, the denominator, $H(s)$, of the transfer function for the third order system is:

$H(s) = s^3 + as^2 + bs + c$ (3.51)

where:

$a = (9 - 7m)\gamma_{ae} - 2g$ (3.52)

$b = -38m\gamma^2 - 10(m-1)\gamma g$ (3.53)

$c = 40m\gamma^2 g$ (3.54)

For overshoot to occur in this system, the two of the three poles of the transfer function must be complex conjugates, while the other is real. This is since the transfer function of a 3rd order system, which is of the form of equation (3.51), has three roots and three real coefficients. Equation (3.51) has three roots, which may be complex-valued. However, if complex roots do exist, then they must exist as a complex conjugate pair (since the coefficients of the equation are all real). Hence, either all three roots are real or one root is real and the others are a complex conjugate pair.

If all three roots are real, then either the system is asymptotically stable, if all three roots are negative, or asymptotically unstable if at least one root is not negative. If there exists a complex

conjugate pair, however, then oscillations or overshoot can occur, similar to a second-order system.

For this system, a complex conjugate pair of solutions to the transfer function occurs if:

$$f(p,q) = \frac{p^3}{27} + \frac{q^2}{4} > 0 \tag{3.55}$$

where:

$$p = -\frac{a^2}{3} + b \tag{3.56}$$

$$q = 2\left(\frac{a}{3}\right)^3 - \frac{ab}{3} + c \tag{3.57}$$

However, no combination of the two variables, g_{n1} and γ_{ae}, is able to satisfy the inequality (3.55). For instance, we show the function $f(p,q)$ when $g_{n1} = 0$ in Figure 3..6, where:

$$\gamma_{ne} = -\gamma_{ae} \tag{3.58}$$

This occurs when the CBF drop is 80%, from Table 3.1.

It can be seen that only when both variables are exactly 0 will the absolute maximum be reached; yet, this happens to be 0 and so inequality (3.55) is not satisfied.

Even when γ_{ne} is made to be independent of γ_{ae} and the approximation in equation (3.40) is relaxed, a similar analysis still shows that inequality (3.55) is never satisfied and, thus, overshoot still does not occur.

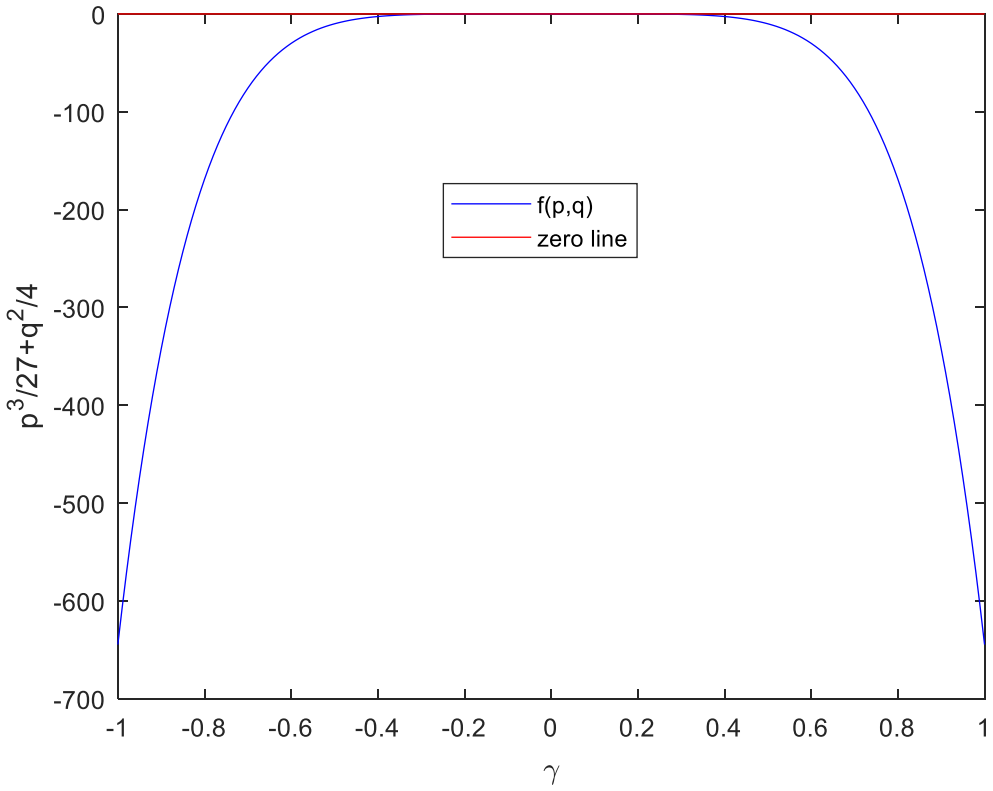

Figure 3.6: A plot showing, in blue, the function $f(p,q)$ from Equation (3.55) and, in red, the function $g(p,q) = 0$. The inequality required for overshoot is never satisfied.

3.4 Adding Storage Compartments to the Model

Due to the unstable nature of the 3rd order system, the model was expanded to include compartments representing calcium storage. In the first instance, the model should be as simple as possible. Therefore, an existing model by Lavrentovich and Hemkin [66], describing the oscillatory behaviour of astrocytic calcium, was modified.

This model contains three compartments, one representing the concentration of astrocytic calcium, another the storage of calcium in the endoplasmic reticulum (ER) and the third the IP_3 levels in the cell. IP_3 is a chemical messenger that, after being activated by cellular calcium, is able to bind to receptors on the ER, triggering release of calcium stored there.

However, for simplicity, the assumption here is that the concentration of IP_3 is constant. This reduces the model to two compartments, whose reduced equations are as follows:

$$\frac{dC_a}{dt} = v_{in} - k_{out}C_a + v_{CICR} - v_{serca} + k_f(C_{aer} - C_a) \quad (3.60)$$

$$\frac{dC_{aer}}{dt} = -v_{CICR} + v_{serca} - k_f(C_{aer} - C_a) \quad (3.61)$$

where:

- C_a is the concentration of calcium in the astrocyte.
- C_{aer} is the concentration of calcium in the ER.
- v_{in} is the rate at which calcium enters the astrocyte from the extracellular space.
- k_{out} is the rate at which calcium is dispelled from the astrocyte.
- k_f is the rate of diffusion-driven calcium leakage from the ER to the astrocyte .
- v_{CICR} is the term representing IP_3-driven calcium movement from the ER to the astrocyte. Lavrentovich and Hemkin [66], propose that it be composed of 3 terms: first, a Gaussian-shaped function in terms of astrocytic calcium concentration, since the receptor-bound IP_3 is dependent on the latter in a bell-shaped manner, second, a Hill function in terms of IP_3 concentration and, finally, the difference in calcium concentration between the ER and astrocyte.
- v_{serca} is the term representing calcium influx from the astrocyte into the ER, due to mechanisms involving ATPase from the ER. This is the term that replenishes calcium ions in the ER and has the form of a Hill function, in terms of C_a.

Before this model can be coupled to equations (3.1)-(3.3), it must first be adapted. A couple of assumptions are required: the first is that a similar mechanism occurs in the neurons and, therefore, the equations representing that compartment 'mirror' equations (3.60) and (3.61). Next, the v_{CICR} term is modified by reducing it from 3 component terms, in the corresponding version of Lavrentovich and Hemkin, to 1, leaving only the difference in calcium concentration between ER and astrocyte:

$$v_{CICR} = v_C(C_{aer} - C_a) \quad (3.62)$$

Since the first term of Lavrentovich and Hemkin's v_{CICR}, which is in terms of the astrocytic calcium concentration and varies between 0 and 1, we assume that this term can be represented by a constant. Also, we neglect the second term, the Hill function in terms of IP_3, because of the assumption that the IP_3 concentration is approximately constant. This results in equation (3.62). Hence, the v_{CICR} and $k_f(C_{aer} - C_a)$ terms are effectively combined. Moreover, in Lavrentovich and Hemkin's model, both the v_{in} term, representing calcium influx from the extracellular fluid, as well as the $k_{out}C_a$ term, are similar to the mass transfer term in equation (3.1) and, hence, they have already been incorporated.

The v_{SERCA} term, however, needs to be incorporated in a new model, since this is the term that replenishes the levels of calcium ions in the ER. This has the following form:

$$v_{SERCA} = v_{S1}\left(\frac{C_a^2}{C_a^2+v_{S2}^2}\right)$$

$$\approx \frac{v_{s1}}{2v_{s2}}C_a = v_{s3}C_a \quad (3.63)$$

The approximation in equation (3.63) holds when the concentration of astrocytic calcium is low ($<$ v_{s2}).

Finally, terms are added that correspond to the active transport of calcium ions from inside the cell to the extracellular space, by means of a Ca^{2+}-ATP pump. This is represented by:

$$v_{pump} = v_p C_a \quad (3.64)$$

This term was originally of the form of a Hill function in MacDonald and Silva, [27]; here, it is simplified to be of linear form. This results in the following new model, a schematic of which is shown in Figure 3.7:

$$\varphi_a \frac{\partial C_a}{\partial t} = v_{CICR} - v_{SERCA} - \gamma_{ae}(C_a - C_e) - v_{pump}$$

$$= v_C(C_{aer} - C_a) - v_{s3}C_a - \gamma_{ae}(C_a - C_e) - v_p C_a \quad (3.65)$$

$$\varphi_{aer}\frac{\partial C_{aer}}{\partial t} = -v_{CICR} + v_{SERCA}$$

$$= -v_C(C_{aer} - C_a) + v_{s3}C_a \quad (3.66)$$

$$\varphi_n\frac{\partial C_n}{\partial t} = v_{CICRn} - v_{SERCAn} - \gamma_{ne}(C_n - C_e) - v_{pumpn}$$

$$= v_{Cn}(C_{ner} - C_n) - v_{s3n}C_n - \gamma_{ne}(C_n - C_e) - v_{pn}C_n \quad (3.67)$$

$$\varphi_{ner}\frac{\partial C_{ner}}{\partial t} = -v_{CICRn} + v_{SERCAn}$$

$$= -v_{Cn}(C_{ner} - C_n) + v_{s3n}C_n \quad (3.68)$$

$$\varphi_e\left(\frac{\partial C_e}{\partial t} + U_e.\nabla(C_e)\right) = \nabla.\left(D.\nabla(\varphi_e C_e)\right) + \gamma_{ae}(C_a - C_e) + \gamma_{ne}(C_n - C_e) + v_{pump} + v_{pumpn}$$

$$= \nabla.\left(D.\nabla(\varphi_e C_e)\right) + \gamma_{ae}(C_a - C_e) + \gamma_{ne}(C_n - C_e) + v_p C_a + v_{pn}C_n \quad (3.69)$$

where:

- φ_{aer} and φ_{ner} are the volume fractions of the astrocytic and neuronal ER compartments, respectively. Note that the volume fractions of φ_a and φ_n will both be reduced so that the sum of the ER and reduced volume fractions remain the same as the original.
- v_{CICRn} is the term corresponding to v_{CICR} in the neurons, where:

  $$v_{CICRn} = v_{Cn}(C_{ner} - C_n) \quad (3.70)$$

- v_{SERCAn} is the term corresponding to v_{SERCA} in the neurons, where:

  $$v_{SERCAn} = v_{s3n}C_n \quad (3.71)$$

- v_{pumpn} is the term corresponding to v_{pump} in the neurons, where:

  $$v_{pumpn} = v_{pn}C_n \quad (3.72)$$

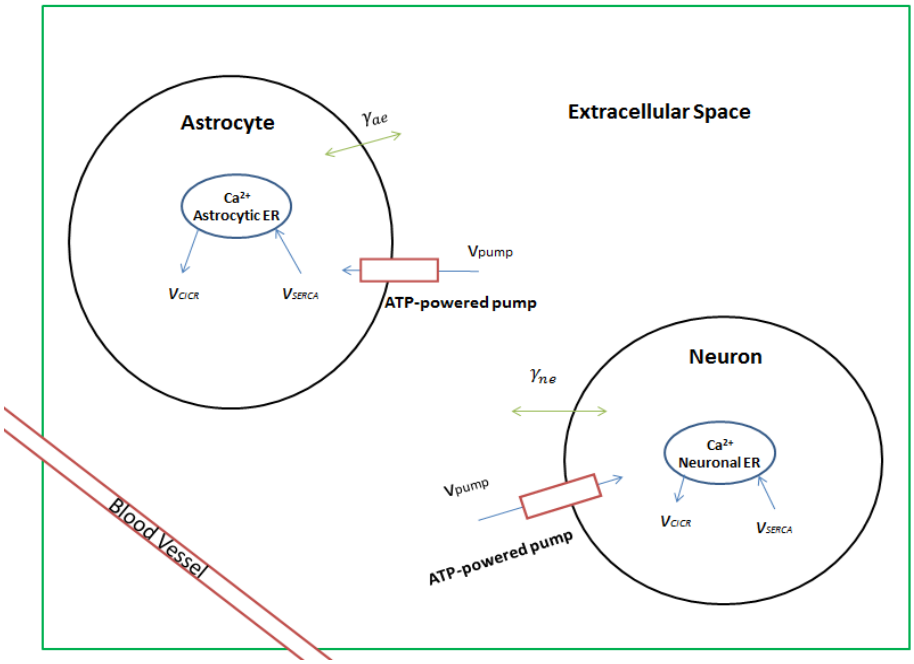

Figure 3.7: The schematic of our modified mathematical model.

3.4.1 Steady-State and Stability Analyses

A steady-state analysis can be used to determine some relations between certain parameters. The following equalities must hold:

$$v_p = \left(\frac{\overline{C_e}}{\overline{C_a}} - 1\right)\gamma_{ae} \quad (3.73)$$

$$v_{s3} = \left(\frac{\overline{C_{aer}}}{\overline{C_a}} - 1\right)V_c \quad (3.74)$$

$$v_{pn} = \left(\frac{\overline{C_e}}{\overline{C_n}} - 1\right)\gamma_{ne} \quad (3.75)$$

$$v_{s3n} = \left(\frac{\overline{C_{ner}}}{\overline{C_n}} - 1\right)V_{cn} \quad (3.76)$$

where the overbar indicates steady-state concentrations.

These relations can be used to aid the determination of the unknown parameter values:

$\gamma_{ae}, \gamma_{ne}, v_C, v_{cn}, v_{sn3}$ and v_{pn}.

3.4.2 Stability of New Model

As was the case for the previous model, the new model can be written in matrix form, as it is linear:

$$\frac{d\bar{C}}{dt} = \boldsymbol{J_{new}}\bar{C} \quad (3.77)$$

where:

$$\boldsymbol{J_{new}} = \begin{bmatrix} -\frac{v_c+v_{s3}+\gamma_{ae}+v_p}{\varphi_a} & \frac{v_c}{\varphi_a} & 0 & 0 & \frac{\gamma_{ae}}{\varphi_a} \\ \frac{v_c+v_{s3}}{\varphi_{aer}} & -\frac{v_c}{\varphi_{aer}} & 0 & 0 & 0 \\ 0 & 0 & -\frac{v_{cn}+v_{s3n}+\gamma_{ne}+v_{pn}}{\varphi_n} & \frac{v_{cn}}{\varphi_n} & \frac{\gamma_{ne}}{\varphi_n} \\ 0 & 0 & \frac{v_{cn}+v_{sn3}}{\varphi_{ner}} & -\frac{v_{cn}}{\varphi_{ner}} & 0 \\ \frac{\gamma_{ae}+v_p}{\varphi_e} & 0 & \frac{\gamma_{ne}+v_{pn}}{\varphi_e} & 0 & -\frac{(\gamma_{ae}+\gamma_{ne})}{\varphi_e} \end{bmatrix} \quad (3.78)$$

From linear algebra, a singular matrix has at least one eigenvalue that is zero. This affects the stability of the system; a linear system with a zero eigenvalue is stable but not asymptotically stable (attracting). Hence, in order for the system to be stable overall, the four remaining eigenvalues must be positioned so that each has negative real part.

The characteristic equation of (3.78) takes the form:

$$p_4(\lambda) = \lambda(\lambda^4 + a\lambda^3 + b\lambda^2 + c\lambda + d) = 0 \quad (3.79)$$

The four non-zero eigenvalues from equation (3.79) can be solved analytically; for quartic equations, Cardano and Ferrari established the analytical formula in the 16th century. However, this formula leads to a very bulky solution that does not help us determine system stability.

For the $\boldsymbol{J_{new}}$ matrix, the nullspace is given by the vectors satisfying:

$$\boldsymbol{c} = (c_1, c_2, c_3, c_4, c_5) \quad (3.80)$$

$$c_1 = t \quad (3.81)$$

$$c_2 = \left(1 + \frac{v_{s3}}{v_c}\right) t \quad (3.82)$$

$$c_3 = \frac{\gamma_{ne}}{\gamma_{ae}} \left(\frac{\gamma_{ae} + v_p}{\gamma_{ne} + v_{pn}}\right) t \quad (3.83)$$

$$c_4 = \frac{\gamma_{ne}}{\gamma_{ae}} \left(1 + \frac{v_{s3n}}{v_{cn}}\right) \left(\frac{\gamma_{ae} + v_p}{\gamma_{ne} + v_{pn}}\right) t \quad (3.84)$$

$$c_5 = \left(1 + \frac{v_p}{\gamma_{ae}}\right) t \quad (3.85)$$

Hence, for this underdetermined system, the steady-state equalities of the parameters that were determined in equations (3.73)-(3.76) only ensure that the ratios of the steady-state values match those of the Orlowski model.

The required steady-states are given by:

$$\boldsymbol{c_{required}} = (0.22266, 0, 0.74799, 0, 1.0328) \quad (3.86)$$

Since this set of steady-states is obtainable only from certain initial conditions, the model, as it is, is unrealistic. The next subsection sees a few modifications to the model to rectify these disadvantages.

3.4.3 Reduction to Four Compartments

The fact that the system represented by equations (3.65)-(3.69) is linearly dependent suggests that mass is conserved; there are no generation or loss terms, after all.

This suggests that there exists a *first integral* to the system, which we denote by $f(\boldsymbol{x})$. A first integral of a system, $\frac{d\boldsymbol{x}}{dt}$, exists if the first integral, $f\big(\boldsymbol{x}(t)\big)$, remains a constant for all times, t, of the solution, $\boldsymbol{x}(t)$.

For our system, with:

$$\boldsymbol{x}(t) = [C_a, C_{aer}, C_n, C_{ner}, C_e] \quad (3.87)$$

the first integral, $f\big(\boldsymbol{x}(t)\big)$, must satisfy:

$$\frac{df(\boldsymbol{x}(t))}{dt} = 0 \quad (3.88)$$

Hence, by the chain rule:

$$\frac{df}{dt} = \frac{df}{dC_a}\frac{dC_a}{dt} + \frac{df}{dC_{aer}}\frac{dC_{aer}}{dt} + \frac{df}{dC_n}\frac{dC_n}{dt} + \frac{df}{dC_{ner}}\frac{dC_{ner}}{dt} + \frac{df}{dC_e}\frac{dC_e}{dt} = 0 \quad (3.89)$$

Hence, a first integral for our system is given by:

$$f\big(\boldsymbol{x}(t)\big) = \varphi_a C_a + \varphi_{aer} C_{aer} + \varphi_n C_n + \varphi_{ner} C_{ner} + \varphi_e C_e \quad (3.90)$$

From the definition of linear dependence, the derivative of $f\big(\boldsymbol{x}(t)\big)$ is zero. Hence, we set $f(\boldsymbol{x}) = C_0$, where C_0 is a constant signifying the total concentration of calcium ions in all the compartments. Notice that conservative systems, or systems where a first integral exists, cannot have an attracting fixed point (we showed this in the previous section, as the system contained a zero eigenvalue). This observation then allows us to express one of the compartments in terms of the other four, reducing the ODE system to four coupled equations. We choose to replace the astrocytic ER compartment, since the Orlowski model provides dynamics for the astrocytic, neuronal and extracellular compartments. Hence:

$$C_{aer} = \frac{1}{\varphi_{aer}}(C_0 - \varphi_a C_a - \varphi_n C_n - \varphi_{ner} C_{ner} - \varphi_e C_e) \quad (3.91)$$

A simple check ensures that equation (3.66) still holds. Equation (3.65) then becomes:

$$\varphi_a \frac{dC_a}{dt} = v_c\left(\frac{1}{\varphi_{aer}}(C_0 - \varphi_a C_a - \varphi_n C_n - \varphi_{ner} C_{ner} - \varphi_e C_e) - C_a\right) - v_{s3} C_a - \gamma_{ae}(C_a - C_e) - v_p C_a$$

(3.92)

The other equations stay the same.

Equation (3.92) and (3.67)-(3.69) then form our new four-compartment system. Again, being linear, it can be expressed in matrix form:

$$\dot{\boldsymbol{x}} = \boldsymbol{J_{reduced}}\boldsymbol{x} \quad (3.93)$$

where

$$\boldsymbol{J_{reduced}} = \begin{bmatrix} -\frac{v_c\left(\frac{\varphi_a}{\varphi_{aer}}+1\right)+v_{s3}+\gamma_{ae}+v_p}{\varphi_a} & -\frac{v_c\,\varphi_n}{\varphi_a\varphi_{aer}} & -\frac{v_c\,\varphi_{ner}}{\varphi_a\varphi_{aer}} & \frac{-\frac{\varphi_e}{\varphi_{aer}}v_c+\gamma_{ae}}{\varphi_a} \\ 0 & -\frac{v_{cn}+v_{s3n}+\gamma_{ne}+v_{pn}}{\varphi_n} & \frac{v_{cn}}{\varphi_n} & \frac{\gamma_{ne}}{\varphi_n} \\ 0 & \frac{v_{cn}+v_{sn3}}{\varphi_{ner}} & -\frac{v_{cn}}{\varphi_{ner}} & 0 \\ \frac{\gamma_{ae}+v_p}{\varphi_e} & \frac{\gamma_{ne}+v_{pn}}{\varphi_e} & 0 & -\frac{(\gamma_{ae}+\gamma_{ne})}{\varphi_e} \end{bmatrix} \quad (3.94)$$

We note that, for non-zero parameter values, $J_{reduced}$ is now full-rank.

3.4.4 Bifurcation analysis

Although many bifurcations, such as the Hopf bifurcation, are not present in linear systems, nevertheless, we perform a bifurcation analysis here. In particular, we are interested in *transcritical bifurcations,* which arise when, when a certain parameter is increased or decreased past a critical value, the solution becomes unstable. This is helpful for us as it can rule out certain regions for a parameter search. Section 4.7 contains a more detailed introduction to bifurcation analysis, where we apply the method to another portion of the model; for now, we will discuss the findings of our analysis of this portion.

We find that a transcritical bifurcation exists for all four parameters that can be varied ($\gamma_{ae}, \gamma_{ne}, v_c, v_{cn}$); and these all occur when the parameter value is slightly less than 0 (specifically, at 10^{-6}). Hence, for the first three parameters, almost all negative values make the equilibrium lose stability. For v_{cn}, however, we notice that it is located 'extremely close to' a neutral saddle (not a bifurcation point *per se*), and this means that there is still a chance that we can approach the equilibrium along the stable manifold.

Hence, we can rule out, for three of the parameters, most negative regions and focus only on their positive values in the parameter search.

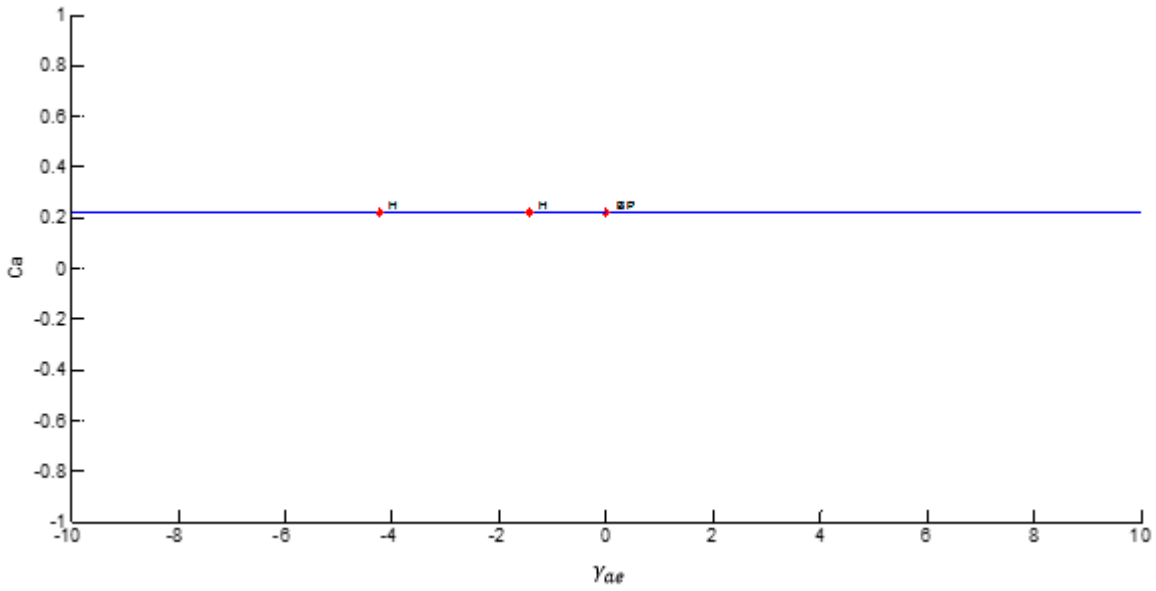

Figure 3.8: Bifurcation plot for γ_{ae}. H stands for a Hopf bifurcation, BP for break point, denoting a transcitical bifurcation.

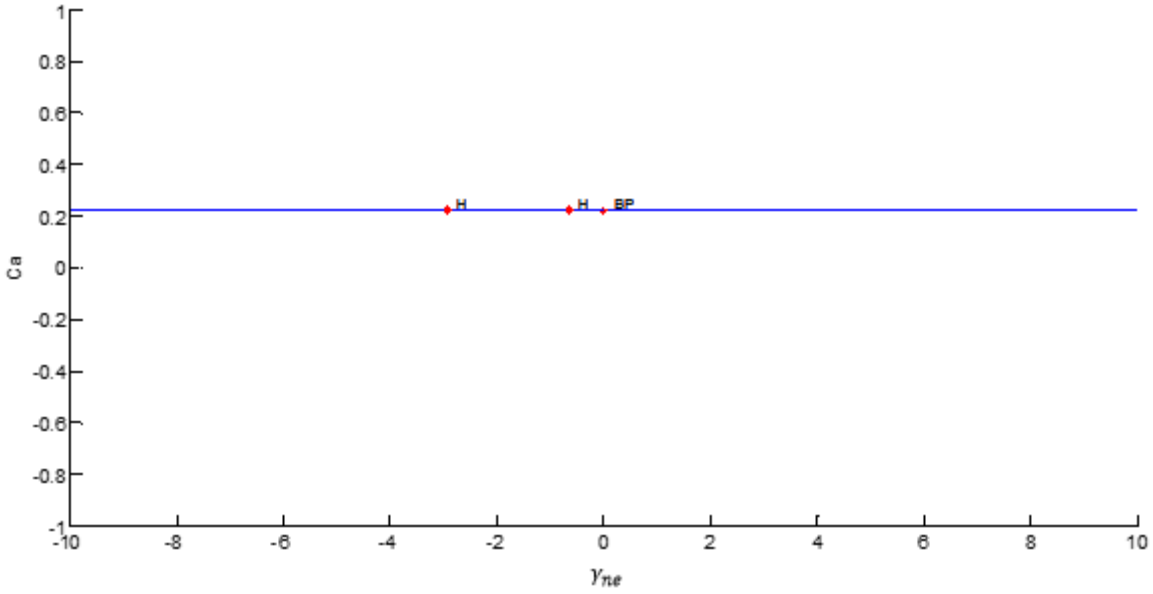

Figure 3.9: Bifurcation diagram for γ_{ne}. H stands for a Hopf bifurcation, BP for break point, denoting a transcitical bifurcation.

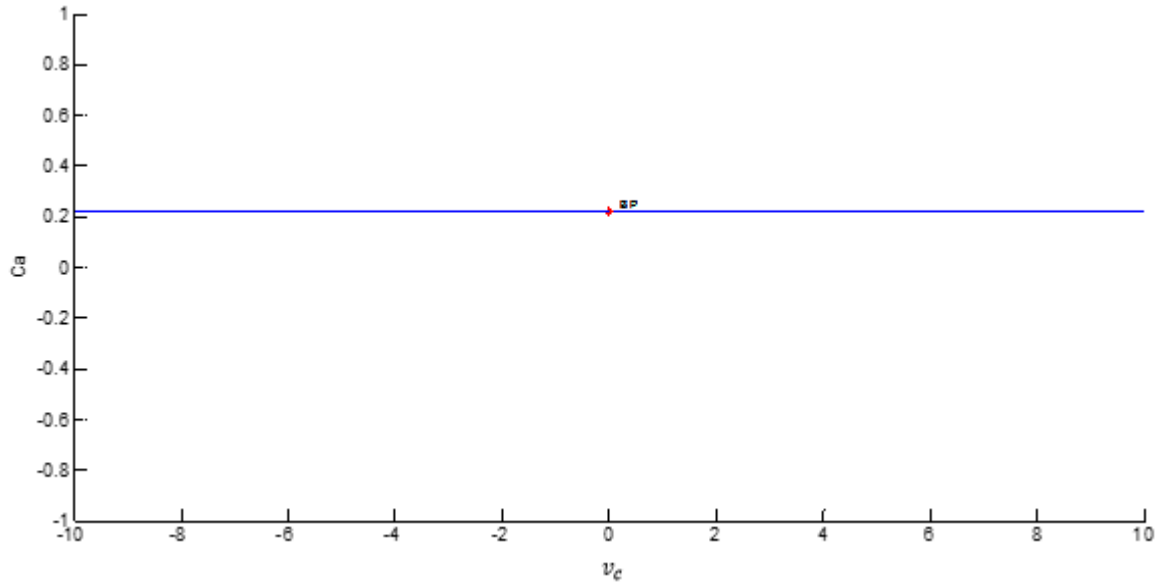

Figure 3.10: Bifurcation diagram for v_c. BP stands for break point, denoting a transcitical bifurcation.

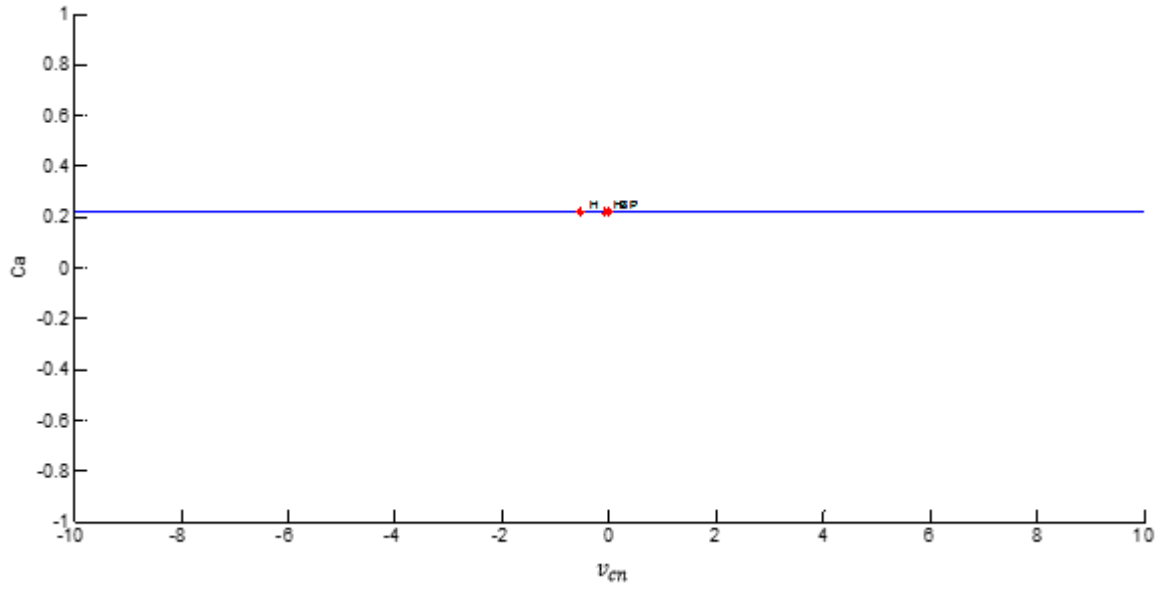

Figure 3.11: Bifurcation diagram for v_{cn}. H stands for a Hopf bifurcation, BP for break point, denoting a transcitical bifurcation.

3.4.5 Parameter Fitting

The parameter values of the model were obtained by matching the calcium dynamics to simulations of the calcium dynamics in the model of Orlowski *et al.* at CBF decreases from 75% to 95%, representing strokes at differing severities. The four unknown parameter values were determined,

for each decrease in CBF, using a nonlinear least-squares approach: specifically, we used the *lsqnonlin* function in MATLAB. Since, from the bifurcation analysis, all four parameter values must be positive for model stability, a trust-region-reflective algorithm was used to incorporate these parameter bounds.

Having obtained four parameter values for each CBF reduction, we expressed each of these parameters as a function of CBF. We chose this function to be smooth and also as simple as possible.

We obtain the following relations:

$\gamma_{ae} = 2.38 \times 10^{-4}$ /(mM s) (3.95)

$\gamma_{ne} = 9.80 \times 10^{-5}$ /(mM s) (3.96)

$v_c = 3.643 \times 10^{-5} \exp\left(-\left(\frac{CBF-75}{2.768}\right)^2\right)$ /(mM s) (3.97)

$v_{cn} = 2.85 \times 10^{-6}\, CBF - 1.02 \times 10^{-4}$ /(mM s) (3.98)

Note that the expression for v_{cn} could equally well be taken as a constant, given the variability in the results. The parameter values for different CBF decreases are summarised in Table 3.2 and shown graphically in Figures 3.12-3.15.

CBF Reduction (%)	γ_{ae}	γ_{ne}	v_c	v_{cn}
95	2.38×10^{-4}	9.80×10^{-5}	7.73×10^{-28}	1.69×10^{-4}
90	2.38×10^{-4}	9.80×10^{-5}	6.42×10^{-18}	1.55×10^{-4}
85	2.38×10^{-4}	9.80×10^{-5}	7.82×10^{-11}	1.40×10^{-4}
80	2.38×10^{-4}	9.80×10^{-5}	1.39×10^{-6}	1.26×10^{-4}
75	2.38×10^{-4}	9.80×10^{-5}	3.643×10^{-5}	1.12×10^{-4}

Table 3.2: The parameter values for the four parameters of the calcium model at different CBF values.

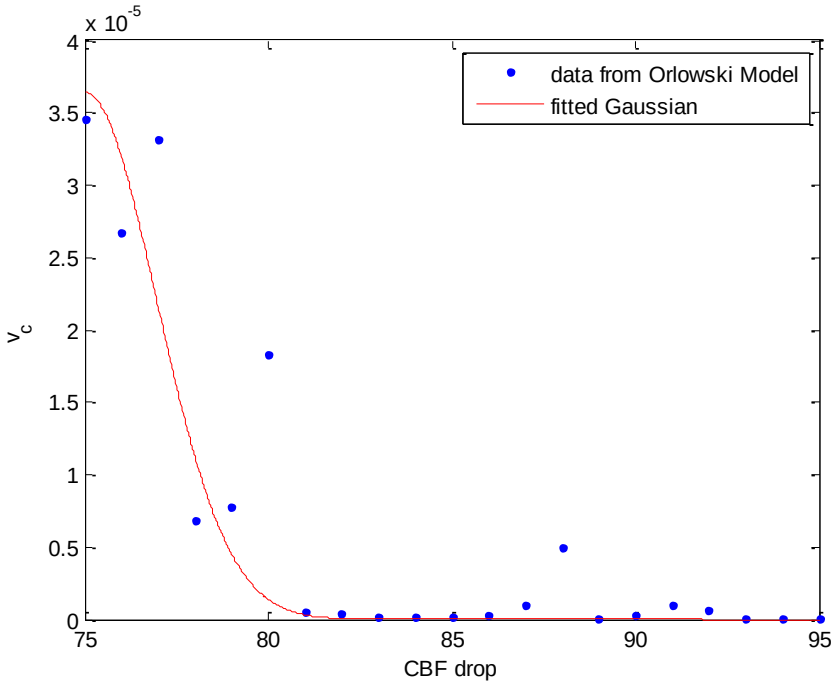

Figure 3.12: Best fit of v_c using a Gaussian function.

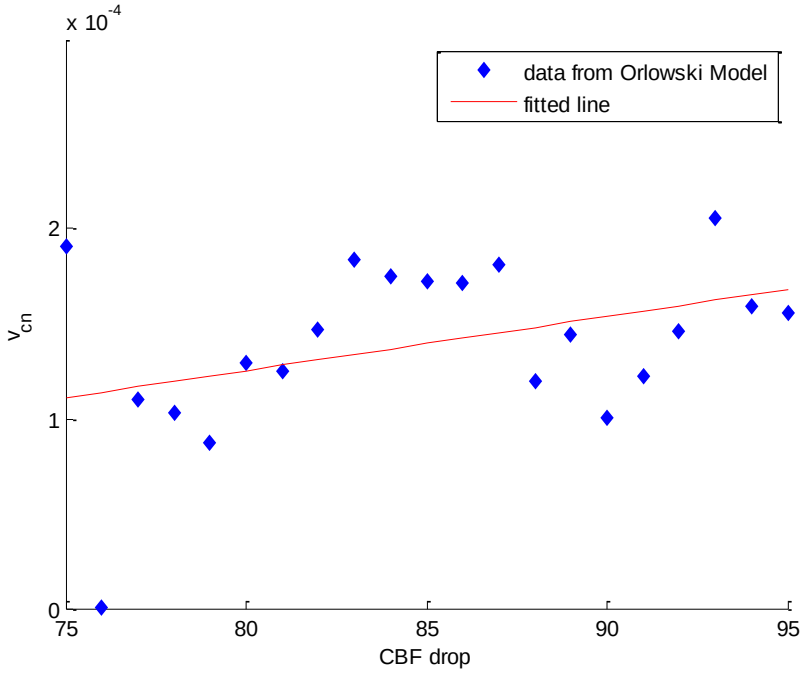

Figure 3.13: Best fit of v_{cn}, with a linear function.

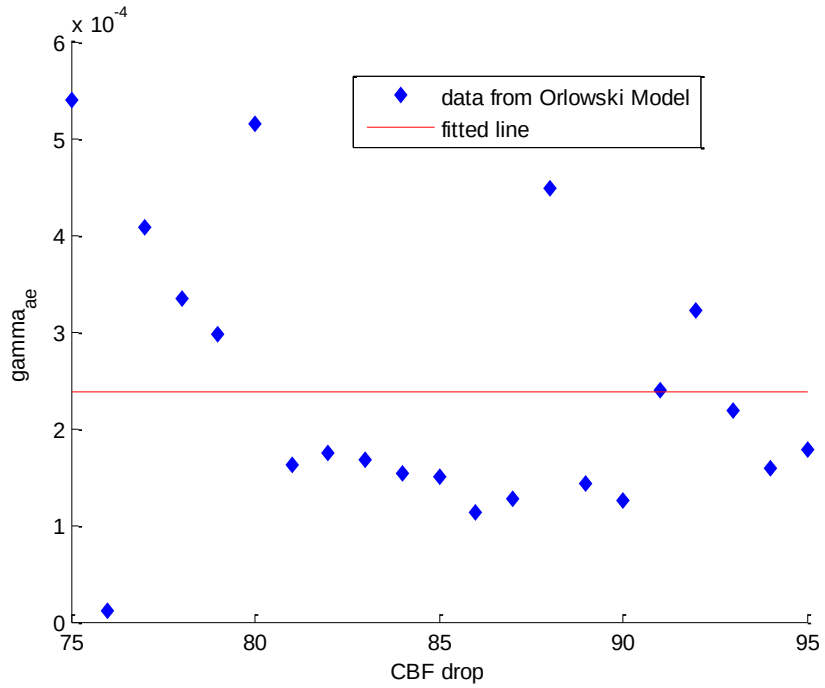

Figure 3.14: Best fit of γ_{ae}

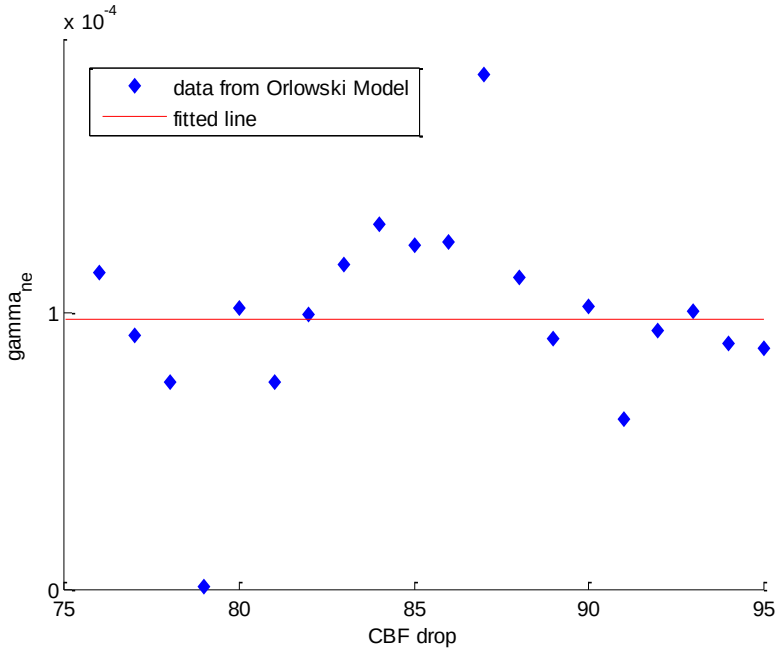

Figure 3.15: Best fit of γ_{ne}

Figures 3.12-3.15 shows these four parameters plotted as functions of CBF, together with the individual fits, at each CBF value, to the data points generated from the Orlowski model. These

functions generate parameter values that give acceptable fits at each CBF drop, based on visual inspection.

3.4.6 Graphs of Fitted Responses of Proposed Model

To verify that the best fits of the parameters (Section 3.2.5) are suitable, we simulate the calcium model with these parameter values, in the absence of spatial variations. Figures 3.16 shows plots of the 95% case. Although there are clear differences between the fitted and Orlowski model responses, the fits do manage to portray many qualitative effects of the Orlowski model, such as the overshoot observed for larger CBF decreases.

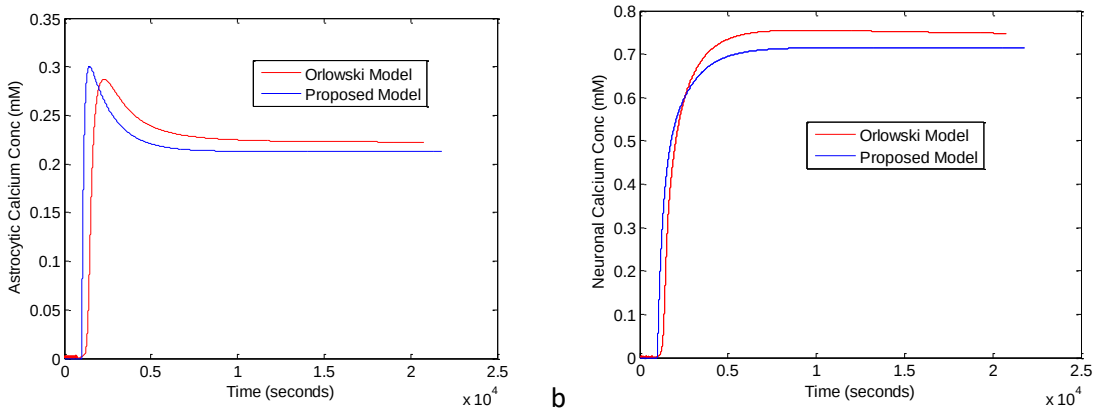

c

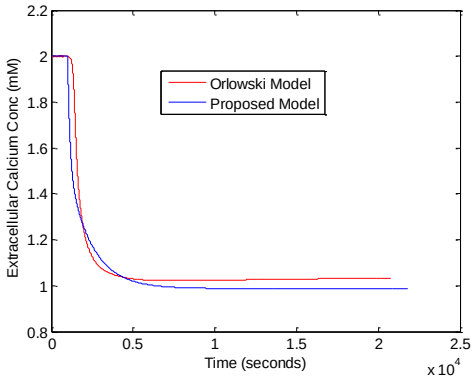

Figure 3.16: Graphs comparing calcium dynamics predicted by the Orlowski Model (red) and our model (blue) at 95% CBF drop, in the a) astrocytic, b) neuronal and c) extracellular compartments.

3.5 Conclusions

This chapter looks at a model for the mass transport of calcium ions across the brain. We propose an initial model and discuss the changes required to make it realistic. Having made these changes, we then find appropriate parameter values.

The advantages of the model are that the equations are based on the concept of mass transport as well as biological concepts of calcium transport. In addition, we have strived, where possible, to simplify the model. For instance, we simplify many terms in Lavrentovich and Hemkin's model so that all the terms are linear. We then ensure model stability by selecting parameters sensibly.

The disadvantages are, firstly, the difficulty in determining best fit curves of the four parameters. Figures 3.12-3.15 show what a hard task this is. Furthermore, the fact that we use synthetic data as the blueprint for the fitting can also be validly questioned. Finally, we will see in Chapter 5 that the model does not allow for spatial inhomogeneities, a necessary requirement for modelling ischemic stroke.

In the next chapter, we will investigate a model that describes cell injury and death, before Chapter 5 couples the calcium and cell death models together to give us a model that uses calcium dynamics to predict cell death.

Chapter 4: Cell Death Model

And this is why I sojourn here,
Alone and palely loitering,
Though the sedge is withered from the lake,
And no birds sing.
'La Belle Dame Sans Merci', John Keats

4.1 Introduction

Section 2.3 described some of the mathematical models of calcium dynamics during ischaemic stroke found in the literature and also what other variables are required in the model. Each of these models has desirable features but limitations as well. Perhaps the ideal model, from our perspective, is one whose schematic is shown in Figure 4.1. This model should have a clinically measureable input, such as cerebral blood flow (CBF), include intracellular calcium dynamics and a 'counter' quantifying the damage done to cells in a region and an output stating the fate of these cells. Although there are other measures that are of clinical interest, such as oxygen consumption, this thesis focuses on CBF as the only model input. CBF can be accurately measured using MRI scans on ischaemic individuals, making it a practical choice. CBF can drop to as low as 20-25 ml/100 g/minute from its standard flow rate of 60-80 ml/100g/min. Decreasing CBF further to only 10-20ml/100g/min results in the formation of the ischemic penumbra [82].

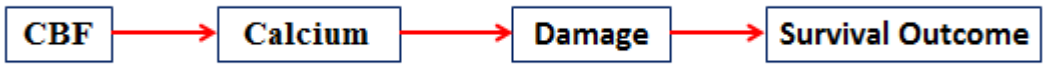

Figure 4.1: A schematic of our ideal mathematical model of stroke.

Hereafter is an explanation of the new model, which is an extension of the one found in DeGracia *et al.*, [7], and also draws inspiration from the paper by O'Neill *et al*. [8]. The schematic in Figure 4.2 shows the interactions in this model. After a stroke occurs, different cells are injured at varying degrees

of *Injury* (*I*), which is assumed to depend on the cell's intracellular calcium concentration. Each cell is then in one of three states: the *Alive* (*A*) state, the *Vulnerable* (*V*) state or the *Necrotised* (*N*) state. This is based on the tri-state model by O'Neill *et al.*. A cell in the Alive state is healthy and can still perform normal biological functions, while Necrotised cells have perished due to either necrosis or apoptosis (the precise mechanism is not important in this model yet, since the only concern is whether or not the cell dies at this stage).

4.2 From Calcium to Survival/Apoptosis: A New Mathematical Model

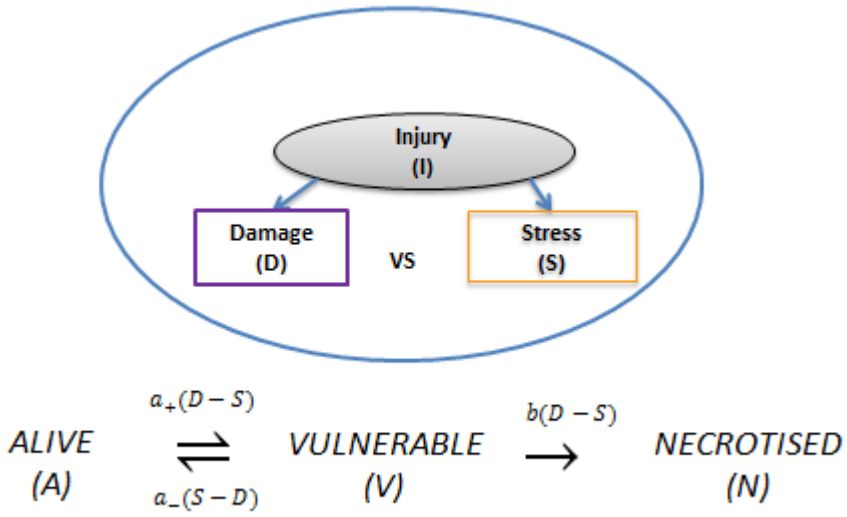

Figure 4.2: Schematic of our model of cell injury and death.

However, it is the Vulnerable cells that are most interesting in this work; these are able to either slip into the Necrotised state, or be rescued as Alive cells. Biologically, these can be thought to represent cells in the region of the penumbra, which can be saved with treatment. The rate at which these cells switch states is assumed to be governed by the variables *Damage* (*D*) and *Stress* (*S*). The biological meanings for these two variables are explained in Section 2.3.3.

In rate equation form, our model so far can then be written as:

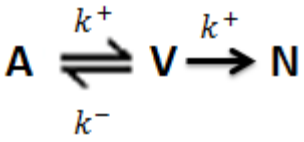

(4.1)

This set of reactions can be expressed by ordinary differential equations, specifically Equations 4.2 - 4.4 below:

$$\frac{dA}{dt} = -H[D-S](D-S)A + H[S-D](S-D)V \quad (4.2)$$

$$\frac{dV}{dt} = H[D-S]\big((D-S)A - (D-S)V\big) - H[S-D](S-D)V \quad (4.3)$$

$$\frac{dN}{dt} = H[D-S](D-S)V \quad (4.4)$$

where $H[x]$ represents the Heaviside step function, which is defined as:

$$H[x] = 1, \qquad x \geq 0$$

$$= 0, \qquad x < 0 \quad (4.5)$$

Thus, the set of rate reactions can be interpreted as follows: there are two modes. If the total Damage factors (D) exceed the Stress factors (S), then the Alive cells (A) are assumed to progress to the Vulnerable (V) state, while Vulnerable cells (V) also progress to the Necrotised state (N) at a rate proportional to the difference between the Damage and Stress factors. If, however, the Stress factors (S) exceed the Damage (D), then none of the above reactions occur. Instead, the system moves towards a recovering stage and no cells perish; this provides a chance for Vulnerable cells (V) to recover to the Alive (A) state and they are assumed to do this at a rate equal to the difference between the Stress (S) and Damage (D) factors. D and S are defined in a similar manner as in DeGracia's model, explained in Section 2.3.3 , and are both functions of Injury (I):

$$\frac{dD}{dt} = \frac{1}{\tau}\left(\frac{\left(c_D I exp(\lambda_D I)\right)^4}{\left(c_D I exp(\lambda_D I)\right)^4 + S^4} - D\right) \quad (4.6)$$

$$\frac{dS}{dt} = \frac{1}{\tau}\left(\frac{\left(c_S I exp(-\lambda_S I)\right)^4}{\left(c_S I exp(-\lambda_S I)\right)^4 + D^4} - S\right) \quad (4.7)$$

Note that equations 4.6 and 4.7 include a time constant, τ, an addition to DeGracia's equations. This is to allow for nondimensionalisation and also us to determine the timescale of the system response (around 100 seconds for a spreading stroke). Thus, the reactions can be seen to develop over real time, rather than over an arbitrary time scale. c_D, c_S, λ_D and λ_S are parameters whose values are given later in Table 4.

Notice that, at this point, there is no spatial dependence: it is still, like DeGracia's model, in 0-dimensional space. This will be developed in the following sections, adding calcium propagation across the brain.

4.3 Diffusion-Reaction Equation for Calcium Propagation

In order to model calcium propagation across the brain cells, spatial coordinates must be added to the model: in others words, the equations should now be dependent on both time and space, making our model a set of PDEs.

Adding this spatial dimension allows us to supplement the diffusion of calcium from the cells affected by ischemic stroke. As explained in Section 2.2.4.1, a calcium cascade triggers the cell's transition to the Necrotised state. However, the magnitude of initial injury, I, is linked to the calcium concentration [34], [43] and so, instead of adding another variable to the model to represent calcium concentration, one can assume that calcium concentration is directly proportional to the Injury. Thus, as a first approximation, the Injury variable could also be thought of as being analogous to the amount of calcium ions that have diffused to each particular region of the brain. The PDE for I takes the form of a diffusion-reaction equation, using spherical coordinates and assuming spherical symmetry:

$$\frac{\partial I}{\partial t} = \frac{\alpha}{r^2}\frac{\partial}{\partial r}\left(r^2\frac{\partial I}{\partial r}\right) - \beta \tanh\left(\frac{I}{I_0}\right) + \gamma I(I_0 - I) \quad (4.8)$$

Following the work of Chapuisat *et al*. (34), adding two terms to the diffusion equation results in a *diffusion-reaction* equation, as follows: first, the term $-\beta\, tanh\left(\frac{I}{I_0}\right)$ represents the rate at which calcium ions are being flushed out of the system due to homeostatic measures [83], depending on both the calcium concentration at the initiation of stroke (I_0) and the current calcium concentration, I.

The term $\gamma I(I_0 - I)$ represents the addition of calcium ions due to ionic currents at the cell membrane and from calcium pumps [83]. This takes the form of a logistic function, where the rate of change is zero at $I = 0$ and $I = I_0$. Notice that $I = 0$ is still a stationary point of the equation, as expected.

This model completes the link from calcium to cell death, as depicted in Figure 4.3. It ignores the different compartments found in the Orlowski model; instead, the whole space is considered as a single isotropic medium, as a first approximation. When we couple this model to the cell death model in Chapter 3, we will be able to portray a more ideal model of ischaemic stroke (see Figure 4.1).

Figure 4.3: Schematic of Calcium/Damage model is shown here.

4.4 Numerical Implementation

The mathematical model requires one initial and two boundary conditions. The initial condition simulates a stroke by assuming a core volume of injured tissue. The ideal initial condition to simulate this is a function that is constant for a very short distance radially, from the centre of the stroke, and zero further out (no effects of stroke).

One possible function is the Heaviside. Beyond a critical radial distance, k, the function takes a value of one (this represents the region damaged by stroke), while at distances less than k, the function is zero (no effects of stroke). However, this is not a smooth function and, hence, encounters difficulties

during the numerical integration. As an alternative, the following is a function that resembles the Heaviside but is still sufficiently smooth: specifically, at $t = 0$:

$$I(r, t = 0) = 1 - 0.5\, tanh\left(\frac{r-k}{2}\right) \quad (4.9)$$

where, r is the radial distance from the centre of the stroke, while k is a fixed point usually halfway between the centre and the outer boundary of the sphere. This shifts the *tanh* function to the right, so that the value of Injury is 1 at $r = k$ but trails away at regions further away. Hence, this equation for the initial condition gives a smooth function that is still similar to the step function.

The two boundary conditions for this PDE are as follows:

1. The flux of I at the centre of the spherical region (i.e. at $r = 0$) is zero (mathematically, $\frac{\partial I}{\partial r} = 0$ at $r = 0$).
2. At the boundary of a sufficiently large sphere, the flux of calcium into/out of the sphere is zero (mathematically, $\frac{\partial I}{\partial r} = 0$ at $r \to \infty$), as suggested by Schiesser and Griffith [84].

An alternative for the second boundary condition is to specify that, at infinite radius, the value of I tends to zero; or, practically, that the mesh-point furthest from the centre of the stroke should be close enough to zero that it can be approximated as such (mathematically, $I \to 0$ as $r \to \infty$).

The boundary conditions for all the remaining variables are: first, there is no radial flux at the centre and, second, at infinity, the radial flux of every variable is zero.

4.5 Model Discretisation

The model comprises of a set of partial differential equations. The *Method of Lines* is a technique that can solve these numerically. The idea here is to semi-discretise the equations by discretising in the spatial dimension, leaving a set of ODEs. These can then be solved using in-built MATLAB functions. The discretisation in space is performed using a 5-point finite difference scheme. Using the Taylor

expansion for each of the 5 points and finding a linear combination that eliminates as many terms that are not the first derivative as possible, results in the following centred finite difference scheme:

$$\frac{1}{12}\left(f(x_{-2}) - 8f(x_{-1}) + 8f(x_1) - f(x_2)\right) = f'(x_0) + O(\varepsilon^4) \quad (4.10)$$

This 5-point scheme, based upon the discretised first derivatives, can be used to obtain the second derivative. The code used for the centred difference scheme is largely based on that of Schiesser and Griffith [84] and Hamdi *et al.* [85].

Having presented this model, the next section focuses on two analytical techniques that help to identify the unknown parameters and qualify the different behaviours that the system presents: namely nondimensionalisation and bifurcation analysis.

4.6 Nondimensionalisation

Nondimensionalisation is a technique used to reduce the number of parameters in a model, as well as to provide insights into the scales involved in these parameters. To obtain the nondimensionalised model, we substitute the variables I, t, α, β and γ with their non-dimensionalised forms, as follows:

$$I^* = \frac{I}{I_0}, \quad t^* = \frac{t}{\tau}, \quad r^* = \frac{r}{R}, \quad \alpha^* = \frac{\tau\alpha}{I_0}, \quad \beta^* = \frac{\tau\beta}{I_0}, \quad \gamma^* = \frac{\tau\gamma}{I_0}$$

Notice that the variables A, V and N are already nondimensional.

From the literature [86], the diffusion coefficient for calcium in the neuron, α, takes values from 2×10^{-3} to 6×10^{-3} m²/s. Also, $I_0 = 10$, from DeGracia's work [7], with a value of 10 being the maximum magnitude of Injury inflicted upon the cell in the DeGracia model; here, we restrict Injury values so that they take values between 0 and 1, while $\tau = 100$ seconds, representing a typical timescale for spreading of stroke and $R = 1mm$, a typical lengthscale. Hence, it turns out that: $\alpha^* = 0.01$, which fixes one parameter. Values can also be determined for I^*, t^* and r^* in this way.

What is required, then, is to find appropriate values for β^* and γ^*. The term $\beta^* \tanh(I^*)$ represents the flushing out of calcium ions to provide balance to the diffusion effects. Thus, since the hyperbolic tangent function has a maximum value of 1, the value of β^* should be of the same order of magnitude as that of α^*.

Parameter	Value
$\boldsymbol{\tau}$	$\mathbf{100}$
$\mathbf{c_D}$	$\mathbf{0.1}$
$\mathbf{c_S}$	$\mathbf{20}$
$\boldsymbol{\lambda_D}$	$\mathbf{0.1}$
$\boldsymbol{\lambda_S}$	$\mathbf{0.9}$
$\mathbf{I_0}$	$\mathbf{10}$

Table 4.1: Table of parameter values for the variables in our model originating from the model by DeGracia *et al.* [7].

Parameter	Value(s)
$\boldsymbol{\alpha^*}$	$\mathbf{10^{-2}}$
$\boldsymbol{\beta^*}$	$\mathbf{2 \times 10^{-2}}$

Table 4.2: Table of non-dimensionalised values, found by nondimensionalisation, of two of the three parameters involved in the reaction-diffusion equation added to DeGracia's model; γ^* remains to be determined.

The nondimensionalised model equations are:

$$\frac{\partial D}{\partial t^*} = \frac{\left(c_D I_0 I^* exp(\lambda_D I_0 I^*)\right)^4}{\left(c_D I_0 I^* exp(\lambda_D I_0 I^*)\right)^4 + S^4} - D \quad (4.11)$$

$$\frac{\partial I^*}{\partial t^*} = \alpha^* \frac{1}{r^2}\frac{\partial}{\partial r}\left(r^2 \frac{\partial I^*}{\partial r}\right) - \beta^* \tanh(I^*) + \gamma^* I^*(1 - I^*) \quad (4.12)$$

$$\frac{\partial S}{\partial t^*} = \frac{\left(c_S I_0 I^* exp(-\lambda_S I_0 I^*)\right)^4}{\left(c_S I_0 I^* exp(-\lambda_S I_0 I^*)\right)^4 + D^4} - S \quad (4.13)$$

These are coupled to equations 4.1-4.3 in their nondimensionalised form. The parameter values used in this model are given in Tables 4.1 and 4.2.

We also conducted a sensitivity analysis on this model to see how the varying the parameters, especially the unknowns (α^*, β^* and γ^*), affects the output variance. Taking the values of the parameters given in Tables 4.1 and 4.2, as well as $\gamma^* = 0.39$, for reasons we elaborate on in Section 4.7, we conduct a sensitivity analysis using the Morris Method. This is a popular method that considers the change in model output when each of the n model parameters is varied at several randomly selected regions in parameter space.

Specifically, each time the *i*th parameter, say X_i, is increased from some base value by a small increment, Δ, say, we record its *elementary effect,* which is defined as the difference between the model output, $f(X_i)$, calculated at the two parameter values:

$$EE_i = \frac{f(X_1, X_2 \dots X_i + \Delta, \dots X_n) - f(X_1, X_2 \dots X_i, \dots X_n)}{\Delta} \quad (4.14)$$

The elementary effect of each parameter is then calculated m times at different locations in parameter space; the book by Saltelli *et al.* contains an algorithm that optimises these locations [87], which we implement to find the sensitivities. For the *i*th parameter, the Morris Method gives two measures of sensitivity: μ_i^*, the average of the absolute values of its elementary effects and σ_i, the standard deviation of these elementary effects. These are written, mathematically, as follows:

$$\mu_i^* = \frac{1}{m}\sum_{j=1}^{m}\left|EE_{i,j}\right| \quad (4.15)$$

$$\sigma_i = \frac{1}{m-1}\sum_{j=1}^{m}\left(EE_{i,j} - \mu_i\right)^2 \quad (4.16)$$

where:

$$\mu_i = \frac{\sum_{k=1}^{r} EE_i^k}{r} \quad (4.17)$$

Larger values of μ_i^* indicate that the *i*th parameter affects the model output more than a factor with a lower μ_i^*, while higher σ_i values suggest that the parameter is involved with interactions with itself or other parameters in a nonlinear manner; a low σ_i, by contrast, indicates a linear, additive parameter.

Since the Morris Method works on ODEs rather than PDEs, we will reduce equations 4.11-4.13 to ODEs by removing the spatially varying term $\alpha^* \frac{1}{r^2}\frac{\partial}{\partial r}\left(r^2 \frac{\partial I^*}{\partial r}\right)$. Hence, this sensitivity analysis will not include the effects on the parameter α^*. After we solve the resultant equations numerically, we can then use the Morris Method at each time point, recording the values of μ^* and σ for each parameter as a function of time. Each of the three dependent variables of equations 4.11-4.13 – namely, D, I^* and S – serves as the model output and so we can plot graphs showing how μ^* and σ for each parameter changes over the simulation time course. This we see in Figure 4.4, where we show only the plots for μ^* and σ in relation to two state variables: D and S. This is because these two variables control the ultimate fate of the cell (we recall that $D > S$ for cell death to occur), whereas the critical value of I^* required to trigger cell death is parameter dependent. Indeed, from DeGracia's paper, we know that this critical value, I_x^*, is given by:

$$I_x^* = \frac{\ln(c_S) - \ln(c_D)}{\lambda_S + \lambda_D} \quad (4.18)$$

Turning our attention back to Figure 4.4, in particular panels a and b, we conclude that all parameters experience a hike in sensitivity at around 10-30 units of time – an understandable phenomenon mirroring the model simulations, which we will inspect later. The most sensitive parameters are λ_S and λ_D and, again, we would expect this given equation 4.18, where they influence the denominator of I_x^*, the Injury threshold value without being constrained by the logarithmic function, as c_S and c_D are. The parameters β^* and γ^* play smaller though not insignificant roles in the output variability of both D and S, which gives some reassurance that our chosen parameter values are sensible. The variability of β^* does play a larger role in the sensitivity of I^*, as would be expected from Equation 4.12, though we have not shown the plot here.

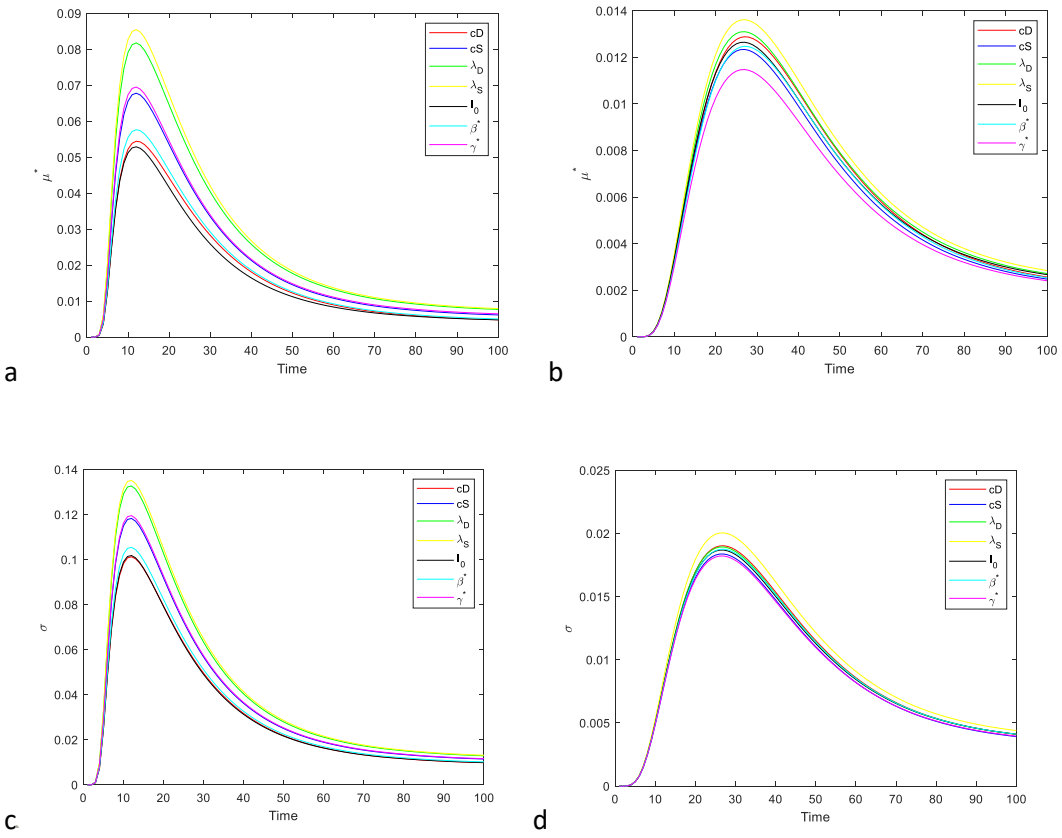

Figure 4.4: Sensitivity analysis showing how the model variance is affected by variability in the parameters in Equations 4.11-4.13, using the Morris Method. Panel a shows the mean of absolute elementary effects when the output variable in consideration is D, caused by the parameters, while panel b shows the mean of elementary effects for output variable S. Panel c shows the standard deviation of the elementary effects for output variable D, while panel d displays the standard deviation for output variable S.

4.7 Bifurcation Analysis

In this subsection, the focus is to conduct a bifurcation analysis of equations 4.6-4.7, i.e. an analysis of DeGracia's model. A bifurcation point is a specific parameter value where changing the value further causes a change in either the stability of the equilibrium point of an ODE, or causes the equilibria to change. There are computer programmes such as MATCONT and AUTO which plot bifurcation diagrams of ODEs and which are freely available. MATCONT, which is a toolbox that serves as an add-on to MATLAB, is used in this analysis [88].

A bifurcation analysis allows one to understand what the effects of changing values of the so-far undetermined parameter in the model, γ^*, have on qualitative model behaviour. To do this, we first examine the work of DeGracia *et al.* [7], where bifurcation diagrams are created by varying the injury parameter, I. With the parameter values in Tables 4.1 and 4.2, a bifurcation diagram of the DeGracia

model, with I being the varying parameter, was created using MATCONT, since the authors do not perform this explicitly for the set of parameters that we choose.

Before discussing the results, a particular type of bifurcation, known as a *saddle-node* bifurcation, or *blue-sky* bifurcation, should be explained. This bifurcation occurs when, by increasing or decreasing a parameter value, two equilibria collide, before they both disappear when the parameter is further increased or decreased. A more detailed analysis is given in many textbooks on dynamical systems, such as that by Strogatz, [89]. In biological systems, the occurrence of a pair of saddle-node bifurcations is common and causes hysteresis.

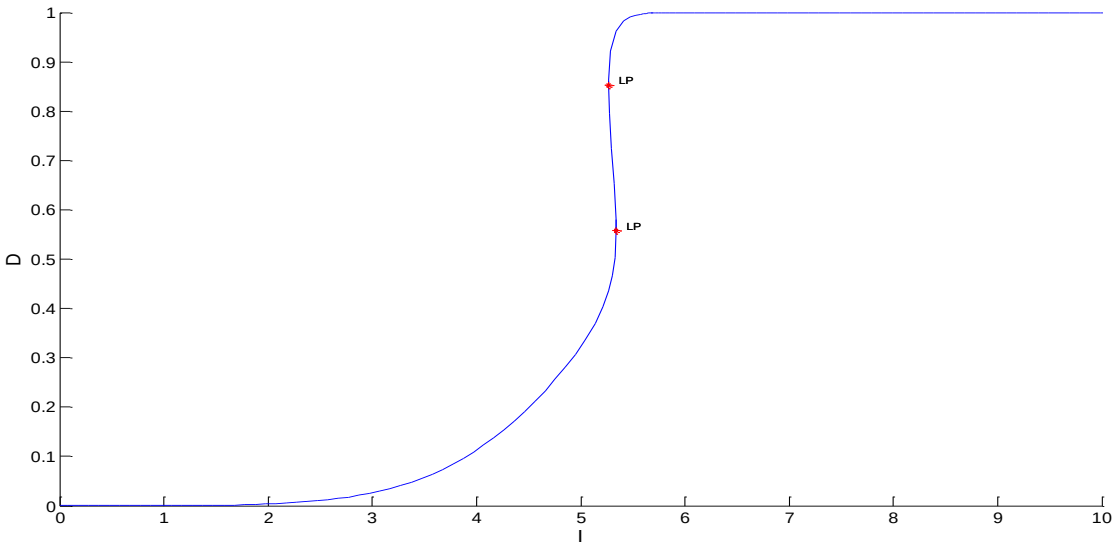

Figure 4.5: Bifurcation diagram showing how Damage (D) varies with magnitude of Injury (I). The two points labelled 'LP' denote limit points; specifically, saddle-node bifurcations, the region between which the solutions are unstable.

MATCONT produces the bifurcation diagram shown in Figure 4.5; after increasing the Injury parameter from an initial value of zero, a limit point or, more precisely, a saddle-node bifurcation, is reached at $I = 5.337$, after which the Damage jumps suddenly to a value of 1. Coming backwards from an Injury value of 10, there exists another saddle-node bifurcation at $I = 5.268$, after which

decreasing the injury more will cause the Damage to jump discontinuously to lower levels. Thus, these parameter values produce the hysteresis behaviour expected from the model.

4.8 Simulation Results

MATLAB simulations of the AVN/SD model using the parameters in Tables 4.1 and 4.2 are displayed in Figures 4.6 and 4.7. As can be seen in Figure 4.6, for $\gamma^* = 0.39$, beyond a radial distance of 0.5, the Injury value is too low to be able to drive many of the Alive cells (Figure 4.6d) into the Vulnerable state (Figure 4.6e). We choose this value of γ^* because this is just below the bifurcation threshold; this γ^*corresponds to a steady-state Injury value, I, of 0.53 (Figure 4.6c), just below the injury threshold, $I_{threshold} = 0.5337$, and hence the Damage is low at steady-state (Figure 4.6a), while the Stress response is high (Figure 4.6b). This Injury value is important, as will be shown later.

Closer to the centre, a small percentage (approximately 20%) of the cells die, shown in Figure 4.6f. For smaller values of γ^*, the percentage of dead cells decreases even further. However, after increasing γ^* above this critical value, a sudden change occurs.

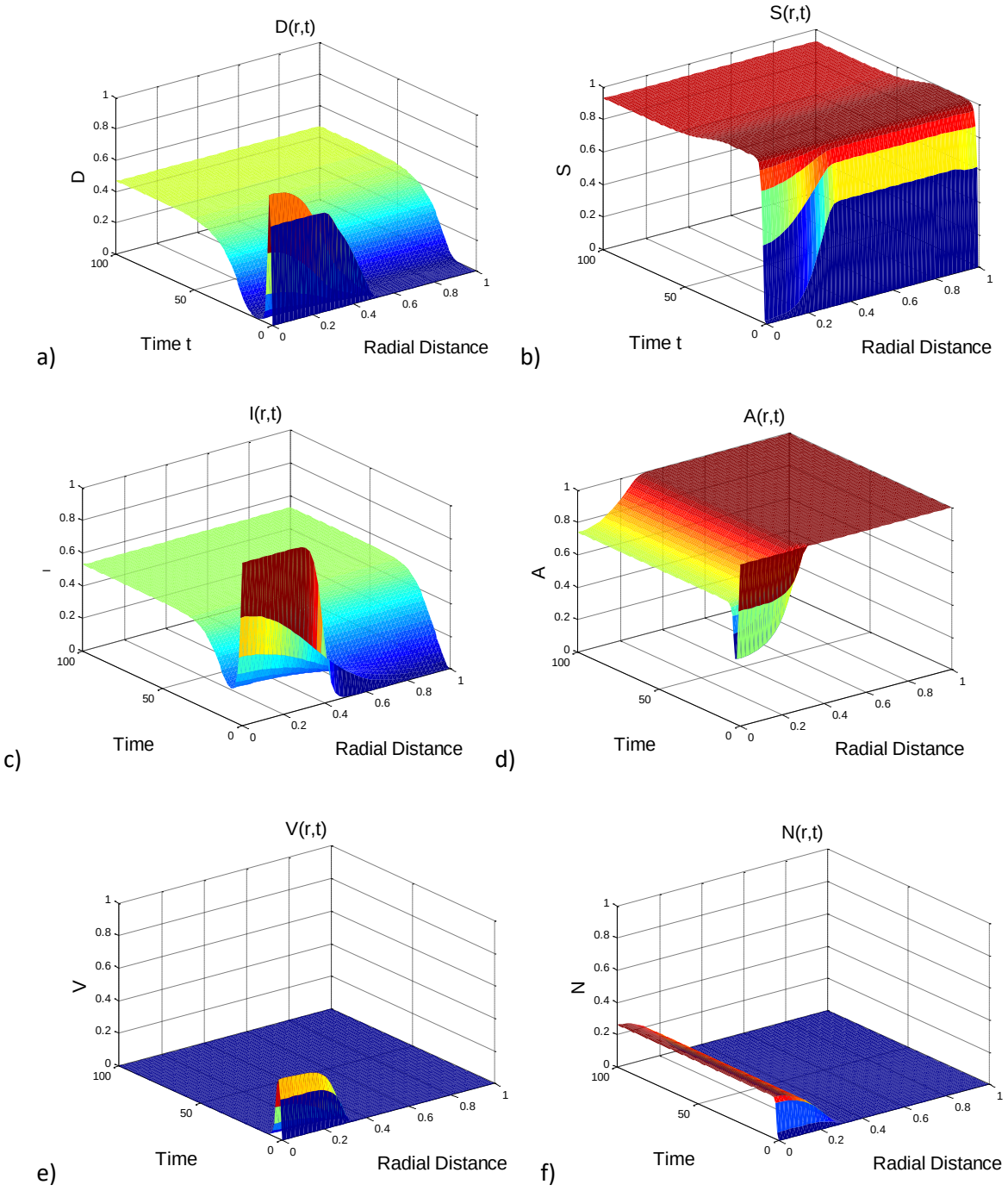

Figure 4.6: These plots show the dynamics of a) Damage, b) Stress, c) Injury and the d) Alive, e) Vulnerable and f) Necrosis if the value of γ is 0.39.

Now, all cells are predicted to die. In Figure 4.7a, the Damage decreases at first, but then increases to 1, the maximum value. In Figure 4.7b, on the other hand, the Stress increases at first but then falls to $\mathbf{0.3}$. In Figure 4.7c, the Injury at steady-state settles at a value of $\mathbf{0.544}$. In Figure 4.7d, the Alive cells throughout the sphere fall to 0 at steady state, as do the Vulnerable cells in Figure 4.7e; there is only a small period of time around $\boldsymbol{t = 50}$ seconds where the Vulnerable cell population is non-zero.

As expected, the proportion of dead cells subsequently rises to $\mathbf{1}$. The reason for these dynamics is that $\boldsymbol{I}$ now crosses the bifurcation value of $\mathbf{0.5337}$ (see Figure 4.5) and hence the Damage ($\boldsymbol{D}$) incurred is close to maximal; all the cells are predicted to die.

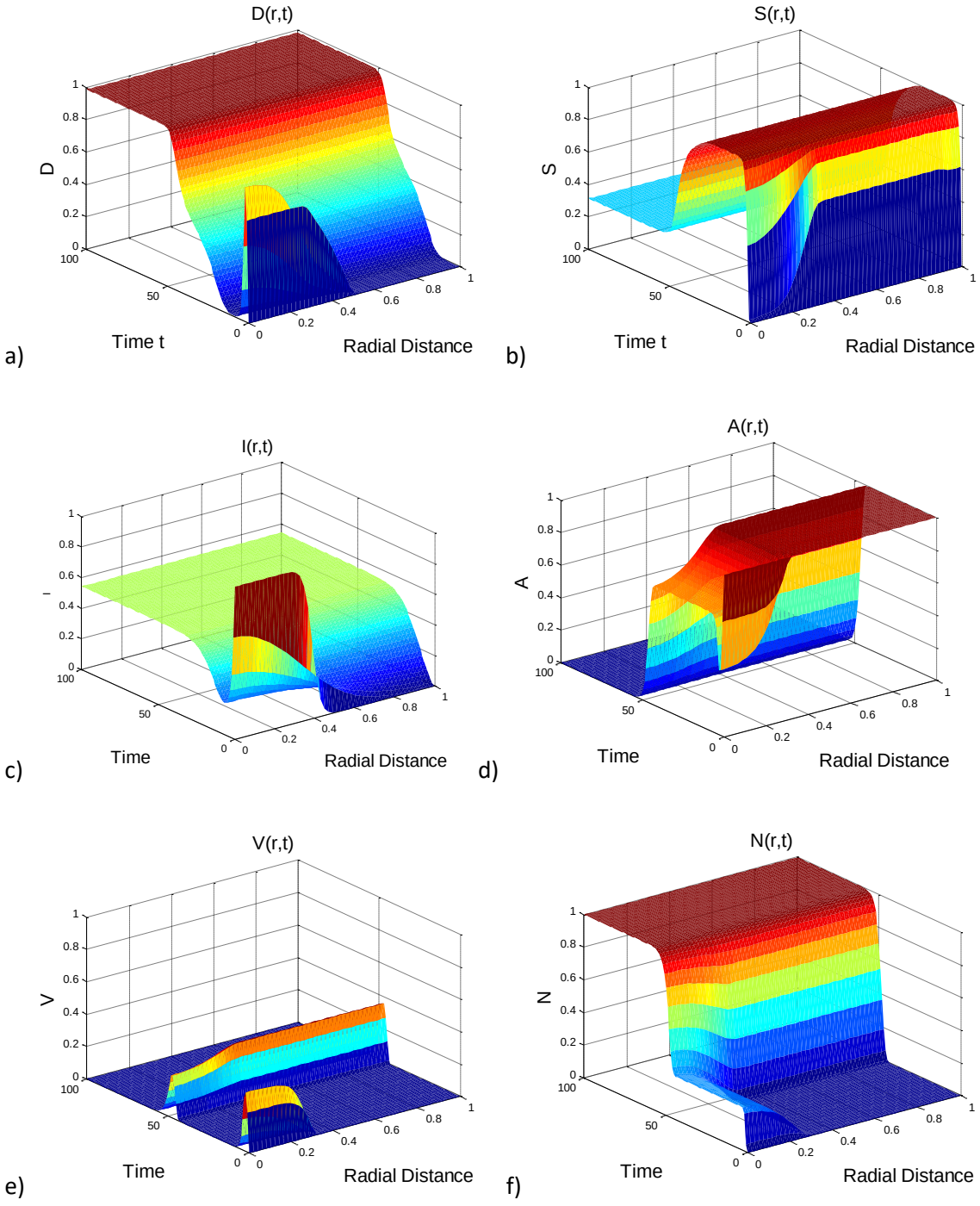

Figure 4.7: These plots show the dynamics of a) Damage, b) Stress, c) Injury and the d) Alive, e) Vulnerable and f) Necrosis if the value of γ is increased to 0.40.

There is no continuous increase of the proportion of dead cells. In a way, this is unrealistic (the cells far away from the centre should not also die) and so some change to the model is necessary. However, the concept that, at some critical injury value, the number of dead cells suddenly increases non-continuously is a particularly interesting aspect of the behaviour of the model.

The reason for this sudden increase in dead cells is as follows: as mentioned in Section 4.7, when we increase the injury value from zero, at a certain value, namely 0.5337, (the non-dimensionalised value), a saddle-node bifurcation is encountered. The Damage incurred will then be maximal and, hence, all cells die.

This is precisely what is happening in the case where $\gamma^* = 0.40$ (further simulations show that a more precise value for this switching effect is $\gamma^* = 0.391$). After the calcium ions have diffused or, mathematically, I has reached its steady-state value, each model equation effectively becomes an ODE for each spatial element; these ODEs all have the same steady-state I value. Moreover, that value is just above the critical value for the saddle-node bifurcation. Hence, using the bifurcation diagram in Figure 4.5, one can conclude that the cells must all perish. Line plots showing the difference between these two values of γ^* are given in Figure 4.8.

Hence, we can conclude that the value of γ^* is kept below 0.391 in a healthy brain but rises above this critical point during a stroke. Knowing also the appropriate parameters for α^* and β^*, we can then simulate the model for two situations: first, when the cell dies and second, when it survives a stroke. This cell death model alone, however, does not allow us to observe regions dying after steady-state has been reached. Hence, as seen in Figure 4.6f, there may be spatial inhomogeneities but these form at the very beginning of the stroke, due to the initial system perturbations. However, we know that vulnerable cells die after sufficiently long time without reperfusion. In addition, as soon as the critical value of γ^* is reached, all cells across the entire domain are predicted to die. Clearly this is unrealistic and so we must find a way to address these points. The work in Chapter 5, where we investigate spatial instabilities in a calcium and cell death model is a step in this direction.

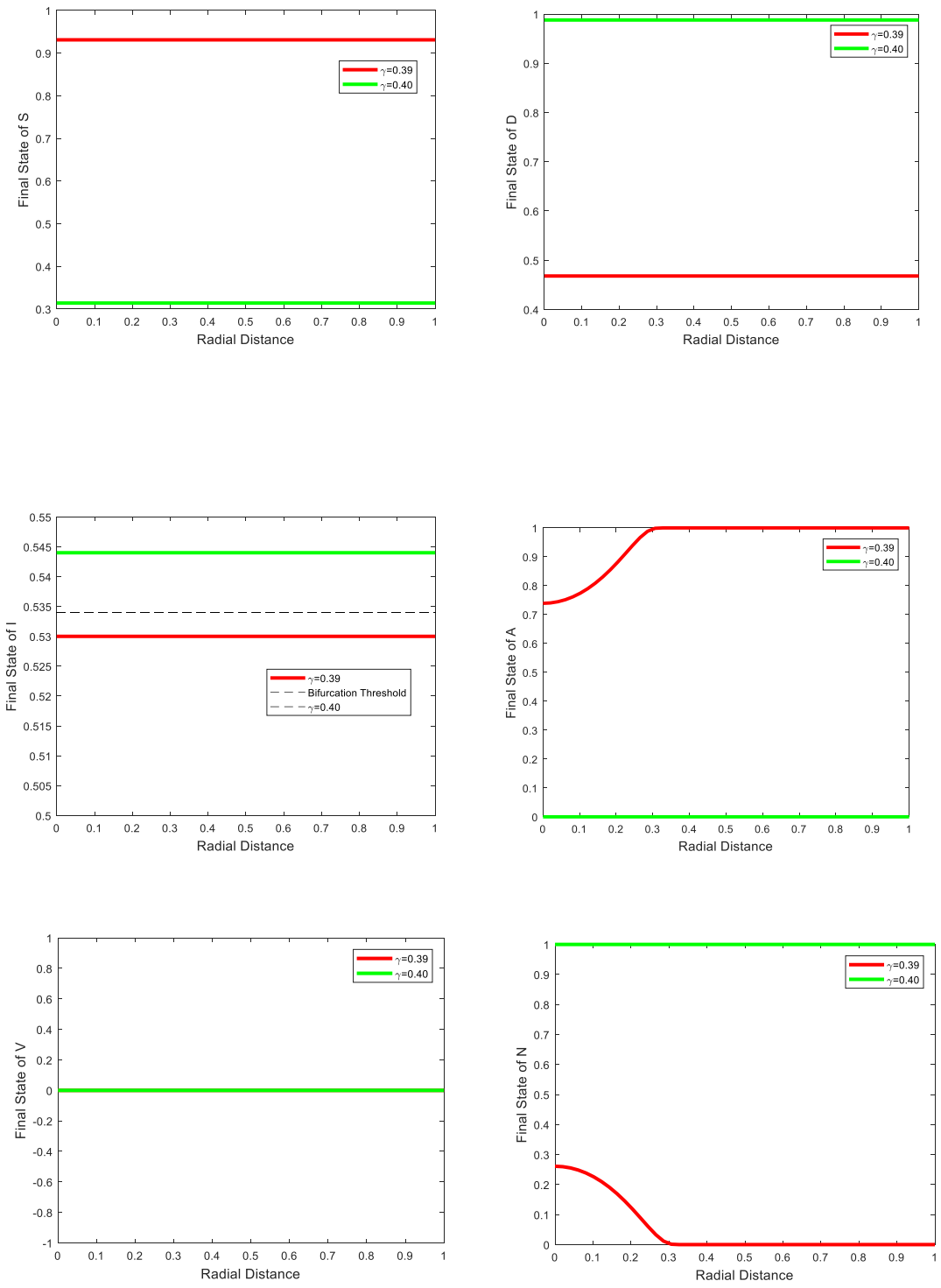

Figure 4.8: Line plots showing the final state of the model when $\gamma = 0.39$ (red) and $\gamma = 0.4$ (green).

4.6 Conclusions

This chapter discusses our cell death model. We combine two concepts: DeGracia's model, in which cell Injury is the resultant sum of all effects that damage and heal the cell, and O'Neill's tri-state model where the state of the cell flips between Alive and Vulnerable, before going on to be Necrotised if it does not receive treatment. This gives us a model that is simple, though highly nonlinear. There is a clear threshold value above which the damage done to the brain is irreparable and this is an aspect of the model we will exploit in Chapter 5. There, we must overcome the limitations of the model (that spatial inhomogeneities are either formed only at the beginning of the ischaemia event or not at all). If, however, we can ensure that some phenomenon guarantees the presence of spatial inhomogeneities after the model reaches steady-state, then we can set parameters so that the steady-state values sit just below the critical value for necrosis and allow the resultant spatial instabilities to take effect. The presence of Turing patterns, as will be discussed in Chapter 5, will, thus, allow this model to be more realistic.

Chapter 5

Beauty is Truth; Truth Beauty - that is all

Ye know on Earth and all ye need to know,

'Ode on a Grecian Urn', John Keats, 1820

In Chapters 3 and 4, we introduced different parts of the model: calcium dynamics (Chapter 3), damage/injury and eventual cell fate (Chapter 4). This chapter pieces together these model components to give us a set of equations that describes the development of a stroke after CBF reduction. However, simply coupling these components together does not necessarily lead to a model showing the qualitative effects we are interested in. Specifically, in most diffusion-reaction models, the diffusion term has a spatially homogenising effect, where the steady-state values of each variable remains the same across the entire domain. In our model, this would mean that the fractions of living and dead cells are the same at every region in the brain.

We know, however, that stroke results in the formation of different regions (such as the core and penumbra) and, therefore, that equilibria which are homogeneous across the brain cannot represent what is observed in reality. In the face of this problem, we look to Turing's work on instabilities resulting from reaction-diffusion equations [72], introduced in Section 2.3. First, we adapt the model so that Turing inhomogeneities can occur (Section 5.1), then find its Turing space (Section 5.1.1), before observing the dispersion relation of the chosen parameters (Section 5.2). We also give a short proof of why our model cannot include advection if we wish to see Turing instabilities (Section 5.2.2).The chapter concludes with simulations of the model, both with and without feedback, in Section 5.3.

5.1 Two-Compartment Model

A realistic mathematical model of ischaemic stroke should display Turing instabilities. As we saw in Section 2.3, this requires both certain terms to be present in the diffusion-reaction equations, and parameter values to fall within the Turing space. If we inspect the two diffusion-reaction equations from our model (see Sections 3.2 and 4.6), we see that they are currently:

$$\left(\frac{\partial C_e}{\partial t} + U_e.\nabla(C_e)\right) = D.\nabla^2(\varphi_e C_e) + \gamma_{ae}(C_a - C_e) + \gamma_{ne}(C_n - C_e) + v_p C_a + v_{pn} C_n \quad (5.1)$$

$$\frac{\partial I}{\partial t} = \alpha.\nabla^2 I - \beta \tanh\left(\frac{I}{I_0}\right) - k_a(C_a - C_{a0})(C_a - C_{a1}) - k_n(C_n - C_{n0})(C_n - C_{n1}) + \eta(I - I^2) \quad (5.2)$$

Immediately noticeable is the fact that since neither equation contains any cooperative terms (see Table 2.2), the model cannot display Turing instabilities. This, together with some calculations that we describe briefly below, suggests that other effects must happen that we have not modelled. To incorporate these extra effects, we compare a few basic models in the literature known to show this phenomenon (see Section 2.3), and select the one that most closely matches our model (Equations 5.1-5.2). This turns out to be the Schnakenburg model [77], which we have introduced in Section 2.3.2.3. The equations of the model with coefficients in front of all terms (*c.f.* equations 2.39-2.40) are:

$$\frac{\partial C_e}{\partial t} = D_1\nabla^2 C_e + a_1 - a_2 C_e + a_3 C_e{}^2 I \quad (5.3)$$

$$\frac{\partial I}{\partial t} = D_2\nabla^2 I + b_1 - a_3 C_e^2 I \quad (5.4)$$

We also define: $D = \frac{D_2}{D_1}$, the ratio of diffusion coefficients.

Here, a_1 corresponds to the terms from equation 5.1 that are independent of C_e, a_2 to those with C_e dependence and b_1 to terms in equation 5.2 without I dependence. As noted previously, no cooperative term exists in equations 5.1-5.2 and, thus, addition of the $a_3 C_e^2 I$ terms is one way to

rectify this. A further consequence of having this term in equation 5.4 ($-a_3 C_e^2 I$) is that, as it represents negative feedback, restricting the increase of I when the injury takes higher values, we now no longer need the corresponding term in equation 5.2, namely $-\eta I^2$. However, as shown by the terms f_1 and f_2 in Table 5.2, adding this term alone is not sufficient; we still cannot satisfy all four conditions (equations 2.29-2.32) necessary for the appearance of Turing instabilities without further adjusting parameter values.

To this end, we now conduct a short proof, by seeing how the parameter values in equations 5.3-5.4 may be chosen to satisfy, first, the required steady-state for C_e and I and, second, the four conditions given by equations 2.29-2.32. We will show, for illustration, the case where CBF reduction is 85%.

5.1.1 Turing Space for the Modified Schnakenburg Model

Finding a model's Turing Space is important, as it allows us to ascertain the range of parameters within which Turing instabilities occur – all the parameter values where the model is physiologically feasible. Since the model represented by equations (5.3) and (5.4) is slightly different to what Schnakenburg proposed in [77], (there are now coefficients in front of all the reaction terms), we must repeat the steps in the paper by Murray, [78]. We define throughout the subscript notation f_x to mean the first partial derivative, $\frac{\partial f}{\partial x}$.

We rename the reaction terms in equations 5.3-5.4 as f and g, where:

$$f(C_e, I) = a_1 - a_2 C_e + a_3 C_e^2 I \quad (5.5)$$

$$g(C_e, I) = b_1 - a_3 C_e^2 I \quad (5.6)$$

Hence:

$$f_{Ce} = -a_2 + 2a_3 C_e I \quad (5.7)$$

$$f_I = a_3 C_e^2 \quad (5.8)$$

$g_{Ce} = -2a_3 C_e I$ (5.9)

$g_I = -a_3 C_e^2$ (5.10)

Subsequently, the four conditions required for Turing instabilities to occur in a two-species model impose the following restrictions:

Condition 1: $(f_{Ce} + g_I)|_{(\overline{Ce},\bar{I})} < 0$ (5.11)

This leads to the following inequality:

$(-a_2 + 2a_3 C_e I - a_3 C_e^2)|_{(\overline{Ce},\bar{I})}$

$= \left(-a_2 - a_3 C_e (2C_e - I)\right)|_{(\overline{Ce},\bar{I})} < 0$ (5.12)

Since $\overline{C_e} > \bar{I} > 0$, this condition is always satisfied.

Condition 2: $(f_{Ce} g_I - f_I g_{Ce})|_{(\overline{Ce},\bar{I})} > 0$ (5.13)

This leads to:

$a_2 a_3 C_e^2|_{(\overline{Ce},\bar{I})} > 0$ (5.14)

We will see in Section 5.2.1 that a_2 is constrained by the parameters γ_{ae} and γ_{ne}. Hence, this condition is guaranteed when $a_3 > 0$.

The next two conditions are dependent on D.

Condition 3: $(D f_{Ce} + g_I)|_{(\overline{Ce},\bar{I})} > 0$ (5.15)

For equations 5.5-5.10, this leads to the following:

$(D(2a_3 C_e I - a_2) - a_3 C_e^2)|_{(\overline{Ce},\bar{I})} > 0$ (5.16)

Condition 4: $((D f_{Ce} - g_I)^2 + 4D f_I g_{Ce})|_{(\overline{Ce},\bar{I})} > 0$ (5.17)

Hence, we require:

$$(D(-a_2 + 2a_3C_eI) + a_3C_e^2)^2 - (4Da_3C_e^2)(2a_3C_eI))|_{(\overline{Ce},\bar{I})}$$

$$= ((D(-a_2 + 2a_3C_eI) + a_3C_e^2)^2 - 8Da_3^2C_e^3I)|_{(\overline{Ce},\bar{I})} > 0 \quad (5.18)$$

We now impose the equilibria constraints forced upon us by setting equations (5.5) and (5.6) to zero and setting variables to their steady-state values:

$$\overline{C_e} = \frac{a_1+b_1}{a_2} \quad (5.19)$$

$$\bar{I} = \frac{b_1}{a_3\overline{C_e}^2} \quad (5.20)$$

In Section 5.2.1, we will see that the parameter a_2 is fixed. If, for now, we can accept this to be true, then equation 5.19 has only one 'free' variable; let that be a_1. Both b_1 and a_3 (in equation 5.20) can then be represented in terms of a_1 (and the other fixed parameters/equilibria).

$$b_1 = a_2\overline{C_e} - a_1 \quad (5.21)$$

$$a_3 = \frac{a_2}{\bar{I}} - \frac{a_1}{\bar{I}\,\overline{C_e}} \quad (5.22)$$

Hence, each of conditions expressed by equations 2.29-2.32 can be written in terms of a_1 and D alone. Due to their length, these are given in the Appendix. However, this means that we can plot the regions where each condition is met. The intersection of all these regions thus reveals the Turing space for our model. Note that we already know that condition 1 is satisfied for all a_1 and D.

The region where a_1 satisfies Condition 2 (equation 5.14), being independent of D, can be seen in Figure 5.1. This shows that the relevant region is:

$$a_1 < 4.4 \times 10^{-4} \quad (5.23)$$

The final two conditions (equations 5.16 and 5.18) are dependent on both a_1 and D, since they indicate when the system becomes unstable due to diffusion-driven effects. We choose to investigate this by looking at certain values of D and finding the range of a_1 that satisfy both conditions.

Figure 5.2, for instance, shows that when $D = 1000$, $a_1 < 2.2 \times 10^{-4}$ is the region satisfying Condition 3, while the union between $a_1 < 2.1 \times 10^{-4}$ and $a_1 > 2.3 \times 10^{-4}$ satisfies Condition 4. Hence, the intersection of these regions is $a_1 < 2.1 \times 10^{-4}$ and this is the Turing Space for $D = 1000$. Further simulations also show that, as D increases above 1000, the feasible region for Condition 4 increases until all positive values of a_1 are incorporated satisfy the condition. However, the feasible region for Condition 3 remains almost exactly the same ($a_1 < 2.2 \times 10^{-4}$) and so this condition becomes the limiting factor at higher values of D.

	$\boldsymbol{D}$	$\boldsymbol{a_1}$
Condition 1	Any value of D	Any positive a_1
Condition 2	Any value of D	$a_1 < 4.4 \times 10^{-4}$
Condition 3	$D = 15$ (critical value)	$a_1 < 2.0 \times 10^{-4}$
	$D = 100$	$a_1 < 2.2 \times 10^{-4}$
	$D = 1000$	$a_1 < 2.2 \times 10^{-4}$
	$D \gg 1000$	$a_1 < 2.2 \times 10^{-4}$
Condition 4	$D = 15$	No positive a_1
	$D = 100$	$a_1 < 1.6 \times 10^{-4}$ or $a_1 > 2.6 \times 10^{-4}$
	$D = 1000$	$a_1 < 2.1 \times 10^{-4}$ or $a_1 > 2.3 \times 10^{-4}$
	$D \gg 1000$	All positive a_1

Table 5.1: Summary of parameter values required to satisfy each condition represented by equations 5.12, 5.14, 5.16 and 5.18. The intersection of all these regions denotes the Turing Space of the model for that value of D.

On the other hand, if we decrease D, the region satisfying Condition 4 begins to shrink. As an example, if we take $D = 100$, then the Turing Space is now $a_1 < 1.6 \times 10^{-4}$, and it is the fourth condition that is responsible for this region being smaller. As can be seen from Figure 5.3, the region satisfying this condition has shrunk, whereas that satisfying Condition 3 has not. This trend of a shrinking feasible region for Condition 4 as the value of D decreases continues until the critical value $D = 15$ is reached. At this value, the left part of the feasible region no longer exists (see Figure 5.4). The right side, moreover, is so far away from the region satisfying Condition 3 (which sees practically no change) that, by taking the intersection of the two regions again, we conclude that the Turing Space vanishes for values of D less than or equal to this critical value. It is worth repeating that, overall, we notice that the feasible region for Condition 3 stays at around $a_1 < 2 \times 10^{-3}$, but that the region for Condition 4 is subject to greater variations at lower D values. Hence, we find that lower values of D result in smaller regions of a_1 where both conditions 3 and 4 are satisfied. This is consistent with the findings given in the literature [70], [78].

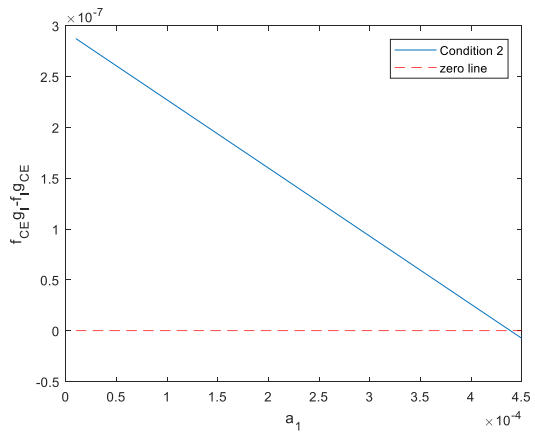

Figure 5.1: Plot of Condition 2 as parameter a_1 changes. To satisfy this condition, $a_1 < 4.4 \times 10^{-4}$.

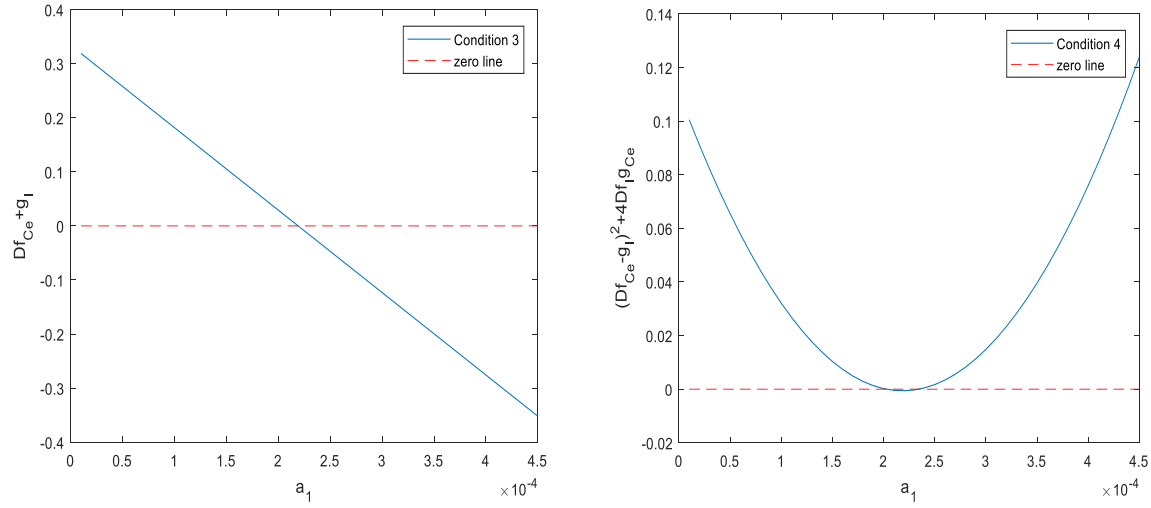

Figure 5.2: The regions of a_1 satisfying condition 3 (left) and 4 (right) when $D = 1000$. The blue curves demarcate where each condition is equivalent to zero, while the red line is at zero. Regions above the red line but below the blue curves indicate feasible regions for each condition.

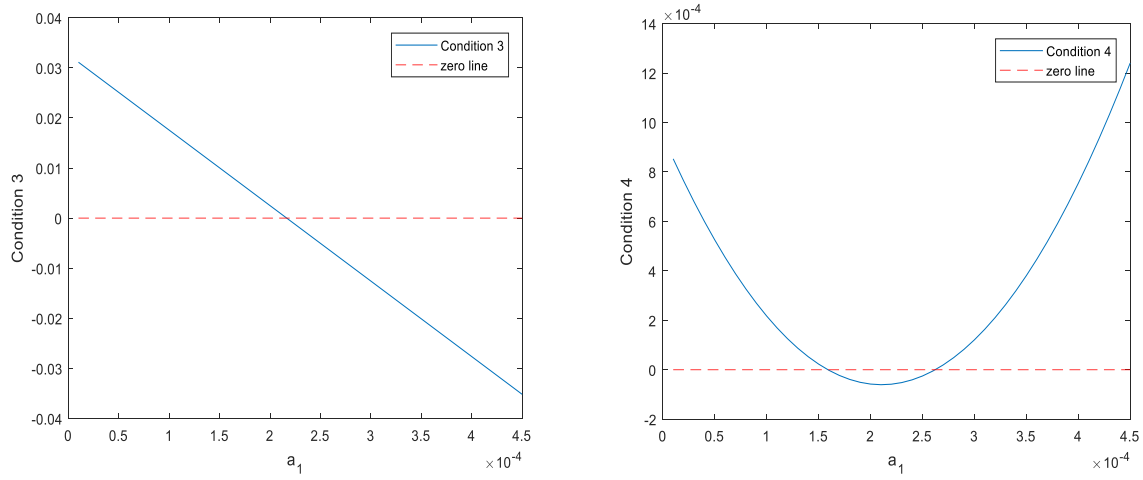

Figure 5.3: The regions of a_1 satisfying condition 3 (left) and 4 (right) when $D = 100$. The blue curves demarcate where each condition is equivalent to zero, while the red line is at zero. Regions above the red line but below the blue curves indicate feasible regions for each condition.

.

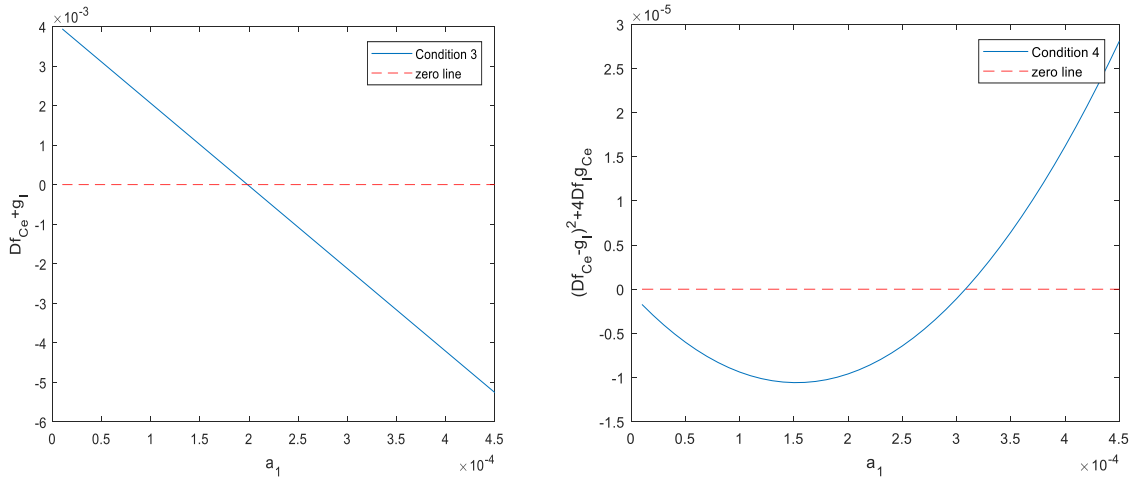

Figure 5.4: The regions of a_1 satisfying condition 3 (left) and 4 (right) when $D = 15$. The blue curves demarcate where each condition is equivalent to zero, while the red line is at zero. Regions above the red line but below the blue curves indicate feasible regions for each condition.

5.2 The fifth condition: Instabilities in the presence of boundary conditions

While satisfying equations 5.10-5.13 is a necessary step for finding Turing instabilities [70], models with boundary conditions present one more condition that we must fulfil. As we saw in Section 2.3.1, this extra condition arises from the need to bound our domain (in our case, by having no-flux conditions at the boundaries). Remembering that the solutions to equations 5.3-5.4 are exponential functions, no-flux boundary conditions restrict the form of these exponentials to cosine functions in space. Hence, only a discrete number of cosine waves can be packed into any domain and the aim of the fifth condition is to determine which *modes* are admissible [70].

By plotting the dispersion plots of the model with several values of a_1 and D that lie within the Turing space, we observe that it is not possible to entirely isolate one mode (see Figure 5.5, where we show the dispersion plots of three different values of D). Instead, there must coexist either a few modes of higher order (> 9), or a large range of both lower (≈ 3) and higher order modes. Modes of higher order will produce instabilities of lower amplitude across the same domain than lower order modes. However, if lower and higher order modes are both present, the former are prone to interact with the latter.

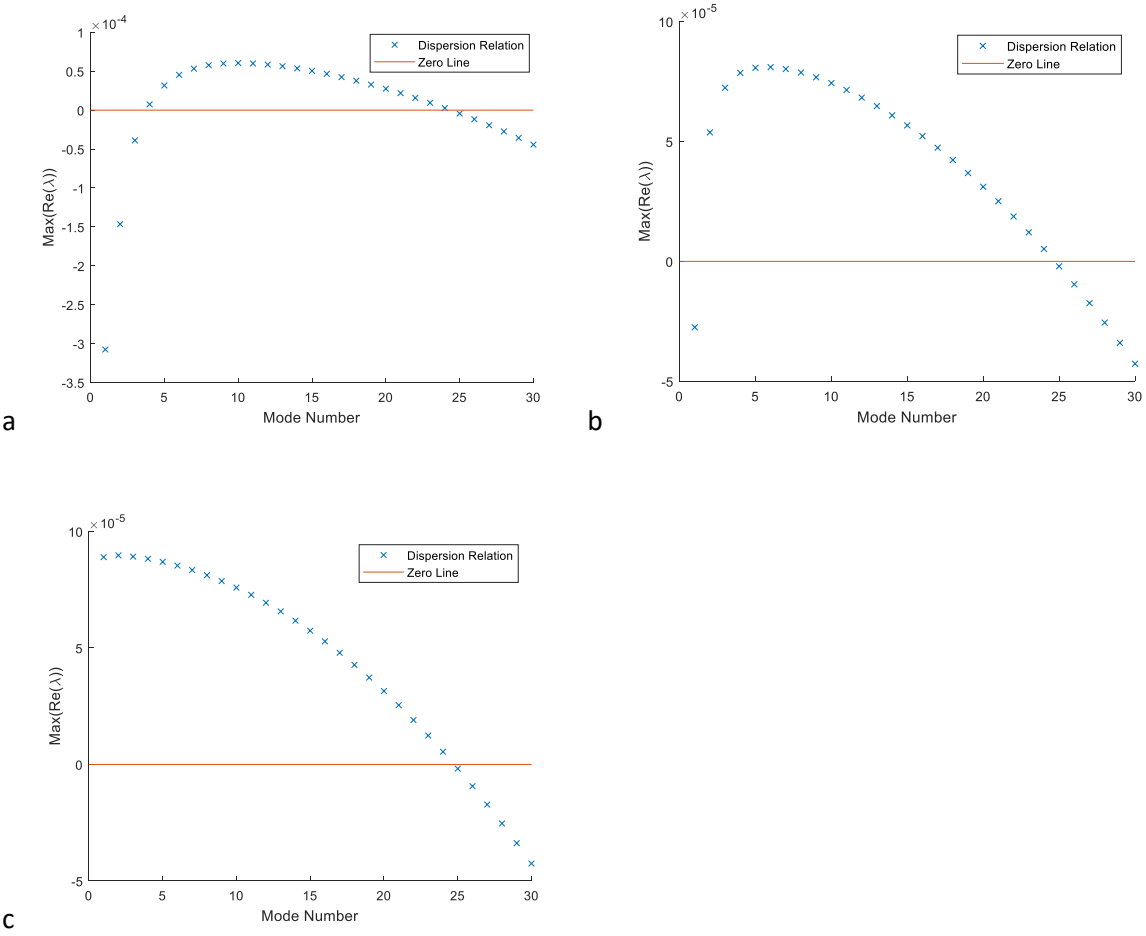

Figure 5.5: Dispersion relation showing the maximum real part of all the eigenvalues of equations 5.3 and 5.4, and the corresponding mode for different values of D. Allowed modes, which have real part of an eigenvalue > 0, increase as D increases: a) for $D = 1000$, admissible modes are: $4 \leq n \leq 24$, b) for $D = 5000$, admissible modes are: $2 \leq n \leq 24$ and c) for $D = 10^4$, admissible modes are: $1 \leq n \leq 24$.

Hence, we opt for the 'halfway point', choosing a_1 and D such that we see lower order modes without them being 'swamped' by those of higher order. Hence, we choose: $a_1 = 1.6 \times 10^{-4}$ and, initially, $D = 10^3$. With $L = 0.2$ metres, the admissible modes are $4 \leq n \leq 24$.

Simulating equations 5.3 and 5.4 gives the results seen in Figure 5.6. This figure shows that the admissible modes do interact, as seen in [90] and produce patterns large enough to discern regions of high and low amplitude. Even more, there are only 3 peaks of uneven heights for C_e, suggesting that although the lowest mode is 4, the other modes interact nonlinearly in such a way that only 3

modes appear to be present. For I, there are 4 visible peaks, as expected. This will be important when coupling the simplified model to the DeGracia model, where there exists an injury threshold above which the cell is predicted to die.

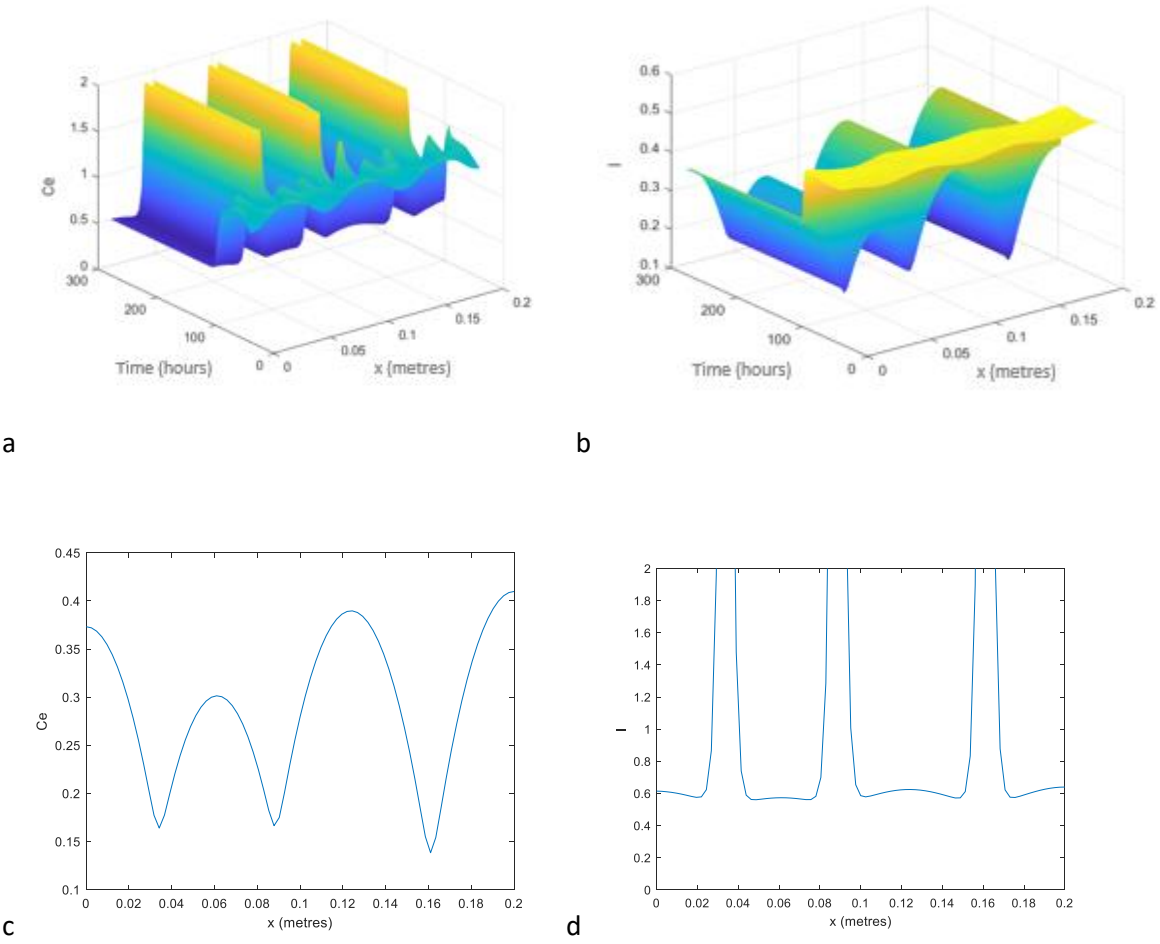

Figure 5.6: Simulations of the Schnakenburg model (Equations 5.3-5.4) show Turing patterns for both C_e and I, (panels a and b) as well as line plots of their equilibrium values (panels c and d). Parameters used were: $a_1 = 1.6 \times 10^{-3}$ and $D = 10^3$.

5.2.1 Physiological Justification

From Table 5.2, we can see that only one term, $a_2 C_e$, is completely fixed. a_1 is only fixed insofar as the parameters of the model given by equations 5.1-5.2 dictate; however, a full model could include further feedback from variables such as A, V and N.

Variables from Modified Model (Equations 5.1-5.2)	Corresponding Variables from Original Model (Equations 5.3-5.4)	Values Free/Fixed
a_1	$\gamma_{ae}\overline{C_a} + \gamma_{ne}\overline{C_n} + v_p\overline{C_a} + v_{pn}\overline{C_n} + f_1$	Partially Fixed
$a_2 C_e$	$-(\gamma_{ae} + \gamma_{ne})C_e$	$a_2 = 3.35 \times 10^{-4}$
$a_3 C_e I$	N/A	Free
$\boldsymbol{b_1}$	$-\boldsymbol{k_a}(\boldsymbol{C_a} - \boldsymbol{C_{a0}})(\boldsymbol{C_a} - \boldsymbol{C_{a1}}) - \boldsymbol{k_n}(\boldsymbol{C_n} - \boldsymbol{C_{n0}})(\boldsymbol{C_n} - \boldsymbol{C_{n1}}) + \boldsymbol{f_2}$	Partially Fixed

Table 5.2: The correspondence between terms from equations 5.1-5.2 and 5.3-5.4. The f_i terms denote feedback from A, V and N terms.

These, kept at steady-state for the analysis of a simplified model, would then need to be equivalent to f_1. Likewise, we would like to preserve the form of b_1, which contains many terms independent of C_e and I, but append to it f_2, which contains feedback terms from other variables present in the full model.

5.3 Inclusion of Advection Terms

This subsection investigates the effects of adding advection terms to equations 5.1-5.2. We would like to acknowledge the help of Philip Maini in this analysis [91].

The boundary conditions here play a crucial role. Whereas Perumpanani *et al.,* [92], showed that advection-diffusion-reaction equations with periodic boundary conditions can lead to the formation of patterns that move across the domain, we cannot use their result for our problem, which requires stricter boundary conditions.

In particular, we require that the concentration of extracellular calcium at one end of the domain remains at equilibrium:

$$u(t, L) = \overline{C_e} \quad (5.24)$$

This boundary condition mimics the unaffected region of the brain.

Since:

$f(\overline{C_e}, \bar{I}) = g(\overline{C_e}, \bar{I}) = 0$ (5.25)

The extracellular calcium concentration must be the same on the other boundary:

$u(t, 0) = \overline{C_e}$ (5.26)

The magnitude of Injury is rather less quantifiable. Hence, we will look at two cases:

1. The magnitude of Injury remains, just like the extracellular calcium concentration, constant on the distant boundary:

   $v(t, L) = \bar{I}$ (5.27)

   We will deal with the nearer boundary during the analysis.

2. No flux of Injury occurs at both boundaries:

   $\frac{\partial v(t,L)}{\partial x} = 0$ (5.28)

These will be important once we have found a general solution for v.

In order to understand what happens when we perturb around the steady-state, we linearise equations 5.1 and 5.2 to give:

$\frac{\partial \hat{u}}{\partial t} = D_u \frac{\partial^2 \hat{u}}{\partial x} + a \frac{\partial \hat{u}}{\partial x} + f_u \hat{u} + f_v \hat{v}$ (5.29)

$\frac{\partial \hat{v}}{\partial t} = D_v \frac{\partial^2 \hat{v}}{\partial \hat{x}^2} + b \frac{\partial \hat{v}}{\partial x} + g_u \hat{u} + g_v \hat{v}$ (5.30)

Now, assuming again that the solution for $\hat{u}$ is:

$\hat{u} = \alpha \exp(\lambda t) \exp(\mu x) \sin\left(\frac{n\pi x}{L}\right)$ (5.31)

And let $\hat{v}$ be a little more general:

$\hat{v} = \exp(\lambda t) \exp(\mu x) \left(\beta \sin\left(\frac{n\pi x}{L}\right) + \gamma \cos\left(\frac{n\pi x}{L}\right)\right)$ (5.32)

Substituting equations 5.31 and 5.32 into equation 5.29 gives:

$$\alpha\lambda \sin\left(\frac{n\pi x}{L}\right) = \alpha D_u \left(\mu^2 \sin\left(\frac{n\pi x}{L}\right) - \frac{n^2\pi^2}{L^2}\sin\left(\frac{n\pi x}{L}\right) + 2\right) + \alpha a \left(\mu \sin\left(\frac{n\pi x}{L}\right) + \frac{n\pi}{L}\cos\left(\frac{n\pi x}{L}\right)\right) +$$

$$\alpha f_u \sin\left(\frac{n\pi x}{L}\right) + f_v \left(\beta \sin\left(\frac{n\pi x}{L}\right) + \gamma \cos\left(\frac{n\pi x}{L}\right)\right) \quad (5.33)$$

By collecting the coefficients of both the sine and cosine terms, we can obtain two equations:

$$\alpha \left(D_u \left(\mu^2 - \frac{n^2\pi^2}{L^2}\right) - \lambda + f_u + \mu a\right) + \beta f_v = 0 \quad (5.34)$$

$$\left(\frac{2D_u \mu n\pi}{L} + \frac{an\pi}{L}\right)\alpha + f_v \gamma = 0 \quad (5.35)$$

To solve the five unknown variables $(\alpha, \beta, \gamma, \lambda, \mu)$, we require three more equations, two of which will come from collecting coefficients of the sine and cosine terms in the v equation:

$$\lambda\beta \sin\left(\frac{n\pi x}{L}\right) + \lambda\gamma \cos\left(\frac{n\pi x}{L}\right)$$

$$= \beta \left(D_v \left(\mu^2 - \frac{n^2\pi^2}{L^2}\right)\sin\left(\frac{n\pi x}{L}\right) + \frac{2D_v \mu n\pi}{L}\cos\left(\frac{n\pi x}{L}\right)\right) + \gamma \left(D_v \left(\mu^2 - \frac{n^2\pi^2}{L^2}\right)\cos\left(\frac{n\pi x}{L}\right) -$$

$$\frac{2D_v \mu n\pi}{L}\sin\left(\frac{n\pi x}{L}\right)\right) + \frac{n\pi b\beta}{L}\cos\left(\frac{n\pi x}{L}\right) - \frac{n\pi b\gamma}{L}\sin\left(\frac{n\pi x}{L}\right) + g_u \alpha \sin\left(\frac{n\pi x}{L}\right)$$

$$+ b\beta\mu \sin\left(\frac{n\pi x}{L}\right) + b\gamma\mu \cos\left(\frac{n\pi x}{L}\right) + g_v \beta \sin\left(\frac{n\pi x}{L}\right) + g_v \gamma \cos\left(\frac{n\pi x}{L}\right) \quad (5.36)$$

The two subsequent equations are:

$$\beta \left(D_v \left(\mu^2 - \frac{n^2\pi^2}{L^2}\right) + g_v + b\mu - \lambda\right) - \left(\frac{2D_v \mu n\pi + n\pi b}{L}\right)\gamma + g_u \alpha = 0 \quad (5.37)$$

$$\beta \left(\frac{2D_v n\pi + n\pi b}{L}\right) + \gamma \left(D_v \left(\mu^2 - \frac{n^2\pi^2}{L^2}\right) + g_v + b\mu - \lambda\right) = 0 \quad (5.38)$$

Equations 5.34-5.35 and 5.37-5.38 contribute 4 equations towards the determination of the 5 unknowns. The last comes from the chosen boundary conditions.

Let us examine the following two cases:

Case I: $\bar{v} = 0$ at $x = L$

This BC implies $\gamma = 0$. This, in turn, means that, at $x = 0, \bar{v} = 0$ and hence the solution is forced to the equilibrium value at both boundaries.

We attempted to solve equations 5.34-5.35 and 5.37-5.38 numerically subject to this constraint. Unfortunately, only the trivial solution exists in this case. This implies that the presence of advection, under Dirichlet boundary conditions, prevents the formation of spatial patterns.

Case II: $\frac{\partial \bar{v}}{\partial x} = 0$ at $x = 0$ and $x = L$

This BC leads to the following constraint:

$$\exp(\lambda t)\left(\mu\gamma + \frac{n\pi\beta}{L}\right) = 0 \quad (5.39)$$

Note that the BC at the boundary, $\frac{\partial \bar{v}}{\partial x} = 0$ at $x = L$, is still fulfilled as:

$$\exp(\mu L)\exp(\lambda t)\left(\mu\gamma + \frac{n\pi\beta}{L}\right) = 0 \quad (5.40)$$

Imposing equation 5.39 ensures this is true.

Again, we tried to solve equations 5.34-5.35 and 5.37-5.38 numerically, subject to equation 5.39; again, however, only the trivial solution exists for this BC; advection still destroys any spatial heterogeneities in this case.

5.3.1 Conclusions

In this subsection, we showed that the presence of advection destroys patterns formed in its absence, for our parameter set. We assume that the extracellular calcium concentration is at steady-state far away (at one boundary) and see that it must also take this value at the other boundary. After forcing the injury magnitude to obey either Dirichlet or Neumann boundary conditions, we ascertain numerically that there exists only the trivial solution to the resultant equations. Henceforth, we will run simulations on the model without including the advection terms.

5.4 Simulation Results

Having determined parameter values for the model in Sections 5.1 and 5.2, we can now simulate the model and show the results. We use the method of lines approach, with a ten-point finite difference scheme and ode15s, a stiff ODE solver that uses the numerical differentiation formulae of orders 1-5 to solve the resultant ODEs.

5.4.1 Model in absence of feedback

As we saw from Chapters 3, 4 and 5.1, the equations of the full model are:

$$\varphi_a \frac{dC_a}{dt} = v_c\left(\frac{1}{\varphi_{aer}}(C - \varphi_a C_a - \varphi_n C_n - \varphi_{ner} C_{ner} - \varphi_e C_e) - C_a\right) - v_{s3} C_a - \gamma_{ae}(C_a - C_e) - v_p C_a \quad (5.41)$$

$$\varphi_n \frac{\partial C_n}{\partial t} = v_{Cn}(C_{ner} - C_n) - v_{s3n} C_n - \gamma_{ne}(C_n - C_e) - v_{pn} C_n \quad (5.42)$$

$$\varphi_{ner} \frac{\partial C_{ner}}{\partial t} = -v_{Cn}(C_{ner} - C_n) + v_{s3n} C_n \quad (5.43)$$

$$\frac{\partial C_e}{\partial t} = D_1 \nabla^2 C_e + a_1 - a_2 C_e + a_3 C_e{}^2 I \quad (5.44)$$

$$\frac{\partial I}{\partial t} = D_2 \nabla^2 I + b_1 - a_3 C_e^2 I \quad (5.45)$$

$$\frac{\partial D}{\partial t} = \frac{(c_D I exp(\lambda_D I))^4}{(c_D I exp(\lambda_D I))^4 + S^4} - D \quad (5.46)$$

$$\frac{\partial S}{\partial t} = \frac{(c_s I exp(-\lambda_S I))^4}{(c_s I exp(-\lambda_s I))^4 + D^4} - S \quad (5.47)$$

$$\frac{\partial A}{\partial t} = -k_{a-} H[D - S](D - S)A + k_{a+} H[S - D](S - D)V \quad (5.48)$$

$$\frac{\partial V}{\partial t} = k_{a-} H[D - S](D - S)A - k_{a+} H[S - D](S - D)V - k_{v-} H[D - S](D - S)V \quad (5.49)$$

$$\frac{\partial N}{\partial t} = k_{v-} H[D - S](D - S)V \quad (5.50)$$

where $H[x]$ represents the Heaviside step function.

Table 5.3 shows the parameter values used. Notice that the parameters k_{a+}, k_{a-} and k_{v-} are rate constants denoting how quickly cells transition from the Alive to Vulnerable (and back again), to

Necrotised states. These three parameter values are found by visual inspection of simulations, while the others either keep their values from previous models or are found by the analyses we have carried out previously.

Since there is no feedback, if we can guarantee that equations 5.3 and 5.4 meet the criteria for the formation of Turing instabilities, then equations 5.41 – 5.50 will also show spatial inhomogeneities.

We do make one change to the parameters: $c_s = 4$ (from $c_s = 20$ in DeGracia's model). This is the threshold parameter, which is a factor in determining at which value the stress equals the damage. We can subsequently set the threshold Injury value, $I_{threshold}$, which represents mathematically the value of I where $\overline{D} = \bar{S}$. This is given by DeGracia (7) as:

$$I_{threshold} = \frac{\ln(c_s) - \ln(c_D)}{I_0(\lambda_D + \lambda_S)} \quad (5.51)$$

Knowing from our simulations in Section 5.2 that if we choose $I_{threshold} \approx 0.34$ then those regions in the 'peaks' of I will surpass the threshold value and, eventually, be predicted to die.

Now we run the model and obtain the results shown in Figure 5.7. In addition, we also show other results in Figures 5.8 and 5.9, which arise from increasing the ratio of diffusion coefficients, D. To ensure the Turing patterns are clearly visible, we do not show the first 20 hours of the simulation, since the critical time scale for pattern formation is $\frac{L^2}{D_2} \approx 19$ hours. This is an order of magnitude larger than we would expect for patterns to occur and suggests that the diffusion coefficient of the Injury magnitude, D_2, may be too low. However, increasing it will result in a smaller D, leading to Turing space shrinking and the lowest admissible mode increasing, as we have discussed above. Since both these properties are also unrealistic, we must concede that this high critical time-scale is a current weakness of the model.

Parameter	Suggested Value (85% CBF decrease)	Units
φ_a	0.225	Dimensionless
φ_{aer}	0.025	Dimensionless
φ_n	0.405	Dimensionless
φ_{ner}	0.045	Dimensionless
φ_e	0.2	Dimensionless
C_0	2.00	mM/L
γ_{ae}	2.37×10^{-4}	$/s$
γ_{ne}	9.8×10^{-5}	$/s$
v_{cn}	7.96×10^{-11}	$/s$
v_{s3}	1.54×10^{-8}	$/s$
v_{s3n}	-1.40×10^{-4}	$/s$
v_p	7.58×10^{-4}	$/s$
v_{pn}	2.41×10^{-4}	$/s$
D_1	6×10^{-10}	m^2/s
D_2	6×10^{-7}	m^2/s
a_1	1.60×10^{-4}	mM/s
a_2	3.35×10^{-4}	$/s$
a_3	3.25×10^{-4}	$/(mM^2\ s)$
b_1	2.79×10^{-4}	$/(mM\ s)$
c_D	0.1	$/s$
c_S	4	$/s$
λ_D	0.1	$/mM$
λ_S	0.9	$/mM$
k_{a+}	1	$/s$
k_{a-}	6×10^{-5}	$/s$
k_{v-}	10^{-6}	$/s$

Table 5.3: Table showing model parameters, values used and their units.

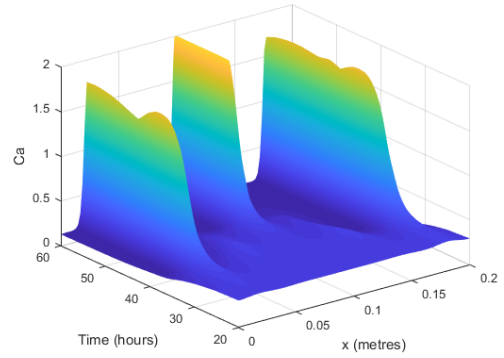
Ca
Time (hours)
x (metres)

a

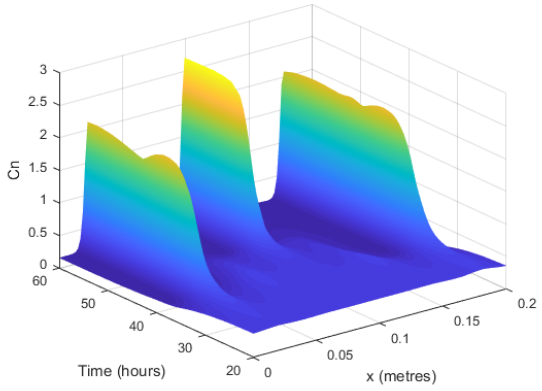
Cn
Time (hours)
x (metres)

b

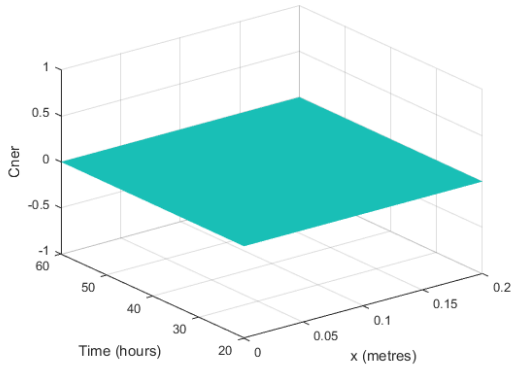
Cner
Time (hours)
x (metres)

c

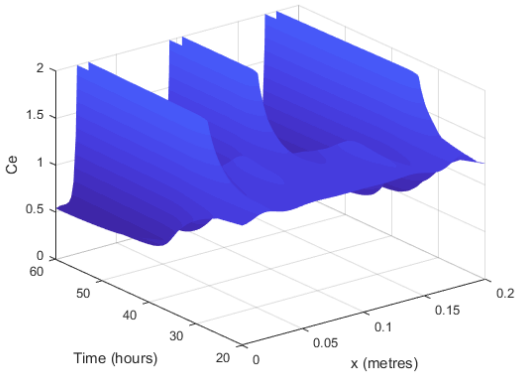
Ce
Time (hours)
x (metres)

d

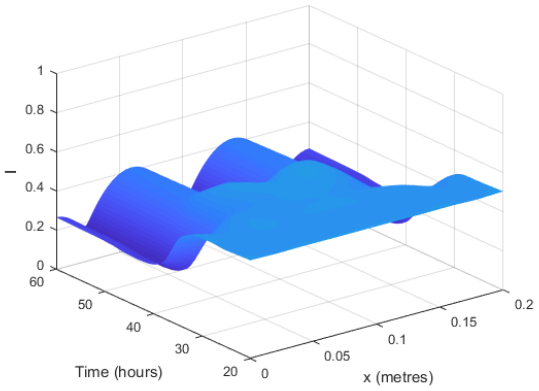
I
Time (hours)
x (metres)

e

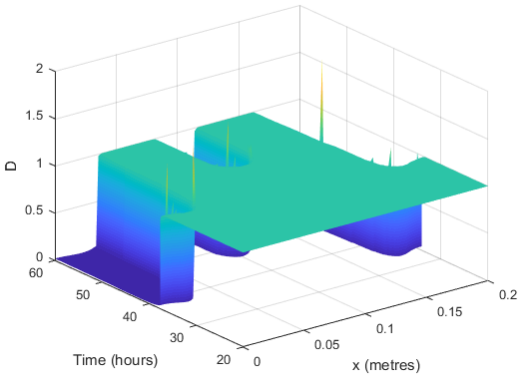
D
Time (hours)
x (metres)

f

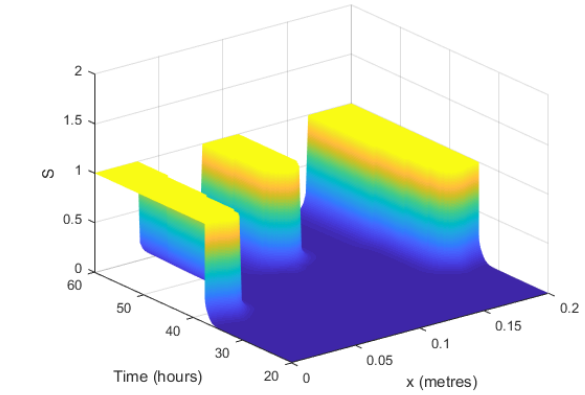

g

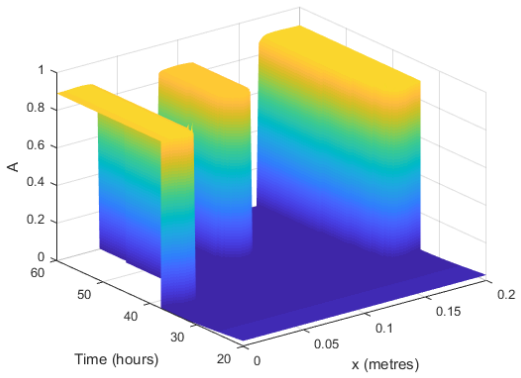

h

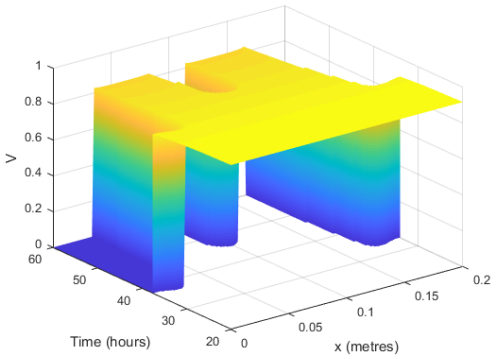

i

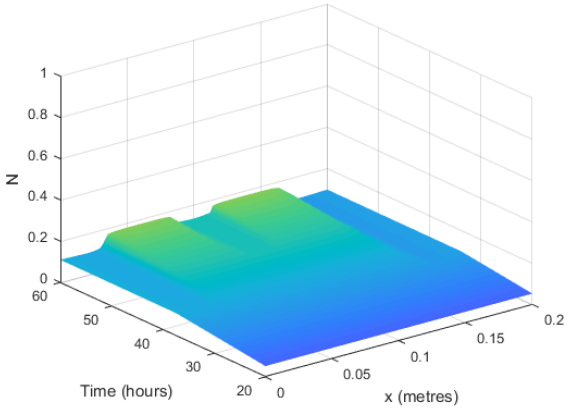

j

Figure 5.7: Simulations of the model without feedback, showing concentrations of: a. astrocytic calcium, b. neuronal calcium, c. Neuronal ER calcium, d. extracellular calcium, e. Injury, f. Damage, g. Stress, h. Alive cell proportion, i. Vulnerable Cell proportion, j. Necrotised cell proportion. Parameters values are given in Table 5.3.

All three figures, all the graphs, except for the constant C_{ner} variable, show spatial inhomogeneities after Turing instabilities start forming at around 30 hours. These originate from the instabilities created by the two diffusion-reaction equations (equations 5.3 and 5.4). Until then, the Damage inflicted upon the brain far exceeds the Stress (not shown). After Turing instabilities begin forming, the three figures start to differ in their predictions.

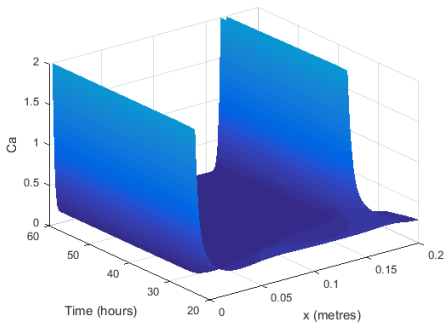
Ca
Time (hours)
x (metres)

a

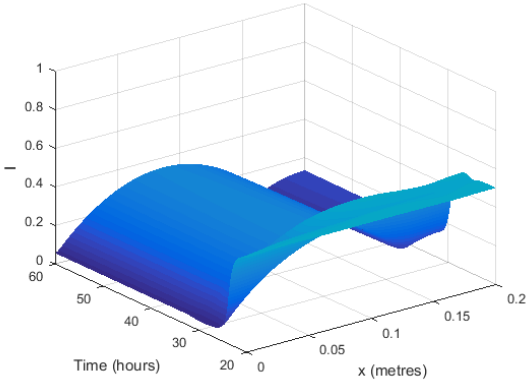
I
Time (hours)
x (metres)

b

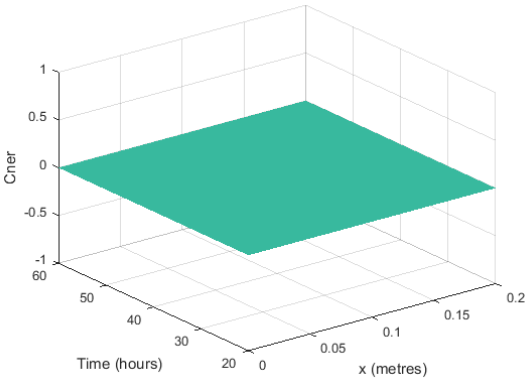
Cner
Time (hours)
x (metres)

c

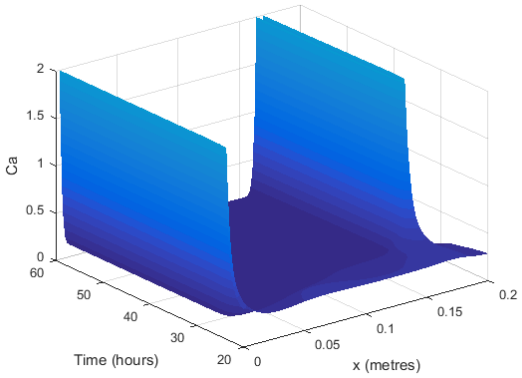
Ca
Time (hours)
x (metres)

d

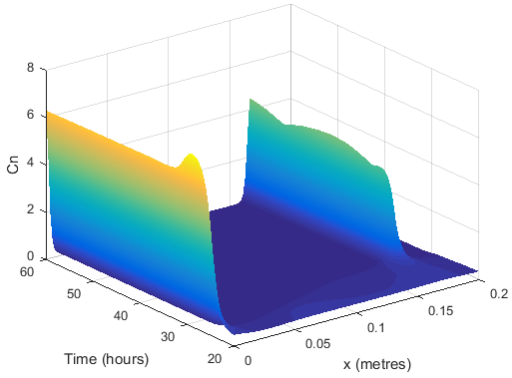
Cn
Time (hours)
x (metres)

e

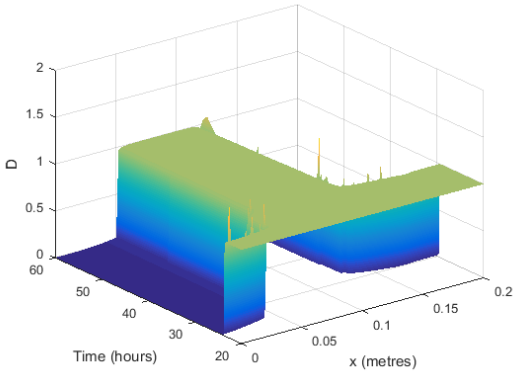
D
Time (hours)
x (metres)

f

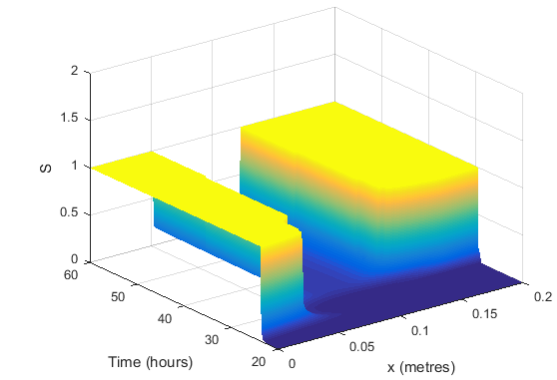

g

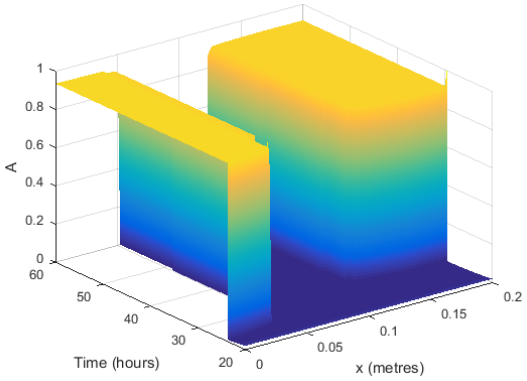

h

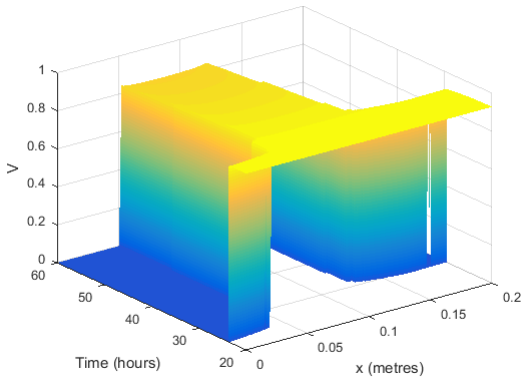

i

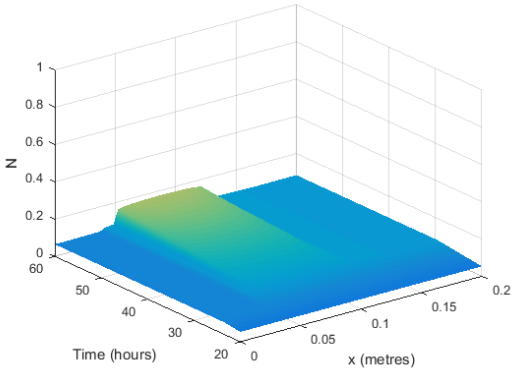

j

Figure 5.8: Simulations of the model without feedback, showing concentrations of: a. astrocytic calcium, b. neuronal calcium, c. Neuronal ER calcium, d. extracellular calcium, e. Injury, f. Damage, g. Stress, h. Alive cell proportion, i. Vulnerable Cell proportion, j. Necrotised cell proportion. Parameters values are given in Table 5.3, except for $D = 5000$ and, hence, $D_2 = 3 \times 10^{-6}$.

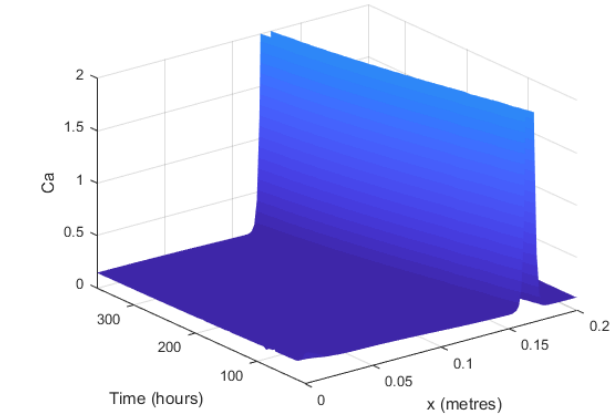
Ca
Time (hours)
x (metres)

a

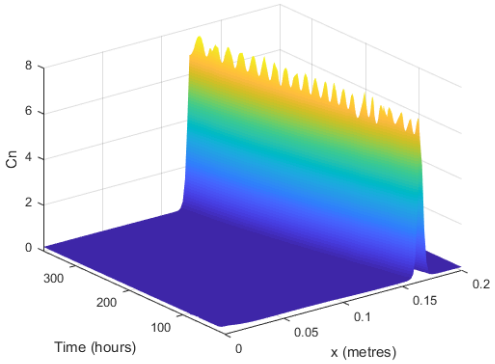
Cn
Time (hours)
x (metres)

b c

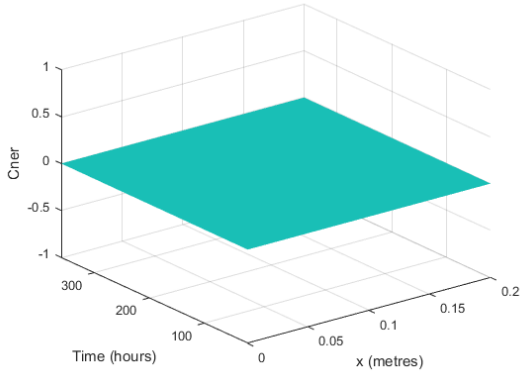
Cner
Time (hours)
x (metres)

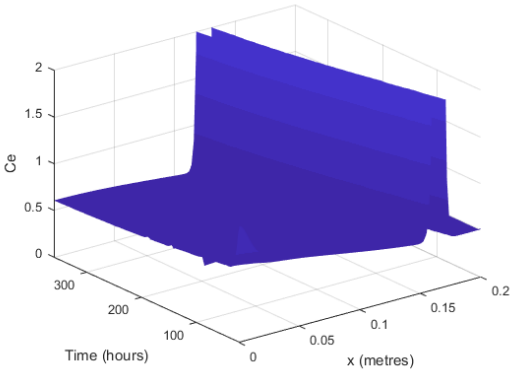
Ce
Time (hours)
x (metres)

d

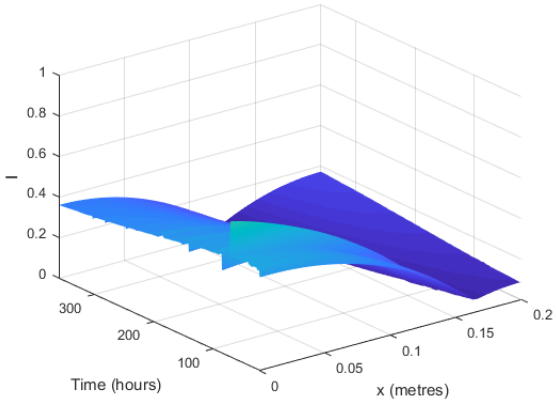
I
Time (hours)
x (metres)

e

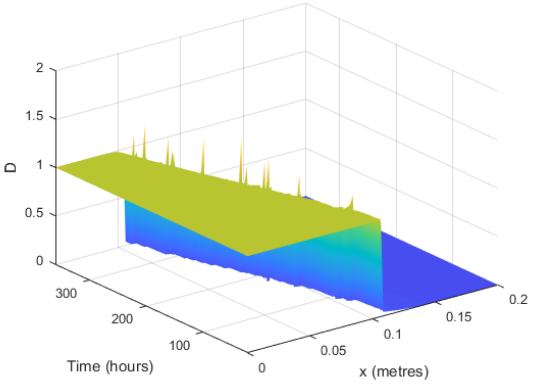
D
Time (hours)
x (metres)

f

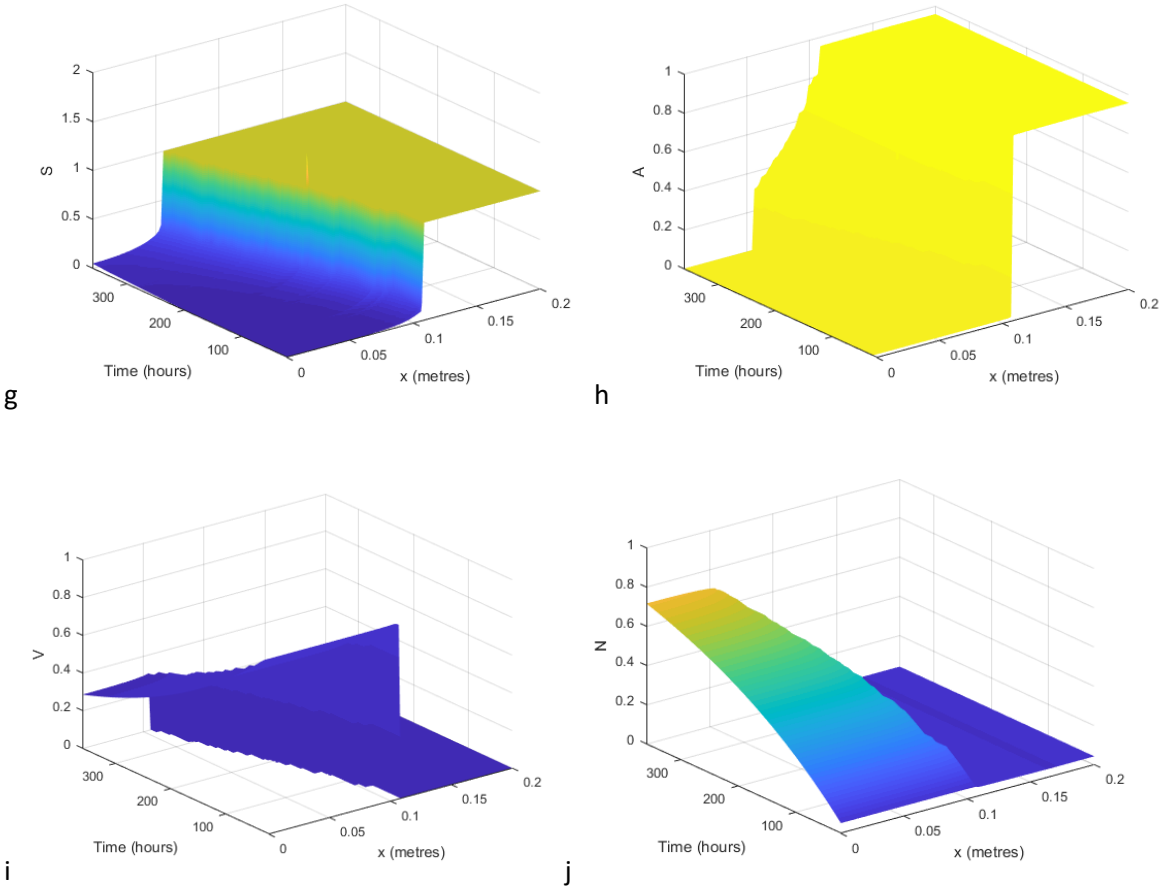

Figure 5.9: Simulations of the model without feedback, showing concentrations of: a. astrocytic calcium, b. neuronal calcium, c. Neuronal ER calcium, d. extracellular calcium, e. Injury, f. Damage, g. Stress, h. Alive cell proportion, i. Vulnerable Cell proportion, j. Necrotised cell proportion. Parameters values are given in Table 5.3, except for $D = 10^4$ and, hence, $D_2 = 6 \times 10^{-6}$.

In the case where $D = 1000$, (Figure 5.7), the Stress factors overcome those of the Damage except in two regions. These correspond to the positions of the peaks of the Injury variable, I. Consequently, the proportion of Alive cells in these regions stays low and the dead cell proportion increases. Otherwise, the model predicts that most cells recover due to the internal Stress responses, without need for clinical intervention.

For $D = 5000$, shown in Figure 5.8, there is now only one (slightly larger) region where D exceeds S. This corresponds to one region near the centre where the proportion of dead cells, N, is noticeably higher than 0 – and still increasing at the end of the simulation.

When $D = 10^4$, which is shown in Figure 5.9, we see in the C_e and I simulations one part of a certain oscillation (on the LHS of the graph) connected to the other (on the RHS). The right side of I

does not meet the threshold for making $D > S$, according to equation 5.51, but the left does and, hence, cells in one region on the left are predicted to die, while many cells in this region are also vulnerable and may be salvaged. This particular case appears to be the closest representation of the physiology that we see after an episode of stroke. This change can be explained by noting that Turing Space now includes the first mode, which we show in Fig. 5.5c. We note also that the graphs for Damage, D, all contain artefacts in the form of 'spikes' near regions of sharp changes in values (high spatial gradients). We believe that this is a by-product of the numerical implementation where the weighted averaging of the ten grid points remains too coarse in the face of dramatic changes on the left and right sides of the point being calculated.

5.4.2 Model with Feedback

To add feedback to the model, we note that the calcium pumps in both the astrocytes and neurons only work when the cell is alive or vulnerable. Hence, we multiply the terms representing these processes (v_p and v_{pn}) by $(A + V)$.

In addition, the residual terms f_1 and f_2 in Table 5.2 must also be incorporated. These are defined to be:

$$f_1 = a_1 - \overline{C_a}\gamma_{ae} - \overline{C_n}\gamma_{ne} - \overline{C_a}v_p - \overline{C_n}v_{pn} \quad (5.52)$$

$$f_2 = b_1 + \overline{C_a}(\overline{C_a} - 1)k_a + \overline{C_n}(\overline{C_n} - 1)k_n \quad (5.53)$$

f_1 and f_2 model terms that are part of the feedback process; when cells die, so too do these processes cease. This can be modelled by multiplying each by N. As the proportion of functioning cells decreases, however, this has a knock-on effect on these processes.

Notice that, at the inception of stroke, all cells are Alive and so, at least at $t = 0$, the model with feedback is the effectively the same as the one without it.

Thus, the equations become:

$$\varphi_a \frac{dC_a}{dt} = v_c \left(\frac{1}{\varphi_{aer}} (C_0 - \varphi_a C_a - \varphi_n C_n - \varphi_{ner} C_{ner} - \varphi_e C_e) - C_a \right) - v_{s3} C_a -$$

$$\gamma_{ae}(C_a - C_e) - v_p C_a \, (A + V) \quad (5.54)$$

$$\varphi_n \frac{\partial C_n}{\partial t} = v_{Cn}(C_{ner} - C_n) - v_{s3n} C_n - \gamma_{ne}(C_n - C_e) - v_{pn} C_n (A + V) \quad (5.55)$$

$$\varphi_{ner} \frac{\partial C_{ner}}{\partial t} = -v_{Cn}(C_{ner} - C_n) + v_{s3n} C_n \quad (5.56)$$

$$\varphi_e \frac{\partial C_e}{\partial t} = D_1 \nabla^2 C_e + a_1 + N f_1 - a_2 C_e + a_3 C_e{}^2 I \quad (5.57)$$

$$\frac{\partial I}{\partial t} = D_2 \nabla^2 I + b_1 + N f_2 - a_3 C_e^2 I \quad (5.58)$$

The remaining equations stay unchanged.

The Turing Space of the system will change, since all 10 equations will now influence the allowed modes. However, as there are more than 4 differential equations and, in addition, the Damage/Stress equations do not have a closed-form analytical solution for their equilibria, we cannot determine the Turing Space analytically. Hence, we proceed straight to model simulation. Simulations of these equations with the parameter values from Table 5.3 leads to the plots shown in Figure 5.10. We also show, in Figures 5.11 and 5.12, the case where D is increased to 5000 and 10000, respectively. Again, we do not show the first 20 hours of the simulation to emphasise the Turing patterns produced.

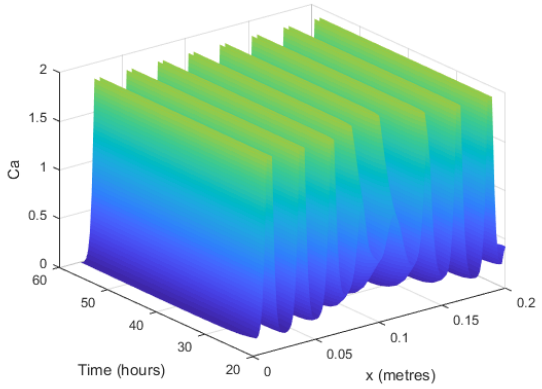
Ca
Time (hours)
x (metres)

a

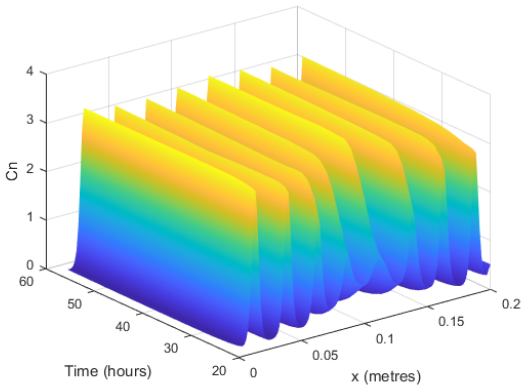
Cn
Time (hours)
x (metres)

b

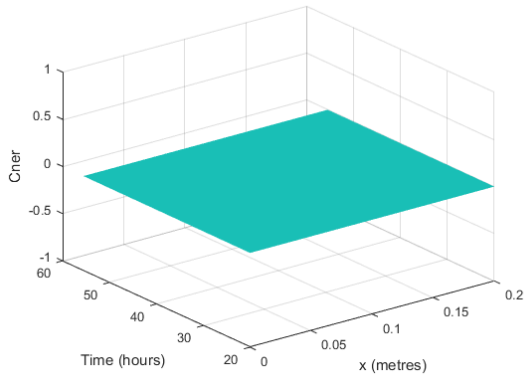
Cner
Time (hours)
x (metres)

c

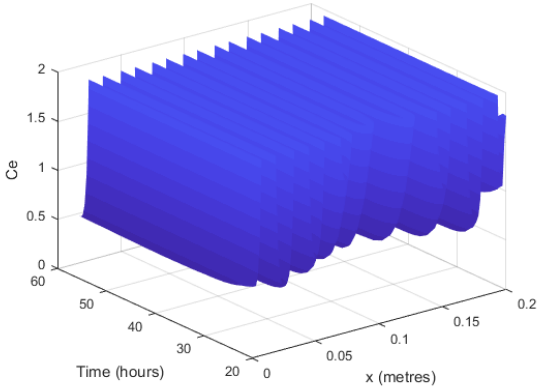
Ce
Time (hours)
x (metres)

d

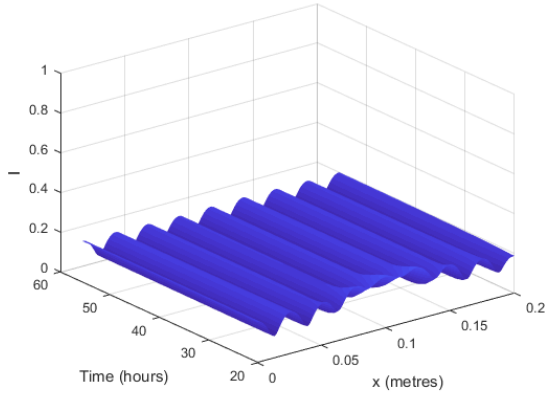
I
Time (hours)
x (metres)

e

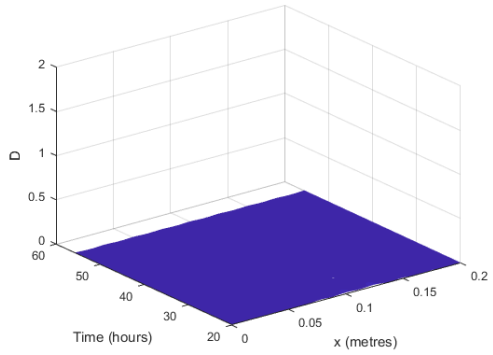
D
Time (hours)
x (metres)

f

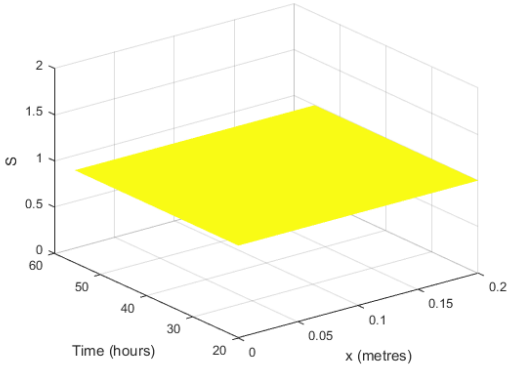
S
Time (hours)
x (metres)

g

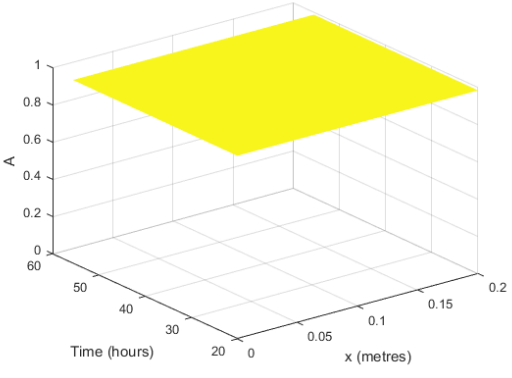
A
Time (hours)
x (metres)

h

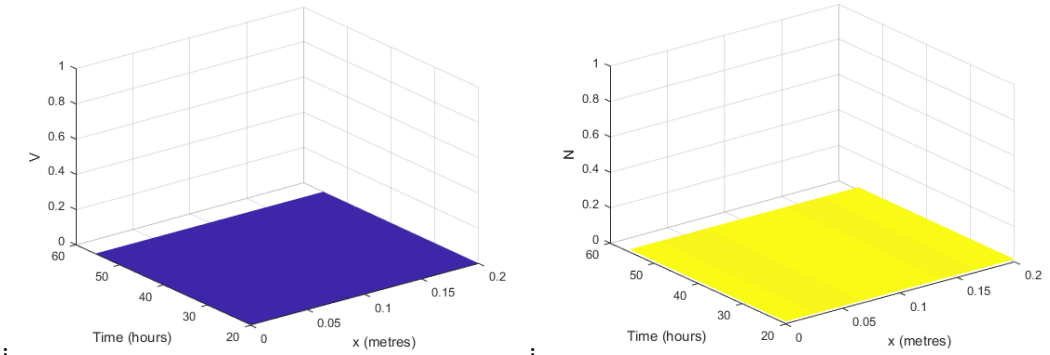

i j

Figure 5.10: Simulations of the model in the presence of feedback, showing concentrations of: a. astrocytic calcium, b. neuronal calcium, c. Neuronal ER calcium, d. extracellular calcium, e. Injury, f. Damage, g. Stress, h. Alive cell proportion, i. Vulnerable Cell proportion, j. Necrotised cell proportion. Parameter values are given in Table 5.3.

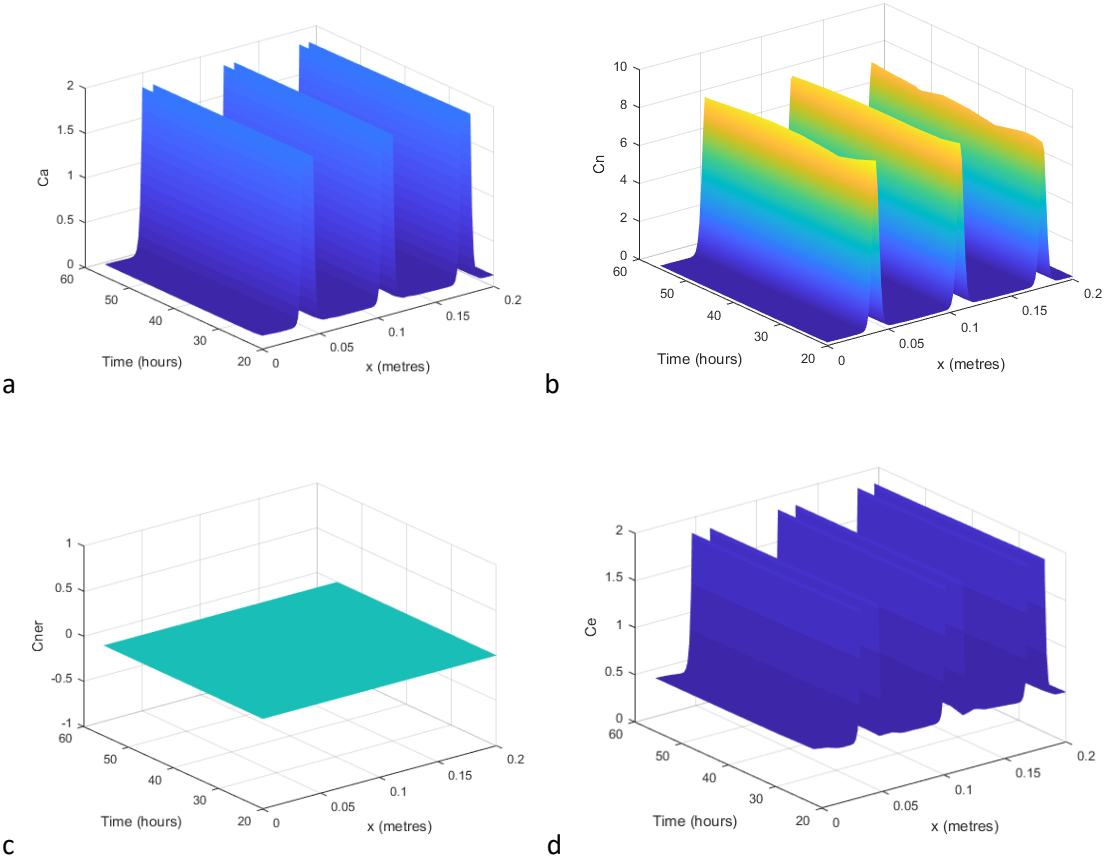

a b

c d

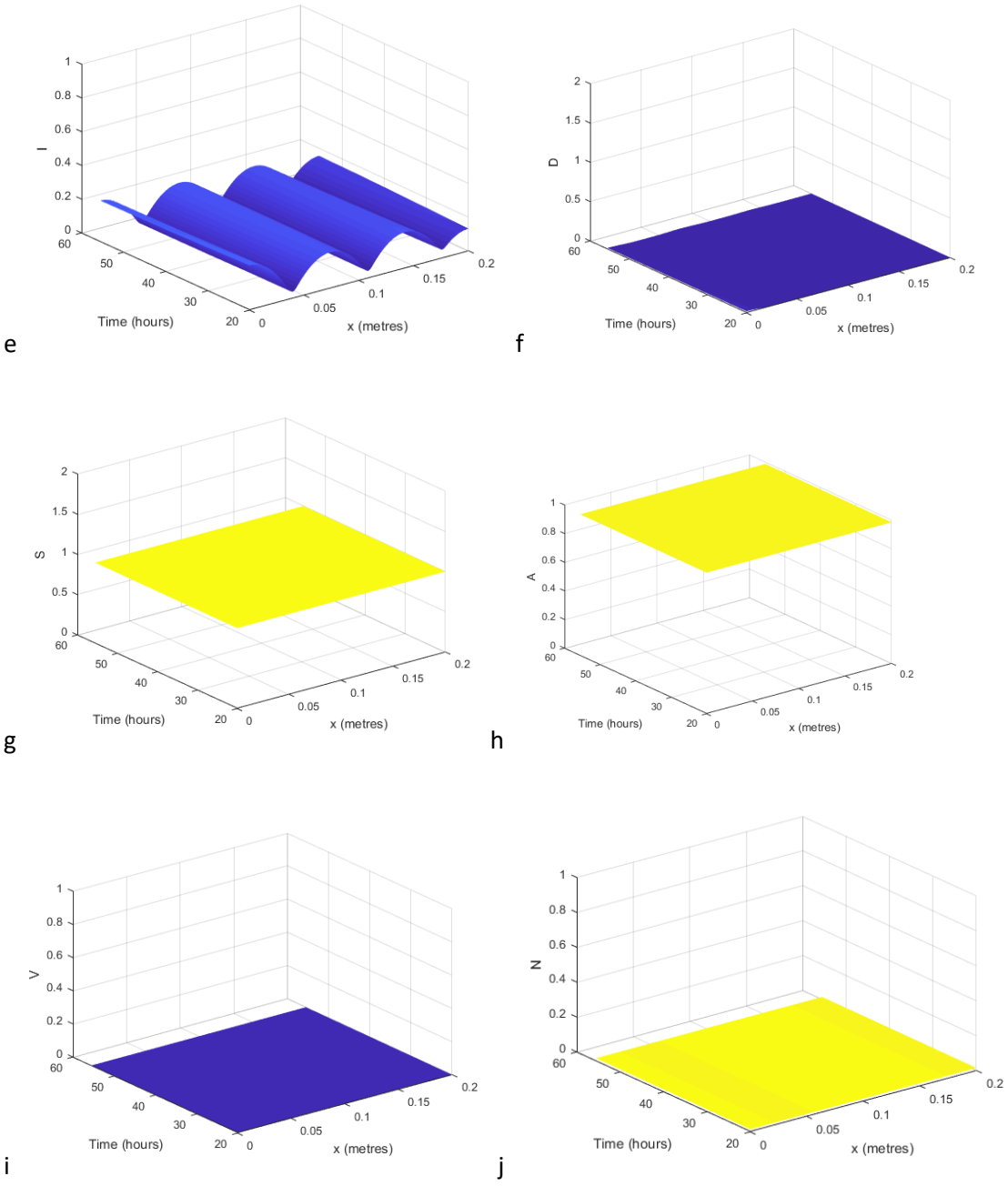

Figure 5.11: Simulations of the model in the presence of feedback, showing concentrations of: a. astrocytic calcium, b. neuronal calcium, c. Neuronal ER calcium, d. extracellular calcium, e. Injury, f. Damage, g. Stress, h. Alive cell proportion, i. Vulnerable Cell proportion, j. Necrotised cell proportion. Parameter values are given in Table 5.3 except for $D = 3 \times 10^{-6}$.

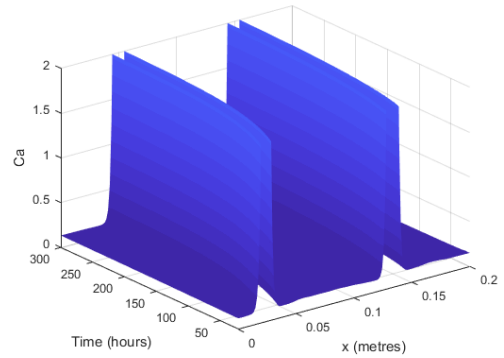
Ca
Time (hours)
x (metres)

a

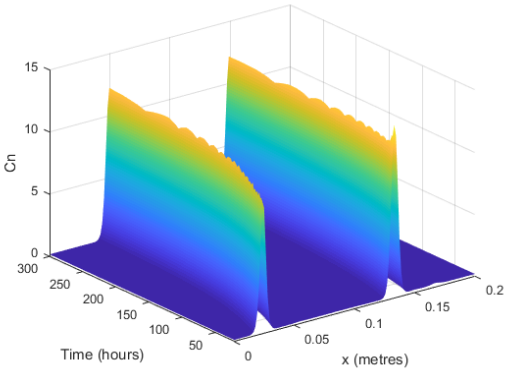
Cn
Time (hours)
x (metres)

b

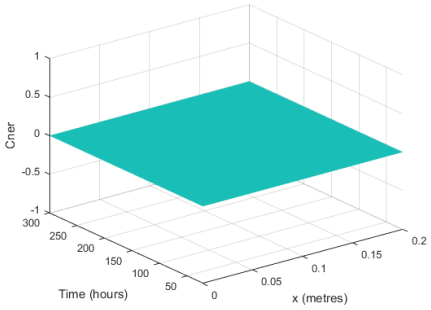
Cner
Time (hours)
x (metres)

c

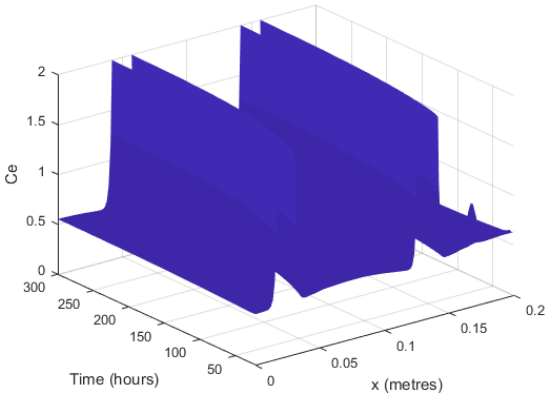
Ce
Time (hours)
x (metres)

d

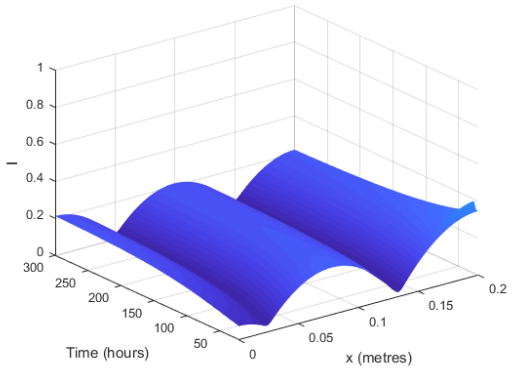
I
Time (hours)
x (metres)

e

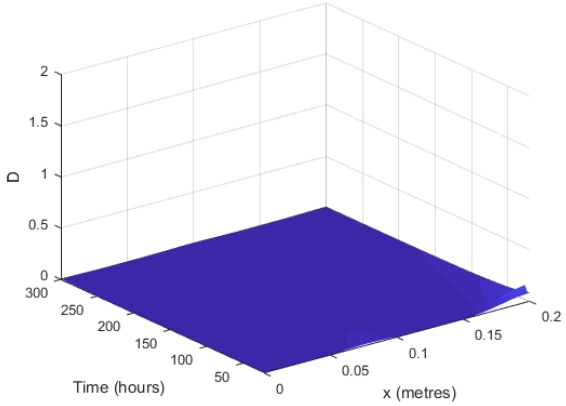
D
Time (hours)
x (metres)

f

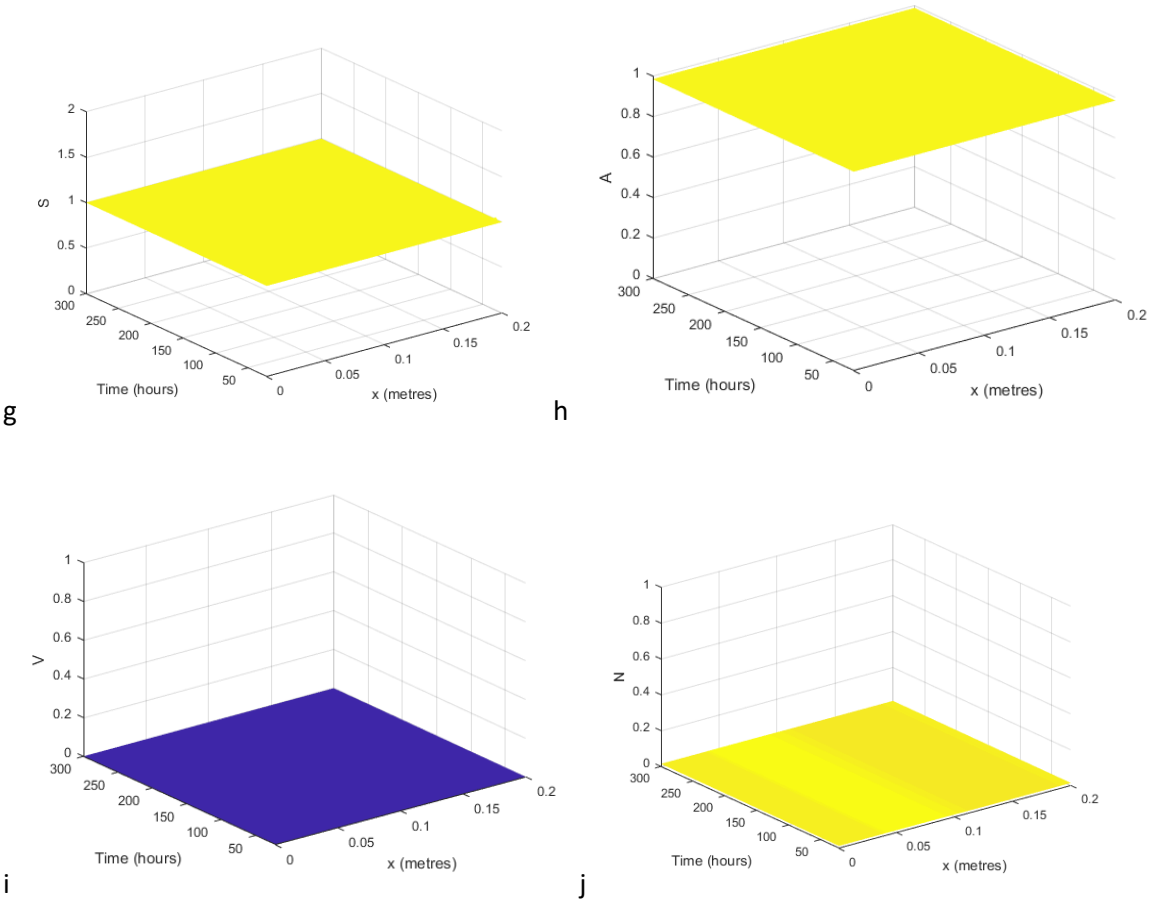

Figure 5.12: Simulations of the model in the presence of feedback, showing concentrations of: a. astrocytic calcium, b. neuronal calcium, c. Neuronal ER calcium, d. extracellular calcium, e. Injury, f. Damage, g. Stress, h. Alive cell proportion, i. Vulnerable Cell proportion, j. Necrotised cell proportion. Parameter values are given in Table 5.3 except for $D = 6 \times 10^{-6}$.

In all three figures, we can see that the magnitude of injury has more peaks and troughs than when feedback is absent (Figures 5.7-5.9). While this results in many modes in both D and S as well, they are each much smaller and so we cannot easily discern individual peaks. This, in turn, means that there are no longer any regions where D or S display large enough spatial inhomogeneities (as we do see in Figures 5.7-5.9 f and 5.7-5.9 g) such that the subtraction of D from S switches signs in different regions. In other words, throughout the domain, Stress exceeds the Damage. The knock-on effect this has is that our model subsequently predicts that cells are predominantly alive.

We postulate that this happens because the addition of feedback forces the Turing space to change, making fewer modes of lower-order admissible. The remaining higher-order modes are smaller in amplitude, and so with our choice of $I_{threshold}$ (equation 5.51) D will always remain smaller than S.

5.5 Discussion

This chapter first investigates how our model can exhibit Turing patterns and second using the parameters found in this analysis, shows the resulting model simulations, both with and without feedback.

Manifested in the results presented in the previous chapters is a model with both strengths and limitations. The strengths are as follows: first, with one set of equations, we can potentially account for the spatial variabilities observed in stroke. Currently, we obtain (in the model without feedback) regions with high proportions of dead cells and others where they survive. Moreover, these inhomogeneities occur after steady-state has been reached, rather than as the result of initial perturbations (as we observed in Figure 4.5f). With some modifications, we can potentially simulate this model to represent the core, penumbra and unaffected regions observed after stroke.

We also found the Turing Space in terms of the parameters a_1 and D. As noted by Murray (48,56), the larger the value of D, the larger the Turing Space; $D = 15,$ moreover, is the critical value below which Turing instabilities do not occur. By selecting appropriate parameter values for a_1 and D, it is also possible to limit the number of modes observed using the technique of mode isolation.

Adding an advection term, no matter how small, renders the system stable and so no Turing patterns are observed; this is another interesting aspect of the work and suggests that, if Turing instabilities are indeed the phenomenon that causes spatial inhomogeneities in stroke, then advection should not occur in the context of calcium transport; this would be a possible experiment to test the validity of our model. Finally, adding feedback changes the Turing Space and increases the dominant mode. We will talk about the modelling implications of this in Chapter 6. Notice, also, the power of mathematical modelling at the beginning of the chapter: we stipulated the need for our model to display Turing patterns and surmised that the model represented by equations 5.1-5.2 could not satisfy this requirement. Hence, we adjusted the model (equations 5.3 and 5.4) and found that certain feedback terms were required, providing physiological justification for their inclusion in Section 5.2.1.

After running the model (equations 5.41-5.50), we saw that Turing instabilities can indeed be observed, particularly in the case without feedback. Moreover, increasing D further makes admissible even the first mode. Hence, when $D = 10^4$, the resulting simulations show a clear ischaemic core next to an unaffected region (Figure 5.9). However, plots of the dispersion relation show that all modes up to $n = 24$ are also admissible and that these interfere with the lower-order modes. When we introduce feedback into the model, the lower-order modes become inadmissible and so an increasing number of patterns are formed, each with lower amplitude.

This, then, brings us to discuss the aspects of the model that we should improve. For instance, at present we use Cartesian coordinates and stay in one dimension. Second, the ideal model should only display the first mode, corresponding to the ischaemic core; in our current model, however, several modes coexist, despite our efforts to limit them. Moreover, the higher-order modes prevalent in our feedback model render the amplitudes of the patterns too small to produce regions where cells predominantly survive in one region and die in another; we must adjust the values of the model parameters such that this happens and Chapter 6.2 discusses a possible strategy to do so.

We should also put more thought into the initial conditions. Because we cannot tell if Turing instabilities occur when linear stability breaks down, we have only chosen initial conditions that are close to the equilibrium values. In addition, these values are constant across the domain. It would be worthwhile investigating the nonlinear effects when the initial conditions are further away from steady-state and take, for example, the form of a *tanh* function (see equation 4.9). We will discuss some of our proposed solutions to these drawbacks in Chapter 6.

5.6 Conclusions

The model presented in this chapter achieves our goal of using calcium concentrations in the brain as an indicator of cell survival after an ischaemic stroke. We fill another gap in the literature with our investigation into Turing instabilities and find that our model is capable of showing spatial

inhomogeneities that arise after the system reaches steady-state. The next chapter addresses how we can further improve the model to make it even more biologically realistic and clinically relevant.

6 Conclusions and Future Work

Was it a vision or a waking dream?
Fled is that music: - do I wake or sleep?
'Ode to a Nightingale', John Keats

In the previous chapters, we looked at the different components of a model that uses calcium dynamics to predict cell death in the brain after an ischaemic event. We now consider what we have achieved in this thesis and the appropriate future work that the project still has to offer.

6.1 Conclusions

This thesis discusses a new model of ischaemic stroke that focuses on the concentration of calcium ions to predict whether or not cells in particular regions of the brain may die.

We first investigated, in Chapter 2, the biology behind the model: the different types of brain cells and how they convert glucose into energy, the maintenance of a vast gradient of calcium ions by calcium pumps and how these ions are involved in cell death (apoptosis, necrosis and necroptosis). Chapters 3 and 4 develops two components of the model: the calcium dynamics and cell injury/stress/death equations, respectively. Before we can couple these two components together, we find in Chapter 5 the appropriate modifications that the two diffusion-reaction equations need to undergo in order for the model to display instabilities, giving physiological justifications for these changes. After determining the Turing space, selecting appropriate parameters and calculating that inclusion of any advection terms destroys spatial inhomogeneities, we run the full model, consisting of equations 5.41-5.50.

Hence, this model adds to the current literature in two ways: first, no other current model can predict cell fate, given CBF as the input, using only calcium levels as a biomarker. Thus, our model is simpler than many others and yet has the potential to be clinically relevant. Second, our model is capable of displaying spatial inhomogeneities after steady-state has been reached. This gives it

potential to model the ischaemic core, penumbra and unaffected region in future.

The main limitation of the model is that the simulations still do not portray what is seen clinically after an ischaemic stroke: the ischaemic core, where cells perish quickly, the penumbra, where vulnerable cells dominate but can either survive or die and the unaffected region. Instead, we see around 5 regions (where cells alternate between being predominantly alive and necrotised) in the model without feedback, and just one region (in which all cells survive) when feedback is included. The reason for this is because, even though we perform mode isolation through appropriate parameter selection, this is still not enough to limit both the number of modes and the mode number to 1 (the ideal case that enables simulations to manifest the core, penumbra and unaffected areas). Instead, there are many admissible modes (modes 4 to 24 inclusive in the model without feedback, while in the feedback model, higher-order modes are present) and these interact nonlinearly, resulting in more patterns forming in both the plots for C_e and I. However, higher-order modes form patterns with lower amplitudes. This is why there is only one region for A, V and N in the feedback model: the peaks and troughs of S and D are so small (though numerous) that at no point does D exceed S. We suggest, then, that restricting the admissible modes to just the first mode is an essential requirement to portray the effects of an ischaemic event.

In addition, the analysis of Turing instabilities involves examining the model in the linear regime. Hence, the initial conditions we have used are close enough to the model equilibria to guarantee this analysis holds. In reality, the initial conditions are different and so further work should reflect this. The initial conditions we use are constants across the domain, whereas a stroke initially affects only a small region of the brain. We should also look at the problem in spherical coordinates, for the brain is most easily modelled as a sphere.

Despite these shortcomings, the model has much potential and with improvements can become clinically relevant. The next section, therefore, discusses the ways we can address the limitations of the model.

6.2 Future Work

We now explain, in greater detail, how we will make improvements to the model. To begin with, let us first say that, although our model is much simpler than those that model many different ions and reactions (for instance, the Orlowski model), it could be simplified further. With 10 equations and 26 parameters, it may well be that one or more parameters may not be set at an appropriate value (see Chapter 3.2.5 to see the difficulty parameter fitting poses) and one of the equations may not reflect biological reality. The best way to confront this issue is to further reduce the model. We feel that one way to do so is to reduce the calcium section of the model to focus only on the extracellular component, C_e. It is, after all, the extracellular calcium concentration that affects cells and so the dynamical changes occurring in the astrocytes and neurons (C_a and C_n) can be included implicitly in the extracellular compartment. Running sensitivity analyses, to which Saltelli *et al.* give an introduction, [93], would also be appropriate for model reduction. Hall *et al.,* for instance, use the Morris method, a global sensitivity method, on a model of thermal ablation in the liver, [94], and this would be our initial method of choice.

Having reduced the model, an added advantage is that mathematical analysis is also simplified. This may result in successful isolation of the first mode of Turing instabilities. Remembering that feedback increases the dominant mode (Chapter 5.4.2), we must find parameters such that the model does *not* show instabilities before feedback (yet is on the verge of instability), so that the addition of these feedback terms allows the first mode (and *only* that mode) to show. We should mention, here, that it is not possible to determine analytically the Turing space of the model with feedback because DeGracia's equations do not have closed-form solutions and, hence, we cannot find closed-form solutions for the model equilibria. Similarly, we cannot find the dispersion relation for a model with feedback components. This does not matter for the model without feedback, though, because the only two equations relevant for finding the Turing space are those with diffusion terms (equations 5.44 and 5.45). Hence, we must use the latter as a guide for mode isolation in the former, as described above. One method that is worth trying is simply to adjust

$I_{threshold}$, the threshold injury value (equation 5.51) to a lower number, based on Figures 5.10-5.12 (around 0.2 would be a good initial estimate). There should then be regions where D exceeds S and vice versa, giving rise to Turing patterns in the plots of A, V and N.

In addition to mode selection, we should also consider using initial conditions in the form of a *tanh* function. Although this choice of initial condition is far away enough from equilibrium values such that we will no longer be investigating linear stability, knowing if instabilities exist already in the linear regime is an important first step.

Finally, we should investigate the model using spherical coordinates and in 3 dimensions; this will involve Bessel functions and so analysing the model will be difficult or even not possible analytically. Hence, our work will be dependent on numerical simulations, aided by clues from the linear analysis to ascertain the appropriate ranges of parameter values.

By carrying out these steps, we would then have a model that portrays the different regions seen after a stroke using only one set of equations. There is, subsequently, potential to use clinical data to model individual subjects, increasing the model's clinical relevance. Specifically, we intend to exploit the fact that our model has both a clinically measureable input and output, in the form of CBF and regions of cell death, respectively.

To this end, there are data that have been collected from the Acute Vascular Imaging Centre (AVIC) as part of a clinical trial investigating the temporal dynamics of ischemic stroke. Data at multiple time points (on admission and two hours, 24 hours, 1 week and 1 month post admission) have been collected, including Perfusion-Weighted Imaging, Diffusion-Weighted Imaging and pH-Weighted Imaging, from over 30 patients. Each of these patients exhibits cell death and so the data will be used as the basis of the investigation, as we can then validate the model by observing the decrease in blood flow and the corresponding regions of cell death After validating the model, clinicians can then use it as a tool to find the regions of Vulnerable cells, allowing them to decide whether or not to reperfuse certain regions of the brain.

7 Appendices

Here, we give the four conditions required for our model equations, in the absence of feedback, to show Turing instabilities in terms of the parameters a_1 and D alone, noting that the values of $\overline{C_e}, \bar{I}$ and a_2 are fixed. See Section 5.1.1 for background information.

Then, Condition 1, given by equation 5.12, can be written as:

$$\left(-a_2 - Ce(C_e - I)\left(\frac{2a_2}{I} - \frac{2a_1}{C_e I}\right)\right)_{|(\overline{Ce},\bar{I})} < 0 \quad \text{(A1)}$$

Notice that this depends on a_1 alone (since D is absent in the first two conditions, which examine linear stability in the absence of diffusion).

Condition 2, given by equation 5.14, becomes:

$$a_2 C_e^2 \left(\frac{a_2}{I} - \frac{a_1}{C_e I}\right)_{|(\overline{Ce},\bar{I})} > 0 \quad \text{(A2)}$$

Condition 3, given by equation 5.16, becomes:

$$\left(\frac{1}{I}(a_2 C_e^2 - C_e a_1 + 2DIa_1 + DIa_2 - 2C_e DIa_2)\right)_{|(\overline{Ce},\bar{I})} < 0 \quad \text{(A3)}$$

Finally, Condition 4 (equation 5.18) is now written as:

$$\left(\frac{1}{I^2}(C_e a_1 - C_e^2 a_2 + 2DIa_1 + DIa_2 - 2C_e DIa_2)^2 - \frac{1}{I}(8C_e D(a_1 - C_e a_2)^2)\right)_{|(\overline{Ce},\bar{I})} > 0 \quad \text{(A4)}$$

8. References

[1] R. C. of P. S. S. N. A. P. (SSNAP), “Is stroke care improving? Second SSNAP Annual Report on behalf of the Intercollegiate Stroke Working Party,” 2015.

[2] O. for N. Statistics, “Deaths registered in England and Wales,” 2015.

[3] J. Adamson, A. Beswick, and S. Ebrahim, “Is stroke the most common cause of disability?,” *J. Stroke Cerebrovasc. Dis.*, vol. 13, no. 4, pp. 171–177, Jul. 2004.

[4] M. R. Law, J. K. Morris, and N. J. Wald, “Use of blood pressure lowering drugs in the prevention of cardiovascular disease: meta-analysis of 147 randomised trials in the context of expectations from prospective epidemiological studies.,” *BMJ*, vol. 338, p. b1665, May 2009.

[5] Royal College of Physicians, “Intercollegiate Stroke Working Party. National Clinical guideline for Stroke- Full 2016 guideline,” 2016. .

[6] G. J. Tortora Derrickson, Bryan., *Principles of anatomy and physiology*. Hoboken, N.J.: Wiley, 2011.

[7] D. J. DeGracia, Z. F. Huang, and S. Huang, “A nonlinear dynamical theory of cell injury,” *J. Cereb. Blood Flow Metab.*, vol. 32, no. 6, pp. 1000–1013, Jun. 2012.

[8] D. P. O’Neill *et al.*, “A three-state mathematical model of hyperthermic cell death,” *Ann. Biomed. Eng.*, vol. 39, no. 1, pp. 570–579, Jan. 2011.

[9] G. Guidoboni *et al.*, “Mathematical modeling approaches in the study of glaucoma disparities among people of African and European descents.,” *J. coupled Syst. multiscale Dyn.*, vol. 1, no. 1, pp. 1–21, Apr. 2013.

[10] P. S. Rivadeneira *et al.*, “Mathematical Modeling of HIV Dynamics After Antiretroviral Therapy Initiation: A Review.,” *Biores. Open Access*, vol. 3, no. 5, pp. 233–41, Oct. 2014.

[11] Y. Shi, P. Lawford, and R. Hose, “Review of zero-D and 1-D models of blood flow in the cardiovascular system.,” *Biomed. Eng. Online*, vol. 10, p. 33, Apr. 2011.

[12] M. Heil and D. McKey, “Protective Ant-Plant Interactions as Model Systems in Ecological and Evolutionary Research,” *Annu. Rev. Ecol. Evol. Syst.*, vol. 34, no. 1, pp. 425–553, Nov. 2003.

[13] D. Morale, M. Zanella, V. Capasso, and W. Jäger, “Stochastic Modeling and Simulation of Ion Transport through Channels,” *Multiscale Model. Simul.*, vol. 14, no. 1, pp. 113–137, Jan. 2016.

[14] A. J. McLane, C. Semeniuk, G. J. McDermid, and D. J. Marceau, “The role of agent-based models in wildlife ecology and management,” *Ecol. Modell.*, vol. 222, no. 8, pp. 1544–1556, Apr. 2011.

[15] F. Chiacchio, M. Pennisi, G. Russo, S. Motta, and F. Pappalardo, “Agent-based modeling of the immune system: NetLogo, a promising framework.,” *Biomed Res. Int.*, vol. 2014, p. 907171, 2014.

[16] J. Poleszczuk, P. Macklin, and H. Enderling, “Agent-Based Modeling of Cancer Stem Cell Driven Solid Tumor Growth,” in *Methods in molecular biology (Clifton, N.J.)*, vol. 1516, 2016, pp. 335–346.

[17] V. Papantchev *et al.*, “The role of Willis circle variations during unilateral selective cerebral

perfusion: a study of 500 circles†," *Eur. J. Cardio-Thoracic Surg.*, vol. 44, no. 4, pp. 743–753, Oct. 2013.

[18] B. J. ALPERS, R. G. BERRY, and R. M. PADDISON, "Anatomical Studies of the Circle of Willis in Normal Brain," *Arch. Neurol. Psychiatry*, vol. 81, no. 4, p. 409, Apr. 1959.

[19] R. G. (Ramón G. González, *Acute ischemic stroke : imaging and intervention*. Springer, 2011.

[20] T. J. Simons, "Calcium and neuronal function," *Neurosurg. Rev.*, vol. 11, no. 2, pp. 119–129, 1988.

[21] M. P. Mattson and S. L. Chan, "Calcium orchestrates apoptosis," *Nat. Cell Biol.*, vol. 5, no. 12, pp. 1041–1043, Dec. 2003.

[22] B. J. Gwag *et al.*, "Calcium ionophores can induce either apoptosis or necrosis in cultured cortical neurons," *Neuroscience*, vol. 90, no. 4, pp. 1339–1348, 1999.

[23] A. M. Brown and B. R. Ransom, "Astrocyte glycogen and brain energy metabolism," *Glia*, vol. 55, no. 12, pp. 1263–1271, Sep. 2007.

[24] V. Parpura and P. G. Haydon, "Physiological astrocytic calcium levels stimulate glutamate release to modulate adjacent neurons," *Proc. Natl. Acad. Sci. U. S. A.*, vol. 97, no. 15, pp. 8629–8634, Jul. 2000.

[25] M. Fisher and J. L. Saver, "Future directions of acute ischaemic stroke therapy," *Lancet Neurol.*, vol. 14, no. 7, pp. 758–767, Jul. 2015.

[26] M. Bélanger, I. Allaman, and P. J. Magistretti, "Brain Energy Metabolism: Focus on Astrocyte-Neuron Metabolic Cooperation," *Cell Metab.*, vol. 14, no. 6, pp. 724–738, Jul. 2011.

[27] C. L. MacDonald and G. A. Silva, "A positive feedback cell signaling nucleation model of astrocyte dynamics," *Front. Neuroeng.*, vol. 6, p. 10.3389/fneng.2013.00004, 2013.

[28] C.-P. Chih, P. Lipton, and E. L. Roberts, "Do active cerebral neurons really use lactate rather than glucose?," *Trends Neurosci.*, vol. 24, no. 10, pp. 573–578, Oct. 2001.

[29] A. B. Patel *et al.*, "Direct evidence for activity-dependent glucose phosphorylation in neurons with implications for the astrocyte-to-neuron lactate shuttle.," *Proc. Natl. Acad. Sci. U. S. A.*, vol. 111, no. 14, pp. 5385–90, Apr. 2014.

[30] S. Mangia, I. A. Simpson, S. J. Vannucci, and A. Carruthers, "The *in vivo* neuron-to-astrocyte lactate shuttle in human brain: evidence from modeling of measured lactate levels during visual stimulation," *J. Neurochem.*, vol. 109, pp. 55–62, May 2009.

[31] C. R. Figley, "Lactate transport and metabolism in the human brain: implications for the astrocyte-neuron lactate shuttle hypothesis," *J. Neurosci.*, vol. 31, no. 13, pp. 4768–4770, Mar. 2011.

[32] L. Pellerin and P. J. Magistretti, "Glutamate uptake into astrocytes stimulates aerobic glycolysis: a mechanism coupling neuronal activity to glucose utilization," *Proc. Natl. Acad. Sci. U. S. A.*, vol. 91, no. 22, pp. 10625–10629, Oct. 1994.

[33] A. M. Brown and B. R. Ransom, "Astrocyte glycogen and brain energy metabolism," *Glia*, vol. 55, no. 12, pp. 1263–1271, Sep. 2007.

[34] S. Orrenius, B. Zhivotovsky, and P. Nicotera, "Regulation of cell death: the calcium-apoptosis

link," *Nat. Rev. cell Biol.*, vol. 4, no. 7, pp. 552–565, Jul. 2003.

[35] A. R. Marks, "Calcium and the heart: a question of life and death," *J. Clin. Invest.*, vol. 111, no. 5, pp. 597–600, Mar. 2003.

[36] A. E. Rossi and R. T. Dirksen, "Sarcoplasmic reticulum: the dynamic calcium governor of muscle," *Muscle Nerve*, vol. 33, no. 6, pp. 715–731, Jun. 2006.

[37] E. De Schutter, "Computational Neuroscience: Trends in research 2004," *Neurocomputing*, vol. 58–60, pp. xix–xxi, Jun. 2004.

[38] B. Zhivotovsky and S. Orrenius, "Calcium and cell death mechanisms: a perspective from the cell death community," *Cell Calcium*, vol. 50, no. 3, pp. 211–221, Sep. 2011.

[39] N. R. Sims and H. Muyderman, "Mitochondria, oxidative metabolism and cell death in stroke," *Mitochondrial Dysfunction*, vol. 1802, no. 1. pp. 80–91, 2010.

[40] I. N. Lavrik, R. Eils, N. Fricker, C. Pforr, and P. H. Krammer, "Understanding apoptosis by systems biology approaches," *Mol. Biosyst.*, vol. 5, no. 10, pp. 1105–1111, 2009.

[41] B. R. S. Broughton, D. C. Reutens, and C. G. Sobey, "Apoptotic Mechanisms After Cerebral Ischemia," *Stroke*, vol. 40, no. 5, May 2009.

[42] C. Nicholson, G. T. Bruggencate, R. Steinberg, and H. Stöckle, "Calcium Modulation in Brain Extracellular Microenvironment Demonstrated with Ion-Selective Micropipette," *Proc. Natl. Acad. Sci. U. S. A.*, vol. 74, no. 3, pp. 1287–1290, 1977.

[43] T. Kristian and B. K. Siesjo, "Calcium in ischemic cell death," *Stroke.*, vol. 29, no. 3, pp. 705–718, Mar. 1998.

[44] K. Kaila and B. R. Ransom, *PH and brain function*. Wiley-Liss, 1998.

[45] G. W. J. Harston *et al.*, "Identifying the ischaemic penumbra using pH-weighted magnetic resonance imaging.," *Brain*, vol. 138, no. Pt 1, pp. 36–42, Jan. 2015.

[46] H. Guven, A. E. Cilliler, C. Koker, S. A. Sarikaya, and S. S. Comoglu, "Association of serum calcium levels with clinical severity of acute ischemic stroke," *Acta Neurol. Belg.*, vol. 111, no. 1, pp. 45–49, Mar. 2011.

[47] F. C. Barone and G. Z. Feuerstein, "Inflammatory Mediators and Stroke: New Opportunities for Novel Therapeutics," *J. Cereb. Blood Flow Metab.*, vol. 19, no. 8, pp. 819–834, Aug. 1999.

[48] J. C. Grotta *et al.*, *Stroke : pathophysiology, diagnosis, and management*. .

[49] S. J. Payne, *Cerebral Blood Flow and Metabolism*. WORLD SCIENTIFIC, 2017.

[50] V. Duval, S. Chabaud, P. Girard, M. Cucherat, M. Hommel, and J. P. Boissel, "Physiologically based model of acute ischemic stroke," *J. Cereb. Blood Flow Metab.*, vol. 22, no. 8, pp. 1010–1018, Aug. 2002.

[51] T. Eissing, H. Conzelmann, E. D. Gilles, F. Allgower, E. Bullinger, and P. Scheurich, "Bistability analyses of a caspase activation model for receptor-induced apoptosis," *J. Biol. Chem.*, vol. 279, no. 35, pp. 36892–36897, Aug. 2004.

[52] G. Chapuisat, M. A. Dronne, E. Grenier, M. Hommel, H. Gilquin, and J. P. Boissel, "A global phenomenological model of ischemic stroke with stress on spreading depressions," *Prog.*

Biophys. Mol. Biol., vol. 97, no. 1, pp. 4–27, May 2008.

[53] M. A. Dronne *et al.*, "Mathematical modelling of an ischemic stroke: an integrative approach," *Acta Biotheor.*, vol. 52, no. 4, pp. 255–272, 2004.

[54] M. Cloutier, F. B. Bolger, J. P. Lowry, and P. Wellstead, "An integrative dynamic model of brain energy metabolism using in vivo neurochemical measurements," *J. Comput. Neurosci.*, vol. 27, no. 3, pp. 391–414, Dec. 2009.

[55] M.-A. Dronne, J.-P. Boissel, and E. Grenier, "A mathematical model of ion movements in grey matter during a stroke," *J. Theor. Biol.*, vol. 240, no. 4, pp. 599–615, Jun. 2006.

[56] P. Orlowski, M. Chappell, C. S. Park, V. Grau, and S. Payne, "Modelling of pH dynamics in brain cells after stroke," *Interface Focus*, vol. 1, no. 3, pp. 408–416, Jun. 2011.

[57] A. H. Seidenstein, F. C. Barone, and W. W. Lytton, "Computer modeling of ischemic stroke," *Scholarpedia*, vol. 10, no. 3, p. 32015, 2015.

[58] P. Rutecki, "Ions in the Brain: Normal Function, Seizures, and Stroke," *Neurology*, vol. 66, no. 4, p. 618–618–a, 2006.

[59] A. Aubert, R. Costalat, P. J. Magistretti, and L. Pellerin, "Brain lactate kinetics: Modeling evidence for neuronal lactate uptake upon activation," *Proc. Natl. Acad. Sci.*, vol. 102, no. 45, pp. 16448–16453, Nov. 2005.

[60] L. P. Endresen, K. Hall, J. S. Hoye, and J. Myrheim, "A theory for the membrane potential of living cells," *Eur. Biophys. J.*, vol. 29, no. 2, pp. 90–103, 2000.

[61] M. Fussenegger, J. E. Bailey, and J. Varner, "A mathematical model of caspase function in apoptosis," *Nat. Biotechnol.*, vol. 18, no. 7, pp. 768–774, Jul. 2000.

[62] V. D. Nair, T. Yuen, C. W. Olanow, and S. C. Sealfon, "Early single cell bifurcation of pro- and antiapoptotic states during oxidative stress," *J. Biol. Chem.*, vol. 279, no. 26, pp. 27494–27501, Jun. 2004.

[63] E. Z. Bagci, Y. Vodovotz, T. R. Billiar, G. B. Ermentrout, and I. Bahar, "Bistability in apoptosis: roles of bax, bcl-2, and mitochondrial permeability transition pores," *Biophys. J.*, vol. 90, no. 5, pp. 1546–1559, Mar. 2006.

[64] S. Huang, Y.-P. Guo, G. May, and T. Enver, "Bifurcation dynamics in lineage-commitment in bipotent progenitor cells," *Dev. Biol.*, vol. 305, no. 2, pp. 695–713, 2007.

[65] J. R. Pomerening, "Uncovering mechanisms of bistability in biological systems," *Curr. Opin. Biotechnol.*, vol. 19, no. 4, pp. 381–388, Aug. 2008.

[66] M. Lavrentovich and S. Hemkin, "A mathematical model of spontaneous calcium(II) oscillations in astrocytes," *J. Theor. Biol.*, vol. 251, no. 4, pp. 553–560, Apr. 2008.

[67] M. R. Bennett, L. Farnell, and W. G. Gibson, "A quantitative model of purinergic junctional transmission of calcium waves in astrocyte networks.," *Biophys. J.*, vol. 89, no. 4, pp. 2235–50, Oct. 2005.

[68] B. Li, S. Chen, S. Zeng, Q. Luo, and P. Li, "Modeling the Contributions of Ca2+ Flows to Spontaneous Ca2+ Oscillations and Cortical Spreading Depression-Triggered Ca2+ Waves in Astrocyte Networks," *PLoS One*, vol. 7, no. 10, p. e48534, Oct. 2012.

[69] X.-S. Yang, “Computational modelling of nonlinear calcium waves,” *Applied Mathematical Modelling*, vol. 30, no. 2. pp. 200–208, 2006.

[70] J. D. Murray, *Mathematical Biology II: Spatial Models and Biomedical Applications*. Springer New York, 2013.

[71] Y. Shiferaw and A. Karma, “Turing instability mediated by voltage and calcium diffusion in paced cardiac cells,” *Proc. Natl. Acad. Sci. U. S. A.*, vol. 103, no. 15, pp. 5670–5675, 2005.

[72] A. M. Turing, “The chemical basis of morphogenesis,” *Philos. Trans. R. Soc. London B Biol. Sci.*, vol. 237, no. 641, pp. 37–72, 1952.

[73] P. K. Maini, “The impact of Turing’s work on pattern formation in biology ,” *Math. Today*, vol. 40, no. 4, pp. 140–141, 2004.

[74] A. M. Nesterenko, M. B. Kuznetsov, D. D. Korotkova, and A. G. Zaraisky, “Morphogene adsorption as a Turing instability regulator: Theoretical analysis and possible applications in multicellular embryonic systems,” *PLoS One*, vol. 12, no. 2, p. e0171212, 2017.

[75] G. G. Thomas D., “Artificial Enzyme Membranes and Enzyme Reactors,” *Springer*, 1975.

[76] A. Gierer and H. Meinhardt, “A theory of biological pattern formation,” *Kybernetik*, vol. 12, no. 1, pp. 30–39, Dec. 1972.

[77] J. Schnakenberg, “Simple chemical reaction systems with limit cycle behaviour,” *J. Theor. Biol.*, vol. 81, no. 3, pp. 389–400, Dec. 1979.

[78] J. D. Murray, “Parameter space for turing instability in reaction diffusion mechanisms: A comparison of models,” *Journal of Theoretical Biology*, vol. 98, no. 1. pp. 143–163, 1982.

[79] J. E. Ferrell and W. Xiong, “Bistability in cell signaling: How to make continuous processes discontinuous, and reversible processes irreversible,” *Chaos*, vol. 11, no. 1, pp. 227–236, Mar. 2001.

[80] W. Xiong and J. E. Ferrell Jr, “A positive-feedback-based bistable ‘memory module’ that governs a cell fate decision,” *Nature*, vol. 426, no. 6965, pp. 460–465, Nov. 2003.

[81] A. Kant, T. K. Bhandakkar, and N. V. Medhekar, “Stress enhanced calcium kinetics in a neuron,” *Biomech. Model. Mechanobiol.*, vol. 17, no. 1, pp. 169–180, Feb. 2018.

[82] K. Jin Yang, Guo-Yuan., “Experimental Stroke,” 2010. .

[83] H. C. Tuckwell and R. M. Miura, “A mathematical model for spreading cortical depression,” *Biophys. J.*, vol. 23, no. 2, pp. 257–276, Aug. 1978.

[84] W. E. Schiesser and G. W. Griffiths, *A Compendium of Partial Differential Equation Models: Method of Lines Analysis with Matlab*. Cambridge University Press, 2009.

[85] S. Hamdi, W. E. Schiesser, and G. W. Griffiths, “Method of lines,” *Scholarpedia*, vol. 2, p. 2859, 2007.

[86] D. M. Egelman and P. R. Montague, “Calcium dynamics in the extracellular space of mammalian neural tissue,” *Biophys. J.*, vol. 76, no. 4, pp. 1856–1867, Apr. 1999.

[87] A. Saltelli, M. Ratto, T. Andres, F. Campolongo, and J. Cariboni, *Global sensitivity analysis: the primer*. 2008.

[88] A. Dhooge, W. Govaerts, and Y. A. KUZNETSOV, “MATCONT: A MATLAB package for numerical bifurcation analysis of ODEs,” *ACM Trans. Math. Softw.*, vol. 29, no. 2, pp. 141–164, 2003.

[89] S. H. Strogatz, *Nonlinear Dynamics and Chaos: With Applications to Physics, Biology, Chemistry and Engineering*, 272nd ed. Westview Press, 2001.

[90] T. E. Woolley, R. E. Baker, and P. K. Maini, “Turingâ€™s Theory of Morphogenesis: Where We Started, Where We Are and Where We Want to Go,” in *The Incomputable: Journeys Beyond the Turing Barrier*, S. B. Cooper and M. I. Soskova, Eds. Cham: Springer International Publishing, 2017, pp. 219–235.

[91] P. K. Maini, “Private Correspondence.” .

[92] A. J. PERUMPANANI, J. A. SHERRATT, and P. K. MAINI, “Phase differences in reaction-diffusion-advection systems and applications to morphogenesis,” *IMA J. Appl. Math.*, vol. 55, no. 1, pp. 19–33, Jan. 1995.

[93] A. Saltelli, K. Chan, and E. M. Scott, *Sensitivity Analysis*. Wiley, 2008.

[94] S. K. Hall, E. H. Ooi, and S. J. Payne, “Cell death, perfusion and electrical parameters are critical in models of hepatic radiofrequency ablation,” *Int. J. Hyperth.*, vol. 31, no. 5, pp. 538–550, Jul. 2015.